Computational Investigations of Earth Viscosity Structure Using Surficial Geophysical Observables Related to Isostatic Adjustment

by

Alexander Mackay Hill

A thesis submitted in partial fulfillment of the requirements for the
Master's degree in Earth Sciences

Department of Earth and Environmental Sciences
Faculty of Science
University of Ottawa

Abstract

The research presented in this thesis seeks to address meaningful geodynamic problems related to the viscosity structure of the Earth's interior. Isostatic adjustment is a process which is dependent upon the mechanical properties of the lithosphere and mantle. By performing computational simulations of the isostatic response for various surface-loading scenarios and numerous viscosity structures, insight can be gained into the mechanical structure of the Earth and geodynamic processes related to that structure. The modelled isostatic signal for a given set of Earth model parameters can be compared to real-world observational data in order to identify valid Earth model configurations.

In Chapter 2, the "Transition Zone Water Filter" theory is tested by modelling the geophysical effects of a low-viscosity melt-rich layer atop the 410 km discontinuity. The thickness and viscosity of this layer, and the surrounding mantle, is constrained using observations of relative sea level and the geodetic $\dot{J}_2$ parameter, as well as multiple ice-loading scenarios by which the isostatic adjustment process is driven. The relative sea level data, being most sensitive to the upper mantle and the theorized melt-rich layer it contained, constrain layer properties more effectively than the $\dot{J}_2$ observation, which is strongly dependent on the lower mantle. Constraints on the viscosity of the melt-rich layer vary according to thickness, with thicker layers requiring stiffer viscosities to satisfy observations. For instance, a 20 km thick layer would require a viscosity of 10^{17} Pas or greater, but any of the considered viscosities could be possible for a 1 km thick layer. Similarly, a broad range of upper mantle viscosities are possible, but they must be balanced by variations in the lower mantle. However, $\dot{J}_2$ results show a strong preference for a high-viscosity lower mantle ($\geq 10^{22}$ Pas). For every evaluated Earth model parameter, there is evidence of ice-model sensitivity in the inversion results. Although the results of this study demonstrate that observables related to glacial isostatic adjustment can provide constraints on the properties of this theorized melt-rich layer, the confounding effect of parameter trade-off prevents a more definitive test of this model of mantle geodynamics.

The purpose of the study presented in Chapter 3 is to analyze the nature of solid-Earth deformation beneath the Lower Mississippi River, most crucially in the Mississippi Delta region where subsidence is an ongoing and costly problem. The study uses the displacement of the long

profile of the Lower Mississippi River over the last 80 kyr to constrain isostatic deformation and determine constraints on the mechanical structure of both the mantle and lithosphere. Deformation recorded in the northern portion of the long profile is dominated by the effect of glacial isostatic adjustment, whereas the southern portion is governed by sediment isostatic adjustment. However, the southern portion is also potentially affected by past fault displacement, and to account for this the observational data are corrected using two distinct faulting scenarios. Displacement of the long profile is modelled using either an entirely elastic lithosphere or a lithosphere with internal viscoelastic structure, the latter of which is derived from two end-member geothermal profiles. Between the elastic and viscous lithosphere models, the viscous models are better able to replicate the observational data for each faulting scenario – both of which prefer a viscous lithosphere corresponding to the warmer geotherm. The chosen faulting scenario exerts no control over the optimal mantle model configuration, however the optimal mantle for the viscous lithosphere models is much stiffer than was determined for their elastic counterparts, reflecting significant parameter trade-off between mantle and lithosphere mechanical structure. These study results demonstrate the utility of the long profile displacement data set for constraining Earth viscosity structure, as well as the importance of considering more-complex models of lithosphere mechanical structure when addressing surface-loading problems similar to those encountered in the Mississippi Delta region.

Acknowledgements

Foremost, I want to express my gratitude for my thesis supervisor, Professor Glenn Milne. I worked for Glenn during my undergraduate as a research assistant, which was a terrific experience that informed me of what an effective supervisor he was. With the prior knowledge that he was a great supervisor, I decided that pursuing graduate school research with him was the optimal course of action. Those who have worked with Glenn know that he has impressive technical expertise as well as great character as a person. During my graduate studies, Glenn consistently provided timely feedback and was attentive to my research, despite his many other obligations. In addition to the exceptional guidance provided by my supervisor, my thesis research benefited from feedback provided by other parties, and with that in mind I would like to thank Joseph Kuchar, Giorgio Ranalli, Zhixiong Shen, and Torbjörn Törnqvist for their valuable intellectual input. Similarly, I am grateful to my thesis committee for their judicial evaluation and insightful commentary on the content of this thesis.

Another positive aspect of my graduate school experience was my research group. Everyone was supportive of one another as well as happy to share resources and technical knowledge. Giving presentations and discussing articles within the group was always a constructive and collaborative experience. I wish all the best to my fellow research group members. I would also like to express my thanks to all of the faculty and staff in the Department of Earth and Environmental Sciences for creating a supportive environment within which I was able to develop as a scientist. Finally, I am grateful for the funding provided by the Natural Sciences and Engineering Research Council which made this research possible.

Table of Contents

List of Figures

Chapter 1

Introduction

1.1 General Thesis Research Introduction

The scientific study of the Earth has always been limited because the interior of our planet cannot be observed directly. By necessity, the study of the planet's interior demands creative and innovative approaches to problem solving. One such method is the application of physics to model or simulate phenomena which take place within the Earth's interior. The application of physical theory allows one to construct a framework within which the Earth's interior properties can be defined and related to each other. What cannot be seen must be imagined using our understanding of the physical laws of our world.

The Earth's interior properties cannot be observed directly, but they can be related to features or observables on/at the Earth's surface. By relating surficial effects to an internal planetary process using the framework of physical theory, the nature of the surficial signature for a given internal process can be predicted. This surficial signature is dependent upon the physical properties of the Earth's interior as well as the nature of the perturbation imposed upon it. Through modelling the physical processes taking place within the Earth, geophysicists can infer Earth's interior properties by identifying models which are congruent with real-world surficial observations.

Many of the deformational processes operating in our planet's interior are governed by material viscosity. For this reason, viscosity is a physical property of the Earth's interior which is of scientific interest. For example, the nature of thermal energy transfer within the planet is strongly dependent upon material viscosity. The deformation of material resulting from an imposed force is another process which is mediated by viscosity. Although the task of observing deformation acting within a planet's interior is enigmatic, there can be effects relating to deformation which manifest themselves at the planet's surface and thus can be observed directly. One example of an imposed force is a surface load, such as an ice sheet or deposited sediment. A surface load will cause deformation within the planet, and the nature of that deformation along with its consequential effects at the planet's surface (i.e. isostatic adjustment) will be governed by the

viscosity of the deformed material. By studying the surficial response to such an applied load, the viscosity of the planet's interior can be inferred (Haskell, 1935, 1936). This task can be accomplished by simulating the physical deformation process using computational models. For a given surface load and viscosity, a specific pattern of surficial effects will arise. Such computational models can consider varying viscosities within the planet (i.e. 'viscosity structure') as well as different surface load configurations. Surficial effects which are predicted by these models can be compared to real-world observational records in order to identify valid deformation scenarios. In this way the viscosity of a planet's interior can be constrained. A simple analogy can be imagined by considering that the Earth resembles an orange, mechanically. It has a thin elastic rind and a fleshy ductile interior. If one picks up an orange and wants to ascertain how ripe it is, they may press their thumb into the orange and observe the response. In the research presented here, a similar process is employed. By observing how the Earth responds to a deforming impulse, one can determine how 'ripe' the planet is.

1.1.1 Research Contributions

This thesis can be divided into two research projects, the first of which is a sensitivity analysis concerning Earth viscosity structure relating to the so-called "Transition Zone Water Filter" model (Bercovici & Karato, 2003; Karato et al., 2006; Leahy & Bercovici, 2007, 2010). This model seeks to explain various geochemical paradoxes by invoking the presence of a melt-rich layer above the mantle transition zone, atop the 410 km seismic discontinuity. In addition to geochemical effects, the presence of such a melt-rich layer has major implications for mantle viscosity structure. The relation between this Transition Zone Water Filter and viscosity structure has never before been evaluated in the academic literature, and so we explore this aspect of it and relate its mechanical properties to surficial geophysical observations. In doing so, we are able to determine constraints on the viscosity and thickness of the melt-rich layer predicted by this model. Such constraints are useful in that they improve our understanding of the nature of the theorized melt-rich layer itself, and because they may allow future research to place limitations on other aspects of its behaviour, such as the effectiveness of the filtering process. Furthermore, the sensitivity analysis offers insight into the relationship between overall mantle viscosity

structure and the properties of a thin low-viscosity zone, and into how these factors influence geophysical observations at the planet's surface.

The second research project presented here evaluates viscosity structure of both the lithosphere and mantle using fluvial long profile data collected in the south-central United States. Both elastic and viscous scenarios of lithosphere rheology are considered, with the viscous scenarios corresponding to different geothermal conditions. Varying lithospheric thicknesses are also considered in the analysis. By modelling how long profile deformation develops for these different scenarios, insight is gained into how isostatic effects at the surface relate to lithosphere structure. Similarly, for the mantle, different scenarios of mantle viscosity structure are considered in conjunction with the array of possible lithosphere structures. In this way the relationship between these two Earth structures, and how they act together to control surficial deformation, is also evaluated. By identifying the model scenarios which best replicate observed long profile data, constraints can be placed on Earth rheological structure and geothermal conditions, as well as regional fault displacement. Constraining these geophysical properties offers insight into the past and ongoing geodynamics of the region. Perhaps most importantly, an understanding of Earth structure in the area is essential for projecting future sea level changes along the Gulf Coast due to the significance of fault displacement and isostasy in the region.

1.2 Background Geophysical Theory

1.2.1 Isostatic Adjustment

The Quaternary Period of Earth's natural history is characterized by repeated planetary-scale glaciations. These glaciations are a climatic process through which significant mass is transported to and accumulates upon high-latitude continents, most notably Laurentia and Fennoscandia (Clark & Mix, 2002; Clark et al., 2009; Ehlers et al., 2018). During the last glacial maximum, the volume of grounded ice is thought to have been approximately 5.2×10^7 km^3 greater than present glaciation (Lambeck et al., 2014). The accumulation of such significant mass imposes a load which must be accommodated by the underlying Earth material. The mechanically weak material (i.e. the mantle) beneath the load flows away from the overburdened area, which in turn leads to subsidence at the surface (Figure 1.1). In this way isostatic

equilibrium is achieved. When the surface load is removed, the opposite process occurs and uplift takes place at the planet's surface. These responses in the solid Earth to glacial accumulation and retreat are referred to using the term 'glacial isostatic adjustment.'

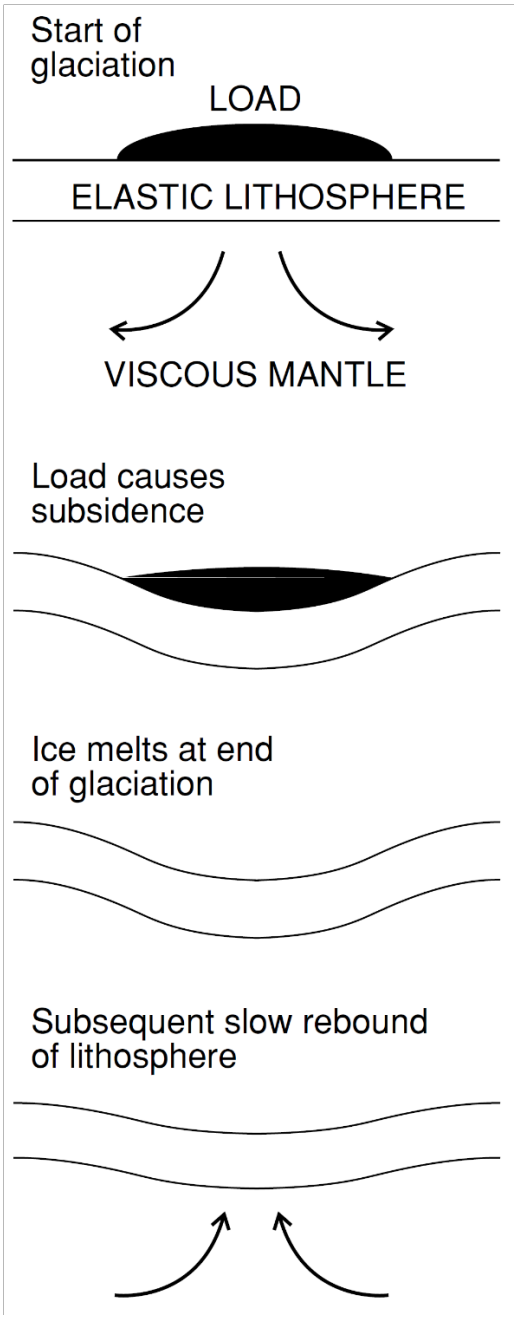

Figure 1.1. Illustration of how the solid Earth deforms in response to a glacial load, and how this process affects surface elevation (Fowler, 2005).

The isostatic adjustment process is dependent not only on the imposed load, but on the physical properties of the underlying solid Earth – most importantly, viscosity structure. The rates of uplift and subsidence vary according to viscosity structure; lower viscosity materials are more readily deformed and thus result in more rapid isostatic accommodation (Haskell, 1937). The spatial distribution of the load is important as well. Intuitively, one would correctly expect that zones of greater loading (i.e. thicker ice overburden) would undergo a greater magnitude of isostatic displacement, with correspondingly more rapid relaxation following the removal of the load. However, the effect of glacial isostatic adjustment is not solely confined within the perimeter of the ice mass. Around the ice mass perimeter there is an isostatic effect which is opposite in its direction of motion and lesser in magnitude relative to the effect occurring directly beneath the glaciation. This effect can be clearly observed in modern measurements of vertical land motion (see Figure 1.2). During glaciation, mantle material flows outwards from the overburden area and causes uplift around the ice sheet – a phenomenon known as the peripheral bulge (Cathles, 1975). All of these solid-Earth deformation processes manifest themselves at the surface in the form of elevation changes, and so they can be related to observable data such as sea level (Daly, 1925).

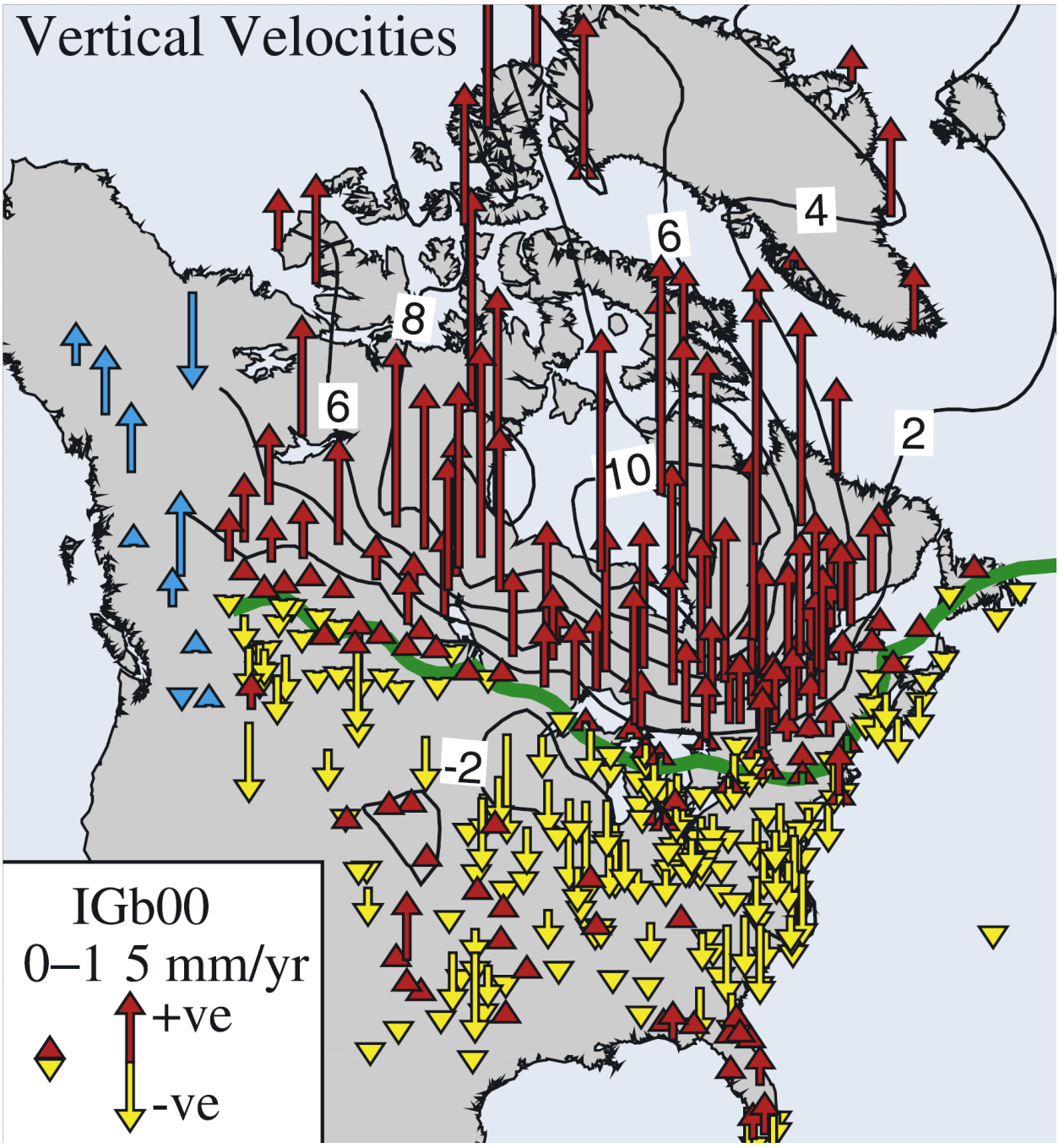

Figure 1.2. Vertical land motion in modern North America recorded by GPS sites. Uplift and subsidence indicated by red and yellow arrows, respectively. Shown in green is a 'hinge line' which separates areas of postglacial rebound from peripheral bulge subsidence. Blue arrows indicate measurements significantly affected by tectonic processes unrelated to glacial isostatic adjustment (Sella et al., 2007).

The process of glacial isostatic adjustment outlined above can be generalized to other forms of mass redistribution at the planet's surface. In addition to the direct effect of water being partitioned into glacial reservoirs, large-scale glaciation also causes redistribution of ocean water due to changes in the geoid (Tamisiea et al., 2001) and the effect of ocean syphoning (Mitrovica & Milne, 2002). The redistribution of ocean mass also necessitates isostatic adjustment – a process known as hydroisostasy (Lambeck, 2019). Sedimentation is another mechanism through which mass is rearranged on a planet's surface. For instance, clastic sediment deposition at the mouth of a river system will cause isostatic subsidence, which in turn will create accommodation space for additional sediment mass transfer (Reynolds et al., 1991). The act of deltaic sedimentation also displaces ocean water. For this reason, sediment isostatic adjustment can be more complicated to model than other isostasy scenarios because the change in the ocean load must be accounted for as well (see Figure 1.3, Lawson, 1942; Kuchar et al., 2018). Regardless of its composition, for any mass deposited on the Earth's surface, the dependence of the isostatic process on planetary viscosity structure will be governed by the lateral extent of the surface load. A surface load with greater lateral extent will exhibit more dependence on deeper viscosity structure, and vice versa (Mitrovica & Peltier, 1991).

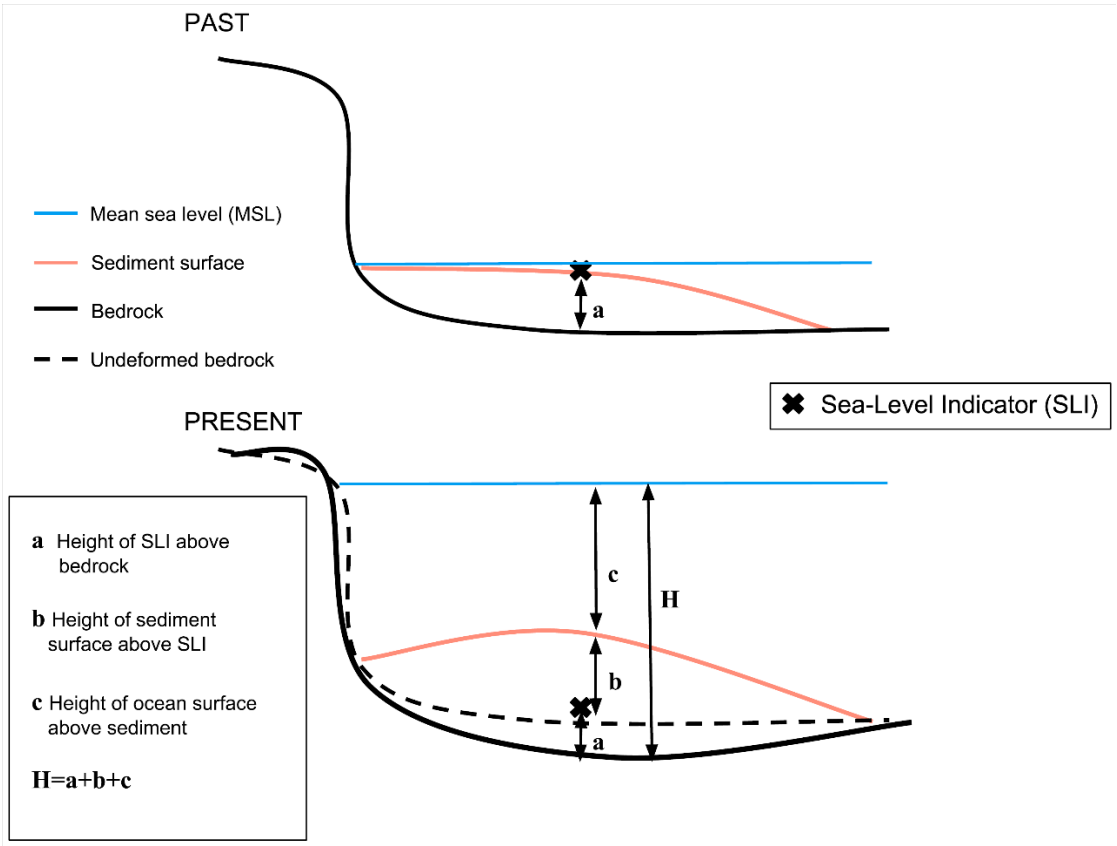

Figure 1.3. Relations between sediment deposition, sea level, ocean loading, and solid-Earth deformation (Kuchar et al., 2018).

1.2.2 Earth Material Rheology

The nature of Earth material rheology is timescale-dependent (Hudson & Harrison, 1997; Karato, 2012). Over short timescales, the Earth responds in an elastic manner to an applied stress. Over longer timescales, the Earth responds in a viscous manner (i.e. behaves as a viscous fluid). The simplest rheological model that can simulate this time-dependent behaviour is the Maxwell model. In the Maxwell model of a viscoelastic material, elastic and viscous components are combined 'in series' such that each component is subjected to the same amount of stress. Displayed in Figure 1.4 is a mechanical analogue commonly used to represent Maxwell viscoelastic behaviour: the linear combination of a spring and dashpot. When a Maxwell viscoelastic material is subjected to a stress, the elastic component of deformation occurs instantaneously whereas the viscous deformation accumulates over time in a manner linearly

proportional to the applied stress (Reddy, 2013). The time periods for which elastic or viscous deformation dominate can be distinguished by a time value known as the Maxwell time (Ranalli, 1995). For a Maxwell material subjected to a stress, the Maxwell time defines the timescale at which the elastic and viscous components of deformation are equal in magnitude. Stress timescales which greatly exceed the Maxwell time will be dominated by viscous behaviour.

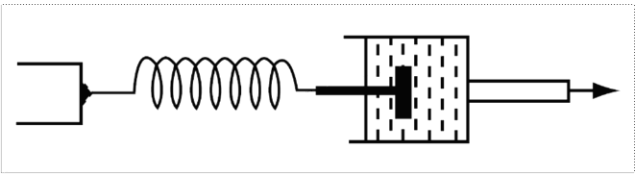

Figure 1.4. A mechanical analogue of the Maxwell model of a viscoelastic material. The two elements combined in series are a spring and dashpot, representing the elastic and viscous deformation components, respectively (Stacey & Davis, 2008).

For the stress timescale of thousands of years encountered in the isostatic processes modelled in this thesis, the solid Earth behaves as a viscoelastic material (Peltier, 2011; Watts, 2011). The considered stresses occur at timescales that are both shorter and longer than the Maxwell time for mantle material (~100 years; see Figure 1.5), therefore the Earth's interior can be appropriately modelled as a Maxwell viscoelastic material. In this way both the short-term elastic and long-term viscous responses to surface loading are accounted for. For the magnitude of stresses involved, the use of a linear rheology is justified by the assumption that diffusion creep is the dominant deformation mechanism involved in isostatic adjustment (Cathles, 1975, but see Gasperini et al., 2004; Dal Forno et al., 2005 for a dissenting opinion). For a spherically symmetric self-gravitating planet with Maxwell viscoelastic rheology, the response of the solid Earth to a time-dependent surface mass load can be determined using the numerical method presented in Peltier (1974).

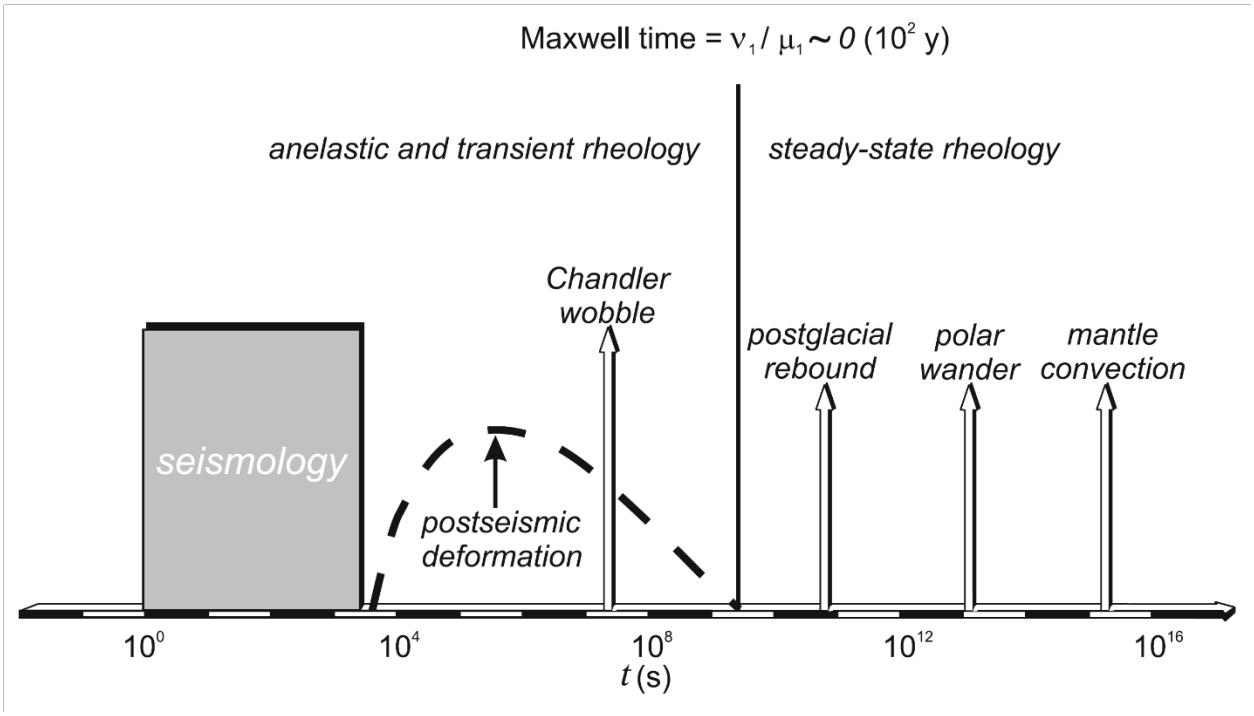

Figure 1.5. Timescales (logarithmic scale) of deformation for various geophysical phenomena relative to the Maxwell time (~100 years) of mantle material (Sabadini et al., 2016).

When modelling solid-Earth deformation on a large scale (e.g. ice sheet isostasy) the lithosphere is commonly approximated as being entirely elastic (Wolf, 1993). However, in reality it is known that the lithosphere contains material which will behave as a viscous fluid under specific conditions (Burov, 2011a). As already outlined above, a long timescale of deformation is required (Burov, 2011b; Watts, 2011). Additionally, there is a strong dependence on temperature. This is particularly true for the lithosphere, where the geothermal gradient is much steeper relative to the underlying mantle (Jaupart & Mareschal, 2011). The viscosity of a material is strongly dependent on temperature, and for this reason a sufficiently high temperature is required for lithosphere material to behave in a viscous manner. This temperature-sensitivity is depicted in Figure 1.6; one can see that a temperature increase of 100K can reduce viscosity by nearly an order of magnitude.

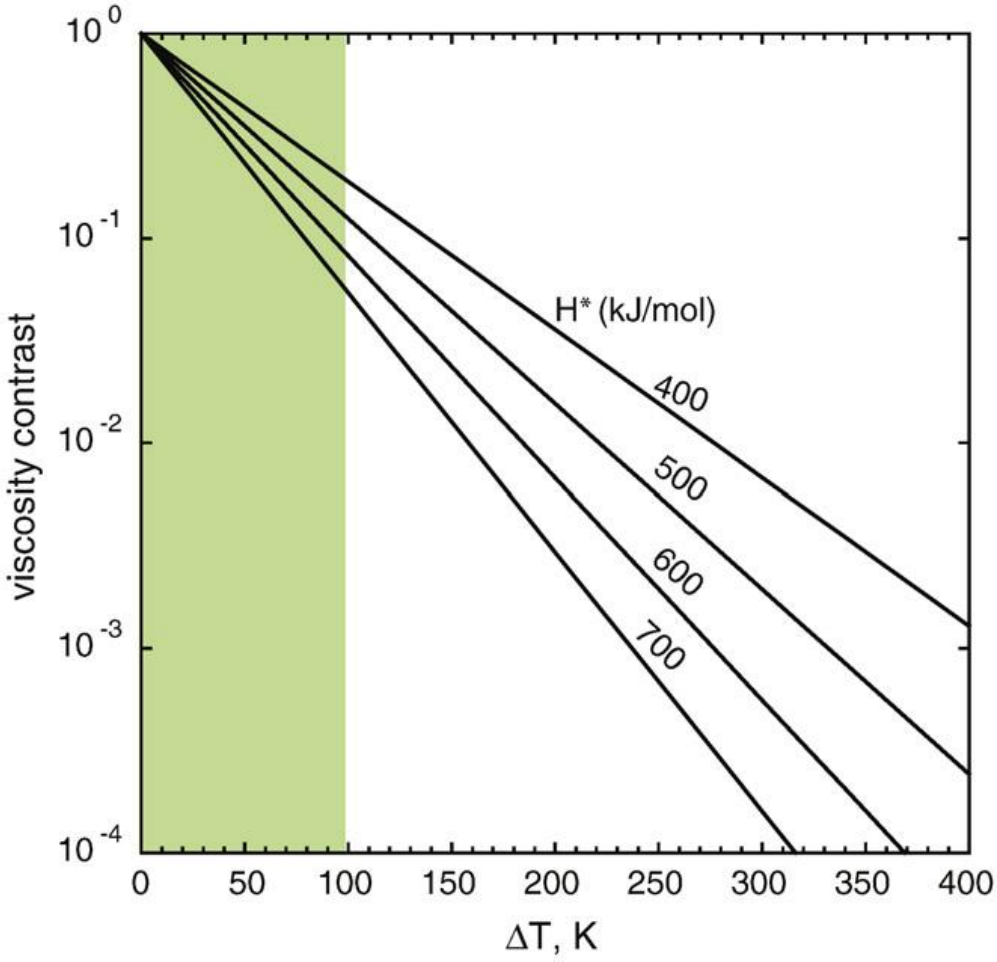

Figure 1.6. Lithospheric mantle viscosity temperature-dependence for an array of activation enthalpies(H^*). Temperature change for viscosity ratios of less than ~1 order of magnitude highlighted in green (Karato, 2010).

1.2.3 Lithosphere Flexure

When the Earth's surface is subjected to loading, the lithosphere responds by macroscale bending due to its rigidity. This bending effect is known as lithosphere flexure, and its development is dependent upon the thickness and rheological structure of the lithosphere for a given loading scenario (Walcott, 1970; Turcotte, 1979). The physical theory of plate flexure is simplified by assuming the material is perfectly elastic, but reality is more complex than this. Real-world observations of lithosphere flexure deviate from what would be expected in the perfectly elastic case. This deviation has given rise to the phrase 'effective elastic thickness,'

which refers to the thickness of a theorized elastic lithosphere which would replicate the observed behaviour of the considered real-world lithosphere (Caldwell et al., 1976; Burov & Diament, 1995; Tesauro et al., 2012). The introduction of additional ductile (i.e. relatively lower viscosity) material to the lithospheric column will progressively decrease the effective elastic thickness. For any lithospheric flexure scenario, the topographic evolution associated with plate bending will be governed by the lithosphere's effective elastic thickness. Lithospheres with lower effective elastic thicknesses permit the development of relatively higher amplitude (and shorter wavelength) topography changes in response to surficial loading (Watts, 2001; Turcotte & Schubert, 2014; Nield et al., 2018). This phenomenon is demonstrated in Figure 1.7, where it can be seen that more-localized (i.e. higher amplitude and shorter wavelength) topographic effects occur for lithospheres which have weaker mechanical structure and thus have lower effective elastic thicknesses.

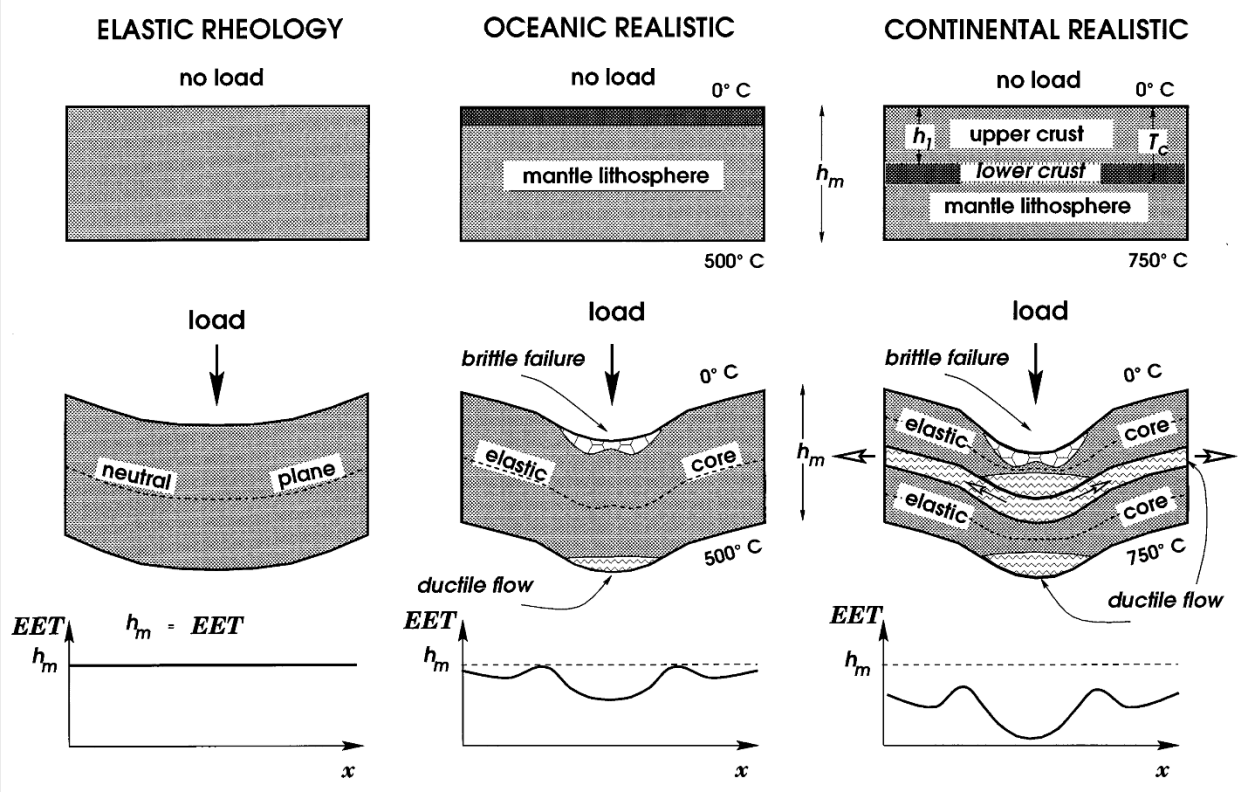

Figure 1.7. Flexure scenarios for various lithosphere mechanical structures. Effective elastic thickness (EET) is plotted for each scenario (Burov & Diament, 1996).

1.3 Geophysical Inversion and Modelling

Geophysical inversion is the practice of relating observational geophysical data to a model configuration which would most accurately produce those observations (Menke, 1989; Aster et al., 2019). This relation between real-world phenomena and theoretical models is a reciprocal one – a theoretical model can be resolved based upon observational data, or theoretical models can be used to produce observable data. The former of these procedures is known as inverse modelling and the latter is known as forward modelling. In order to relate models and observational data, a geophysical inversion procedure will seek to define the data-model fit as a function of the considered model parameters. During forward modelling investigations, it is often the case that the computational efficiency of the inversion is limited by the cost of computing output for each considered model. For this reason, it is common practice that the inversion algorithm through which data-model fit is evaluated will perform a targeted search among model parameters, such that the optimal solution is converged upon instead of needlessly mapping out the entire model-fit parameter space.

In the research studies presented in this thesis a forward modelling approach is used. Models of Earth interior structure are created, and through computational simulation a set of geophysical quantities are predicted for each model. By comparing this synthetic model output to real-world observational data, the degree to which each model satisfies observational constraints is evaluated. However, comparison with real-world constraints often yields some issues when seeking an optimal data-model fit. Foremost, there is the non-uniqueness problem: observational constraints often permit multiple models, meaning that the geophysical inversion problem cannot be solved with strictly one unique model. A change in one model parameter can be compensated by a change in another model parameter, such that an equivalent model output can be produced by multiple unique model configurations. These parameter trade-off effects can prevent the inversion from yielding exact constraints on model characteristics. As a consequence, results may consist of a range of permitted values for each considered model variable rather than a set of unique solutions. There are many ways to estimate optimal model parameters, but the research presented in this thesis employs what is typically referred to as a global optimization method for parameter determination (Sen & Stoffa, 2011).

A fundamental aspect of geophysical inversion is the design of the forward model. To approximate the physical structure of the Earth, the modelled interior is divided into four distinct radial zones: the lithosphere, the upper mantle, lower mantle, and an effectively inviscid core. The lithosphere is treated as being entirely elastic unless stated otherwise (see Chapter 3 where viscous lithospheres are considered). The lower and upper mantle are each assigned a viscosity value, and each of these mantle viscosity values is varied independently of the other. For all Earth models, the internal structure is spherically symmetric and a linear Maxwell viscoelastic rheology is used to compute deformation.

For these Earth models to generate a measurable response, they must be subjected to a perturbation. The perturbation involved in this research is some form of surface loading, most commonly continent-scale glaciation, or a sediment load – see Chapter 3. Therefore, an ice history reconstruction is required as an input for the modelling process. The ice history employed most frequently here is provided by Peltier (2004); it is known as ICE-5G. The sensitivity of some surficial observables to the chosen ice history reconstruction is a matter of ongoing debate (Kuchar et al., 2020), and with this in mind some additional ice history inputs are used as well. Specifics on ice model selection are provided in the respective methods sections of Chapters 2 and 3. Global-scale glaciation is a process which inevitably involves the redistribution of large volumes of water, and for this reason there are changes in ocean mass that will also significantly perturb the modelled Earth (Milne et al., 1999; Mitrovica & Milne, 2003). Therefore the global distribution of ocean water mass must be taken into consideration as model input. Similarly, the rearrangement of mass involved in glaciation has non-negligible effects on the planet's rotational dynamics that must also be included as a model perturbation (Mitrovica et al., 2001).

1.4 Observational Data

Deformation processes which take place in the planet's interior can produce physical effects which manifest themselves at the planet's surface. For the isostatic processes considered in the research presented here, the surface of the planet is displaced as a direct result of the internal deformation. Although the surface displacement which occurred in the past cannot be directly observed, there are proxies which have recorded this information. One of the most commonly

employed proxies of past surface displacement is relative sea level, which is a measure of the height of the mean sea surface relative to a fixed coastal location (Cofaigh & Bentley, 2013; Nelson, 2013). For relative sea level records collected at locations very far from the loading area, the solid-Earth displacement can be isolated from the observational data by removing the eustatic signal (Bassett et al., 2005; Milne, 2015). However, for locations proximal to the loading area, the gravitational changes which take place during both loading and rebound exert significant control over sea level as well (Milne & Shennan, 2013).

One limitation of sea level data is that it can only provide observational records of surface displacement for coastal regions. Fortunately, there are observational proxies for displacement further inland. Land surface displacement has measurable effects on fluvial geomorphology. Specifically, the long profile of a river will be distorted by any vertical displacement of the Earth's surface (Goudie, 2004; Charlton, 2008). Long profile data has been used efficaciously in past research to study tectonic processes taking place in the planet's interior (Whittaker et al., 2008; Crow et al., 2014; Wolstencroft et al., 2014).

The isostatic adjustment process involves the rearrangement of mass at the Earth's surface, which in turn causes mass transfer in the planet's interior due to the flow of viscous Earth material. Even after the surface load is removed, mass transport continues to take place in the planet's interior during isostatic rebound. These continuous rearrangements of the planet's mass (surface and interior) produce measurable changes in the gravitational field (Wahr & Davis, 2002; Tiwari & Hinderer, 2011; Sabadini et al., 2016). Although the exact configuration of the Earth's geoid in the distant past is unknown, recent advances in satellite geodetic technology have allowed the modern geoid to be measured; for example, via the NASA-DLR joint satellite mission known as GRACE, which collected time-variable measurements of Earth's geopotential during the early 21st century (Wahr, 2007; Cazenave et al., 2011). When dealing with spherical potential fields such as Earth's geopotential, a convenient mathematical formulation is the use of spherical harmonics. The spherical harmonic treatment involves a spatio-spectral decomposition of the spherical form of the planet's geopotential (Freeden & Gutting, 2013). The geoid – the equipotential that most closely depicts mean sea level – can be expressed as a linear combination of spherical harmonic functions. In Chapter 2 of this thesis, the spherical harmonic coefficient for the order zero (i.e. zonal) and degree 2 component of the geoid expansion is examined as a

possible model constraint. In intuitive terms, this zonal spherical harmonic is representative of the 'oblateness' of Earth's geoid (Nerem & Wahr, 2011; Cheng et al., 2013). A visual representation of this spherical harmonic function is displayed in Figure 1.8. The time derivative of the coefficient of this function in the geoid expansion is adopted in Chapter 2 as a model constraint, where it is assigned the parameter $\dot{J}_2$ (consistent with past literature). This component of Earth's geopotential is commonly used to study geophysical phenomena in Earth's deep interior due to its high sensitivity to mass redistribution in the lower mantle (Peltier, 1983; Latychev et al., 2005; Nakada et al., 2015, 2016) For the purpose of the research presented here, the time-domain behaviour of the J_2 parameter is an informative proxy for the mass flow taking place in the planet's interior due to the ongoing isostatic rebound process. However, modern behaviour of this parameter is also influenced by another significant mass transfer process – the migration of water from ice sheets in polar regions. The effects caused by ongoing meltwater flux must be removed from the observed geoid signal in order to obtain an accurate measurement of GIA-related mass flow (Johnston & Lambeck, 1999; Mitrovica et al., 2007).

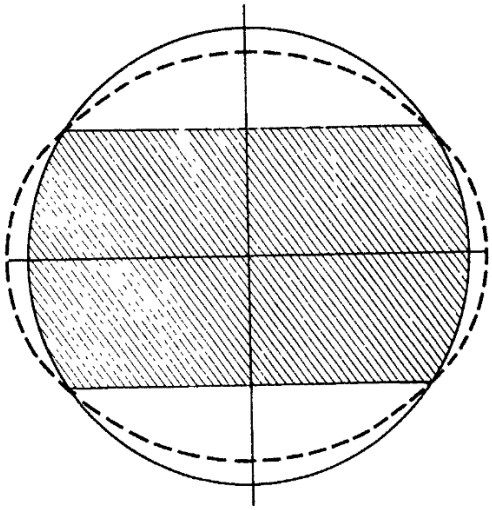

Figure 1.8. The degree 2, order 0 zonal spherical harmonic (J_2) of Earth's geopotential, indicated by the shaded region (Burkard, 1968).

1.5 References

Aster, R.C., Borchers, B. & Thurber, C.H., 2019. *Parameter Estimation and Inverse Problems*. Elsevier.

Bassett, S.E., Milne, G.A., Mitrovica, J.X. & Clark, P.U., 2005. Ice sheet and solid Earth influences on far-field sea-level histories, *Science,* **309**, 925-928.

Bercovici, D. & Karato, S.-I., 2003. Whole-mantle convection and the transition zone water filter, *Nature,* **425**, 39-44.

Burkard, R.K., 1968. *Geodesy for the Layman*. United States Air Force, Aeronautical Chart and Information Center.

Burov, E., 2011a. Rheology and strength of the lithosphere, *Mar. Petrol. Geol.,* **28**, 1402-1443.

Burov, E., 2011b. Lithosphere, mechanical properties, in *Encyclopedia of Solid Earth Geophysics,* pp. 693-701, eds Gupta, H.K., Springer.

Burov, E. & Diament, M., 1995. The effective elastic thickness (T_e) of continental lithosphere: What does it really mean?, *J. Geophys. Res.,* **100**(B3), 3905-3927.

Burov, E. & Diament, M., 1996. Isostasy, equivalent elastic thickness, and inelastic rheology of continents and oceans, *Geology,* **24**(5), 419-422.

Caldwell, J.G., Haxby, W.F., Karig, D.E. & Turcotte, D.L., 1976. On the applicability of a universal elastic trench profile, *Earth Planet. Sci. Lett.,* **31**, 239-246.

Cathles, L.M., 1975. *The Viscosity of the Earth's Mantle*. Princeton University Press.

Cazenave, A., Ramillien, G. & Biancale, R., 2011. Gravity field, temporal variations from space techniques, in *Encyclopedia of Solid Earth Geophysics,* pp. 484-489, eds Gupta, H.K., Springer.

Charlton, R., 2008. *Fundamentals of Fluvial Geomorphology*. Taylor & Francis.

Cheng, M., Tapley, B.D. & Ries, J.C., 2013. Deceleration in the Earth's oblateness, *J. Geophys. Res. Solid Earth,* **118**, 740-747, doi:10.1002/jgrb.50058.

Clark, P.U., Dyke, A.S., Shakun, J.D., Carlson, A.E., Clark, J., Wohlfarth, B., Mitrovica, J.X., Hostetler, S.W. & McCabe, A.M., 2009. The Last Glacial Maximum, *Science,* **325**, 710-714.

Clark, P.U. & Mix, A.C., 2002. Ice sheets and sea level of the Last Glacial Maximum, *Quaternary Sci. Rev.,* **21**, 1-7.

Cofaigh, C.Ó. & Bentley, M.J., 2013. Late Quaternary relative sea-level changes in high latitudes, in *Encyclopedia of Quaternary Science,* pp. 467-480, eds Elias, S.A., Mock, C.J., Elsevier.

Crow, R., Karlstom, K., Darling, A., Crossey, L., Polyak, V., Granger, D., Asmerom, Y. & Schmandt, B., 2014. Steady incision of Grand Canyon at the million year timeframe: A case for mantle-driven differential uplift, *Earth Planet. Sci. Lett.,* **397**, 159-173.

Daly, R.A., 1925. Pleistocene changes of level, *Am. J. Sci.,* **10**, 281-313.

Ehlers, J., Gibbard, P.L. & Hughes, P.D., 2018. Quaternary glaciations and chronology, in *Past Glacial Environments,* pp. 77-101, eds Menzies, J. & van der Meer, J.J.M., Elsevier.

Fowler, C.M.R., 2005. *The Solid Earth*. Cambridge University Press.

Freeden, W. & Gutting, M., 2013. *Special Functions of Mathematical (Geo-)Physics*. Springer.

Goudie, A.S., 2004. Long profile, river, in *Encyclopedia of Geomorphology,* pp. 630-630, eds Goudie, A.S., Taylor & Francis.

Haskell, N.A., 1935. The motion of a viscous fluid under a surface load, *Physics,* **6**, 265-269.

Haskell, N.A., 1936. The motion of a viscous fluid under a surface load. Part II, *Physics,* **7**, 56-61.

Haskell, N.A., 1937. The viscosity of the asthenosphere, *Am. J. Sci.,* **38**, 22-28.

Hudson, J.A. & Harrison, J.P., 1997. *Engineering Rock Mechanics – An Introduction to the Principles*. Elsevier.

Jaupart, C. & Mareschal, J.-C., 2011. Lithosphere, continental: Thermal structure, in *Encyclopedia of Solid Earth Geophysics,* pp. 681-693, eds Gupta, H.K., Springer.

Johnston, P. & Lambeck, K., 1999. Postglacial rebound and sea level contributions to changes in the geoid and the Earth's rotation axis, *Geophys. J. Int.,* **136**, 537-558.

Karato, S.-I., 2010. Rheology of the deep upper mantle and its implications for the preservation of the continental roots: A review, *Tectonophysics,* **481**, 82-98.

Karato, S.-I., 2012. *Deformation of Earth Materials – An Introduction to the Rheology of the Solid Earth*. Cambridge University Press.

Karato, S.-I., Bercovici, D., Leahy, G., Richard, G. & Jing, Z., 2006. The transition-zone water filter model for global material circulation: Where do we stand?, in *Earth's Deep Water Cycle,* pp. 289-313, eds Jacobsen, S.D., Van Der Lee, S., American Geophysical Union.

Kuchar, J., Milne, G.A., Hill, A.M., Tarasov, L. & Nordman, M., 2020. An investigation into the sensitivity of postglacial decay times to uncertainty in the adopted ice history, *Geophys. J. Int.,* **220**, 1172-1186.

Kuchar, J., Milne, G.A., Wolstencroft, M., Love, R., Tarasov, L. & Hijma, M., 2018. The influence of sediment isostatic adjustment on sea level change and land motion along the U.S. Gulf Coast, *J. Geophys. Res. Solid Earth,* **123**, 780-796, doi:10.1002/2017JB014695.

Lambeck, K., 2019. Isostasy, in *Encyclopedia of Coastal Science,* pp. 1039-1047, eds Finkl, C.W., Makowski, C., Springer.

Lambeck, K., Rouby, H., Purcell, A., Sun, Y. & Sambridge, M., 2014. Sea level and global ice volumes from the Last Glacial Maximum to the Holocene, *Proc. Natl. Acad. Sci. USA,* **111**(43), 15296-15303.

Latychev, K., Mitrovica, J.X., Tamisiea, M.E., Tromp, J., Christara, C.C. & Moucha, R., 2005. GIA-induced secular variations in the Earth's long wavelength gravity field: Influence of 3-D viscosity variations, *Earth Planet. Sci. Lett.,* **240**, 322-327.

Lawson, A.C., 1942. Mississippi Delta – a study in isostasy, *Geol. Soc. Am. Bull.,* **53**, 1231-1254.

Leahy, G. & Bercovici, D., 2007. On the dynamics of a hydrous melt layer above the transition zone, *J. Geophys. Res.,* **112**, B07401, doi:10.1029/2006JB004631.

Leahy, G. & Bercovici, D., 2010. Reactive infiltration of hydrous melt above the mantle transition zone, *J. Geophys. Res.,* **115**, B08406, doi:10.1029/2009JB006757.

Menke, W., 1989. *Geophysical Data Analysis: Discrete Inverse Theory*. Academic Press.

Milne, G.A., 2015. Glacial isostatic adjustment, in *Handbook of Sea-Level Research,* pp. 421-437, eds Shennan, I., Long, A.J., Horton, B.P., John Wiley & Sons.

Milne, G.A., Mitrovica, J.X. & Davis, J.L., 1999. Near-field hydro-isostasy: the implementation of a revised sea-level equation, *Geophys. J. Int.,* **139**, 464-482.

Milne, G.A. & Shennan, I., 2013. Isostasy: Glaciation-induced sea-level change, in *Encyclopedia of Quaternary Science,* pp. 452-459, eds Elias, S.A., Mock, C.J., Elsevier.

Mitrovica, J.X., Latychev, K. & Tamisiea, M.E., 2007. Time variable gravity: glacial isostatic adjustment, in *Treatise on Geophysics, Volume 3: Geodesy,* pp. 197-211, eds Herring, T., Elsevier.

Mitrovica, J.X. & Milne, G.A., 2002. On the origin of late Holocene sea-level highstands within equatorial ocean basins, *Quaternary Sci. Rev.,* **21**, 2179-2190.

Mitrovica, J.X. & Milne, G.A., 2003. On post-glacial sea level: I. General theory, *Geophys. J. Int.,* **154**, 253-267.

Mitrovica, J.X., Milne, G.A. & Davis, J.L., 2001. Glacial isostatic adjustment on a rotating earth, *Geophys. J. Int.,* **147**, 562-578.

Mitrovica, J.X. & Peltier, W.R., 1991. Radial resolution in the inference of mantle viscosity from observations of glacial isostatic adjustment, in *Glacial Isostasy, Sea-Level and Mantle Rheology,* pp. 63-78, eds Sabadini, R., Lambeck, K., Boschi, E., Kluwer Academic Publishers.

Nakada, M., Okuno, J., Lambeck, K. & Purcell, A., 2015. Viscosity structure of Earth's mantle inferred from rotational variations due to GIA process and recent melting events, *Geophys. J. Int.,* **202**, 976-992.

Nakada, M., Okuno, J. & Yokoyama, Y., 2016. Total meltwater volume since the Last Glacial Maximum and viscosity structure of Earth's mantle inferred from relative sea level changes at Barbados and Bonaparte Gulf and GIA-induced $\dot{J}_2$, *Geophys. J. Int.,* **204**, 1237-1253.

Nerem, R.S. & Wahr, J., 2011. Recent changes in the Earth's oblateness driven by Greenland and Antarctic ice mass loss, *Geophys. Res. Lett.,* **38**, L13501, doi:10.1029/2011GL047879.

Nelson, A.R., 2013. Tectonics and relative sea-level change, in *Encyclopedia of Quaternary Science,* pp. 503-519, eds Elias, S.A., Mock, C.J., Elsevier.

Nield, G.A., Whitehouse, P.L., van der Wal, W., Blank, B., O'Donnell, J.P. & Stuart, G.W., 2018. The impact of lateral variations in lithospheric thickness on glacial isostatic adjustment in West Antarctica, *Geophys. J. Int.,* **214**, 811-824.

Peltier, W.R., 1974. The impulse response of a Maxwell Earth, *Rev. Geophys.,* **12**(4), 649-669.

Peltier, W.R., 1983. Constraints on deep mantle viscosity from LAGEOS acceleration data, *Nature,* **304**, 434-436.

Peltier, W.R., 2004. Global glacial isostasy and the surface of the ice-age Earth: the ICE-5G (VM2) model and GRACE, *Ann. Rev. Earth Planet. Sci.,* **32**, 111-149.

Peltier, W.R., 2011. Mantle viscosity, in *Encyclopedia of Solid Earth Geophysics,* pp. 869-876, eds Gupta, H.K., Springer.

Ranalli, G., 1995. *Rheology of the Earth*. Chapman & Hall.

Reddy, J.N., 2013. *An Introduction to Continuum Mechanics*. Cambridge University Press.

Reynolds, D.J., Steckler, M.S. & Coakley, B.J., 1991. The role of the sediment load in sequence stratigraphy: The influence of flexural isostasy and compaction, *J. Geophys. Res. Solid Earth,* **96**, 6931-6949, doi:10.1029/90JB01914.

Sabadini, R., Vermeersen, B. & Cambiotti, G., 2016. *Global Dynamics of the Earth: Applications of Viscoelastic Relaxation Theory to Solid-Earth and Planetary Geophysics*. Springer.

Sella, G.F., Stein, S., Dixon, T.H., Craymer, M., James, T.S., Mazzotti, S. & Dokka, R.K., 2007. Observation of glacial isostatic adjustment in "stable" North America with GPS, *Geophys. Res. Lett.,* **34**(2), L02306, doi:10.1029/2006GL027081.

Sen, M.K. & Stoffa, P.L., 2011. Inverse theory, global optimization, in *Encyclopedia of Solid Earth Geophysics,* pp. 625-632, eds Gupta, H.K., Springer.

Stacey, F.D. & Davis, P.M., 2008. *Physics of the Earth*. Cambridge University Press.

Tamisiea, M.E., Mitrovica, J.X., Milne, G.A. & Davis, J.L., 2001. Global geoid and sea level changes due to present-day ice mass fluctuations, *J. Geophys. Res. Solid Earth,* **106**, 30849-30863, doi:10.1029/2000JB000011.

Tesauro, M., Audet, P., Kaban, M.K., Bürgmann, R. & Cloetingh, S., 2012. The effective elastic thickness of the continental lithosphere: Comparison between rheological and inverse approaches, *Geochem. Geophys. Geosyst.,* **13**, Q09001, doi:10.1029/2012GC004162.

Tiwari, V.M. & Hinderer, J., 2011. Gravity field, time variations from surface measurements, in *Encyclopedia of Solid Earth Geophysics,* pp. 489-494, eds Gupta, H.K., Springer.

Turcotte, D.L., 1979. Flexure, *Adv. Geophys.,* **21**, 51-86.

Turcotte, D.L. & Schubert, G., 2014. *Geodynamics*. Cambridge University Press.

Wahr, J.M., 2007. Time variable gravity from satellites, in *Treatise on Geophysics, Volume 3: Geodesy,* pp. 213-237, eds Herring, T., Elsevier.

Wahr, J.M. & Davis, J.L., 2002. Geodetic constraints on glacial isostatic adjustment, in *Ice Sheets, Sea Level and the Dynamic Earth,* pp. 3-32, eds Mitrovica, J.X., Vermeersen, B.L.A., American Geophysical Union.

Walcott, R.I., 1970. Flexural rigidity, thickness, and viscosity of the lithosphere, *J. Geophys. Res.,* **75**, 3941-3954.

Watts, A.B., 2001. *Isostasy and Flexure of the Lithosphere*. Cambridge University Press.

Watts, A.B., 2011. Isostasy, in *Encyclopedia of Solid Earth Geophysics,* pp. 647-661, eds Gupta, H.K., Springer.

Whittaker, A.C., Attal, M., Cowie, P.A., Tucker, G.E. & Roberts, G., 2008. Decoding temporal and spatial patterns of fault uplift using transient river long profiles, *Geomorphology,* **100**, 506-526.

Wolf, D., 1993. The changing role of the lithosphere in models of glacial isostasy: a historical review, *Global Planet. Change,* **8**, 95-106.

Wolstencroft, M., Shen, Z., Törnqvist, T.E., Milne, G.A. & Kulp, M., 2014. Understanding subsidence in the Mississippi Delta region due to sediment, ice, and ocean loading: Insights from geophysical modeling, *J. Geophys. Res. Solid Earth,* **119**, 3838-3856, doi:10.1002/2013JB010928.

Chapter 2

Sensitivity of Glacial Isostatic Adjustment to a Partially Molten Layer at 410 km Depth

Geophysical Journal International

Geophys. J. Int. (2019) **216,** 1538–1548
Advance Access publication 2018 November 16
GJI Geodynamics and tectonics

doi: 10.1093/gji/ggy358

Sensitivity of glacial isostatic adjustment to a partially molten layer at 410 km depth

Alexander M. Hill,[1] Glenn A. Milne,[1,2] Joseph Kuchar[2] and Giorgio Ranalli[3]

[1]*Department of Earth and Environmental Sciences, University of Ottawa, Ottawa: K1N 6N5, Canada. E-mail: ahill075@uottawa.ca*
[2]*Department of Physics, University of Ottawa, Ottawa, Canada*
[3]*Department of Earth Sciences, Carleton University, Ottawa: K1S 5B6, Canada*

Accepted 2018 November 15. Received 2018 April 24; in original form 2017 November 15

SUMMARY

We present a sensitivity analysis aimed at testing whether observables related to glacial isostatic adjustment can support or refute the occurrence of a low viscosity melt-rich layer (MRL) above the mantle transition zone, as required by the 'transition-zone water-filter' model (Bercovici & Karato 2003). In total, 1600 model runs were performed sampling a range of MRL thicknesses (1, 10 and 20 km) and viscosities (10^{15}–10^{19} Pa·s), plausible viscosity values in the upper and lower mantle regions and four distinct ice histories. To determine decay time constraints, we consider relative sea level (RSL) data from two sites [Ångerman River (ÅR), Sweden and Richmond Gulf (RG), Canada] and use a new method of observational sea level data correction. Comparing model output of postglacial decay times and $\dot{J}_2$ to observational constraints, we find numerous possible solutions, largely as a result of parameter trade-off. The investigated observables are sensitive to the existence of an MRL and reasonable variations in its thickness and viscosity. The magnitude and nature of this sensitivity varies between the two data types as well as the adopted background viscosity structure. Decay time results from either considered location do not strictly support or exclude MRL existence. However, both locations offer MRL viscosity requirements for given thicknesses, with ÅR being more restrictive. RG constraints allow MRL viscosities as low as 10^{16} Pa·s (10 km) and 10^{17} Pa·s (20 km). ÅR results narrow these permitted viscosity ranges to 10^{18} Pa·s or greater for both 10 and 20 km MRL thicknesses. In the case of a 1 km thick MRL, ÅR constraints permit the viscosity to be as low as 10^{17} Pa·s, whereas those of RG permit any MRL viscosity. The decay time observations are satisfied by only a small subset of 'background' mantle viscosities (regardless of the MRL properties), none of which support a spherically symmetric solution of Earth viscosity. Finally, comparing model output to the observed $\dot{J}_2$ value did not provide any constraints on MRL properties. However, our results show that this observable has a strong preference for viscosity values in the lower mantle that are equal to or greater than 10^{22} Pa·s.

Key words: Structure of the Earth; Loading of the Earth; Sea level change; Rheology: mantle.

1 INTRODUCTION

The 'transition zone water-filter' model, as described by Bercovici & Karato (2003) and Karato *et al.* (2006), predicts the presence of a hydrous partially molten layer above the 410 km seismic discontinuity in the mantle, with a thickness in the 1–20 km range. The cause for the formation of this layer is the difference in water storage capacity across the 410 km seismic discontinuity (Hirschmann 2006; Ohtani *et al.* 2016). Upwelling mantle material moving through the 410 km boundary undergoes a mineralogical phase change from wadsleyite to olivine. Wadsleyite has considerably greater water storage capacity than olivine, thus this phase change releases free water (Ohtani *et al.* 2004), which decreases the solidus temperature and causes dehydration melting. As shown by Matsukage *et al.* (2005), this hydrous melt is more dense than olivine-bearing mantle material, but less dense than wadsleyite-bearing material, and therefore accumulates atop the 410 km discontinuity.

From the standpoint of mineral physics, the most important evidence for the existence of this hydrous melt-rich layer (MRL) is the demonstration of significantly higher (up to 3 o.o.m.) water diffusivity in wadsleyite with respect to olivine (Hae *et al.* 2006; Chen *et al.* 2011; Litasov *et al.* 2011; but see Hirschmann *et al.* 2005; Litasov *et al.* 2007 for a dissenting view). The study of ringwoodite inclusions in diamond has shown that, at least locally, the transition

zone is hydrous, to about 1 per cent weight (Pearson *et al.* 2014). A property highly sensitive to water content is electrical conductivity. Although resolution is not very high, geophysically inferred electrical conductivity distributions show larger values in the transition zone than in the upper mantle, suggesting greater water content in the former (e.g. Karato 2011).

Attempts have been made to detect the partially molten layer by seismic methods. Experimental work by Yoshino *et al.* (2007) suggests that the presence of a hydrous melt could noticeably reduce seismic wave velocities. The presence of a low velocity zone above the 410 km discontinuity has been inferred in northwestern Canada (Schaeffer & Bostock 2010) and at various other locations around the globe (Benz & McCarthy 1994; Revenaugh & Sipkin 1994; Gilbert *et al.* 2003; Gao *et al.* 2006; Courtier & Revenaugh 2007; Jasbinsek & Dueker 2007; Schmerr & Garnero 2007; Jasbinsek *et al.* 2010; Tauzin *et al.* 2010; Vinnik *et al.* 2010; Hier-Majumder & Courtier 2011; Schmandt *et al.* 2011; Chu *et al.* 2012; Liu *et al.* 2016; Thio *et al.* 2016). However, seismic data show little evidence that the mantle transition zone is hydrated (Houser 2016).

In this paper, we evaluate the sensitivity of observations relating to glacial isostatic adjustment (GIA) to an MRL above the mantle transition zone as predicted by the transition-zone water-filter model. The GIA process has been widely used to infer the mantle viscosity distribution (e.g. Peltier & Andrews 1976; Lambeck *et al.* 1998; Mitrovica *et al.* 2000; Mitrovica & Forte 2004; Soldati *et al.* 2009; Nakada *et al.* 2015; Lau *et al.* 2016). By modelling the GIA response to the presence of a hydrous MRL of varying thickness and viscosity, we aim to determine if GIA observations can be used to test the existence of such a layer. Previous studies have used GIA observables in an attempt to constraint properties of relatively thin and localised layers of lower viscosity (e.g. Milne *et al.* 1998; Paulson & Richards 2009) with mixed results. Solution non-uniqueness associated with parameter trade-off—thickness and viscosity of the low viscosity zone, as well as with the adopted ambient viscosity profile—is a key issue (Paulson & Richards 2009). Another limitation of using GIA observations to infer mantle viscosity is that these data are also sensitive to the glacial loading history which is not precisely known. For this reason, we focus our analysis on observables that are less sensitive to this model input; specifically, decay times inferred from sea level reconstructions (e.g. Walcott 1972; Mitrovica & Peltier 1995; Mitrovica *et al.* 2000) and the rate of change in the degree 2, order 0 component of the geopotential (known as $\dot{J}_2$, Peltier 1983; Yoder *et al.* 1983). We note, however, that $\dot{J}_2$ is sensitive to the rate and location of contemporary ice mass variations (Yoder & Ivins 1985; Trupin *et al.* 1992) and so these must be considered when using this observable to constrain the GIA process (see following section).

2 METHODS

2.1 Data

Relative sea level (RSL) decay times are estimated based on the relationship (Mitrovica *et al.* 2000):

$$\mathrm{RSL}\,(t) = A(e^{-t/\tau} - 1) + C \tag{1}$$

where t is time and the constants A and C represent a site-specific amplitude and datum shift, respectively. The decay time τ is sensitive to the mantle viscosity structure but relatively insensitive to the ice history (local and non-local). We estimate it by a total least-squares method. Specifically, we use the ODR (orthogonal distance regression) package from the Python library Scipy. This Python tool is a derivative of the Fortran ODRPACK software package (Boggs *et al.* 1989, 1992). By comparing decay times from RSL observations with those determined from a GIA model for a variety of viscosity structures, the sensitivity of postglacial decay times to the presence of an MRL can be evaluated (see Section 2.2).

We use decay times estimated from RSL reconstructions at two locations: Ångerman River (ÅR), Sweden, and Hudson Bay, Canada (Fig. 1). These regions experienced glacial loading of different lateral scale and so will exhibit different depth sensitivity to mantle viscosity structure (Mitrovica & Peltier 1991; Mitrovica 1996). Within Hudson Bay, two localities have substantial observational data: James Bay (JB) and Richmond Gulf (RG) (Hardy 1976, 1977; Hillaire-Marcel 1976). Although these two localities are nearby to one another, they have yielded remarkably different RSL observations. The RSL data collected in JB by Hardy (1976, 1977) has been shown to be anomalous, likely due to flawed methodology (Mitrovica *et al.* 2000). Fang & Hager (2002) attributed the anomalous JB RSL data to observational errors. Similarly, Pendea *et al.* (2010) concluded that meaningful analysis of the RSL data collected by Hardy (1976, 1977) in JB was not possible. For these reasons, we defer to the RSL observations from RG (Hillaire-Marcel 1976; Peltier 1998; Mitrovica *et al.* 2000) to define a decay time from Hudson Bay for this analysis. For ÅR, we adopt the RSL data assessed and presented by Nordman *et al.* (2015). The RSL index points from RG that we used to compute a decay time for this locality are provided in Table S1 in the Supporting Information.

The employment of the exponential decay time formalism is most valid when the study region is entirely in a state of free relaxation and unaffected by any ongoing loading. Therefore, to most accurately determine the decay time from RSL reconstructions, several component RSL signals were estimated and removed from the observations to isolate the signal associated with the free decay (uplift) of the solid Earth due to ice sheet unloading. By considering only a time window after deglaciation, the contaminating influence of an active glacial load is avoided. However, even within this time window it is known that there are other sources of gravitational and solid Earth deformation (e.g. ocean loading and rotational effects) which would have been preserved in the observational sea level records. For instance, Han & Gomez (2018) demonstrate that regional ocean loading has an effect on decay time estimates in the Hudson Bay region which is both non-negligible and spatially variable. In addition to localised RSL changes, there is also the global eustatic (meltwater) sea level change which must be accounted for. A correction for this component of RSL change has been employed in past studies which assessed GIA using sea level indicators (e.g. Mitrovica *et al.* 2000; Nordman *et al.* 2015). Due to the observational RSL data being a record of all RSL changes, rather than only the ice-related isostatic adjustment, we remove all component RSL changes from the observational data except that which is produced by ice-related isostasy. By performing this operation, the following effects are removed from the sea level record: ocean loading-related changes, GIA-induced changes in Earth rotation and global mean sea level changes due to eustasy and GIA (syphoning; e.g. Mitrovica & Milne 2002). This correction which is applied to the sea level observations can be expressed as

$$\mathrm{RSL}_{\mathrm{corr}} = \mathrm{RSL}_{\mathrm{full}} - \mathrm{RSL}_{\mathrm{ice}} \tag{2}$$

where $\mathrm{RSL}_{\mathrm{full}}$ represents model output of RSL that incorporates all effects described above and $\mathrm{RSL}_{\mathrm{ice}}$ is the modelled RSL component derived strictly from ice loading only. The correction ($\mathrm{RSL}_{\mathrm{corr}}$) will vary depending on the Earth viscosity structure and ice history

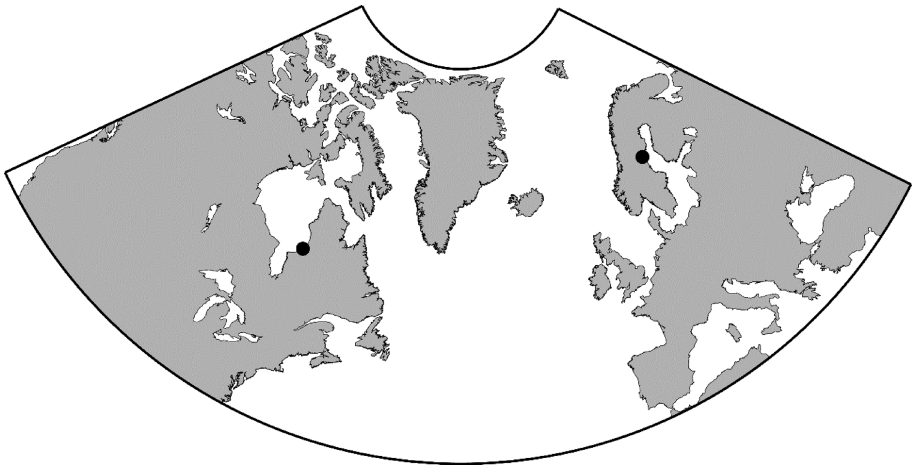

Figure 1. Locations of RSL data sites considered in this study: Richmond Gulf (Hudson Bay, Canada) and Ångerman River (Sweden).

considered. It follows that the estimated decay time for a given observational RSL record differs for each set of model parameters because the correction applied will change.

While the modelled RSL curves generated in this study are determined for exact locations, the observational RSL time-series used to validate these modelled curves are composed of data with coordinates that vary considerably. If there is a large sea level gradient between the locations of the RSL index points, then this can introduce significant error (Nordman *et al.* 2015; Han & Gomez 2018). Mitrovica *et al.* (2000) found that when RSL data from RG and JB are combined into a single curve, a significantly different decay time is determined than would be found by considering the locations separately. To account for such spatial inconsistency, each observational RSL index point is shifted by the difference in modelled sea level between the aggregate location (i.e. a spatial average of all data locations using in a given RSL curve) and the actual data location. For example, if modelled RSL at a given time and index point location is 200 m, and modelled RSL at the aggregate location is 150 m at that same time step, then the RSL value of the considered observational data point will be shifted by −50 m before the decay time is computed. This spatial correction method is dependent on model output generated for a given viscosity structure and ice load model, and so will produce unique results for each set of model parameters.

For each corrected observational RSL time-series, the parameters of eq. (1) are determined using the ODR method previously outlined. We define the range of permissible decay times as falling within two standard deviations of the optimal decay time value (i.e. $\tau \pm 2\sigma$). For this parameter estimation process, we restrict the datum shift C to the same range considered appropriate by Mitrovica *et al.* (2000) and Nordman *et al.* (2015) for RG and ÅR, respectively.

Change in $\dot{J}_2$ is driven by two significant forcings: GIA and surface water mass transfer associated with modern ice melting (Yoder & Ivins 1985; Trupin *et al.* 1992; Mitrovica & Peltier 1993; Wahr *et al.* 1993; Nakada *et al.* 2015; Lau *et al.* 2016). Therefore, the contribution from modern glacial melting must be estimated and removed from the observed $\dot{J}_2$ value in order to isolate the GIA-driven component. We adopt the GIA-related $\dot{J}_2$ value of $-5.4 \pm 0.7 \times 10^{-11}$ yr^{-1} determined by Lau *et al.* (2016).

We chose to include $\dot{J}_2$ in this analysis given that it has complementary viscosity depth sensitivity to postglacial decay times; specifically, it has been shown to exhibit a greater dependence on deeper mantle viscosity structure (Wu & Peltier 1982, 1983; Peltier 1983; Mitrovica & Peltier 1993; Lau *et al.* 2016). It has also been shown to exhibit sensitivity to the inclusion of relatively thin low viscosity zones in the upper mantle (Milne *et al.* 1998).

2.2 Model

RSL decay times and $\dot{J}_2$ were computed for a large number of Earth viscosity models that included (and in some cases did not) a low viscosity layer immediately above 410 km depth, as proposed in the transition-zone water-filter model. Even though our chosen observables are known to be relatively insensitive to the adopted ice history (e.g. Nordman *et al.* 2015; Lau *et al.* 2016), we used four ice loading models to consider the sensitivity of our results to this model input. We used the global ICE-5G model (Peltier 2004) as well as two other regional models that replaced either the North American component or the Fennoscandian component of ICE-5G. The North American component was replaced by the 9927 model reconstruction from Tarasov *et al.* (2012, this model will be referred to as ICE-5G-NAIS9927), and the Fennoscandian component was replaced by the 78311 model reconstruction from Tarasov (2013,this model will be referred to as ICE-5G-FIS78311). Model output of RSL and $\dot{J}_2$ was also generated using the global ice model reconstruction produced by Lambeck and colleagues (e.g. Lambeck 1993; Lambeck *et al.* 1998; Lambeck *et al.* 2014, 2017), henceforth referred to as the Australia National University (ANU) model. We chose these ice models as they are well known within the GIA community and they provide a means to test the rigour of our results with regard to plausible variations in this important GIA model input. The ice model reconstructions introduced above were generated using different data sets and modelling methodologies and so the reader is referred to the original articles cited above for further information.

RSL changes were computed using the theory and algorithm described in Mitrovica & Milne (2003) and Kendall *et al.* (2005) using a spherical harmonic truncation of degree and order 256. GIA-related changes in Earth rotation were incorporated when solving the sea-level equation (Milne & Mitrovica 1998; Mitrovica *et al.* 2005). $\dot{J}_2$ was computed using the relationship provided in eq. (15) of Mitrovica *et al.* (1993).

The Earth was modelled as a spherically symmetric self-gravitating Maxwell viscoelastic planet. Love numbers were computed following the approach described in Peltier (1974). The elastic

and density structure were defined using a seismic model (the Preliminary Reference Earth Model, Dziewonski & Anderson 1981) and a depth discretization that varied from 5 km in the crust to 30 km at the base of the mantle. To account for the presence of a thin (1–20 km) low viscosity layer, the resolution of radial layering at depths of 410 km was increased from 20 km to a resolution of either 0.1 km, for 1 km thick MRLs, or 1 km for MRLs with thicknesses of 10 or 20 km. The viscosity structure of the sub-lithospheric mantle was discretized in two or three layers, with the two-layer case comprising the upper mantle (base of lithosphere to 670 km) and lower mantle (670 km to core–mantle boundary); the three-layer case includes a thin layer with viscosity lower than that of the ambient upper-mantle value. In any given model run, the viscosity in each of these layers was uniform. The thickness of the elastic lithosphere was fixed at 96 km because the GIA observables considered here have been shown to be insensitive to variations in this parameter (Mitrovica 1996; Mitrovica & Forte 2004).

Model runs were performed for a range of upper (UMV) and lower-mantle viscosities (LMV) as well as viscosities and thicknesses of the low viscosity layer immediately above 410 km depth. For the lower mantle, viscosities of 1, 5, 10, 30 and 50 $\times$ 10^{21} Pa·s were considered, while viscosities of 1, 3, 5, 7 and 9 $\times$ 10^{20} Pa·s were considered for the upper mantle. These parameter ranges encompass the majority of inferences for the average viscosity in these regions (Peltier 1983; Lambeck *et al.* 1998; Mitrovica & Forte 2004; Nakada *et al.* 2015; Nordman *et al.* 2015; Lau *et al.* 2016; Métivier *et al.* 2016). The MRL is assumed to range from 1 to 20 km in thickness (Bercovici & Karato 2003; Leahy & Bercovici 2010); we considered three values: 1, 10 and 20 km. The mean viscosity within this layer is not well known. At relatively low pressure, the presence of melt ($\geq$ 4–5 per cent by volume) is known to decrease the viscosity by 1–2 o.o.m. in both diffusion and dislocation creep regimes (Hirth & Kohlstedt 1995a, 1995b). A further viscosity decrease is possibly associated to grain size reduction, due to transformational superplasticity (e.g. Vaughan & Coe 1981) and/or the pinning effect of the melt phase limiting grain growth and increasing the role of grain boundary sliding (Hirth & Kohlstedt 1995a, 1995b). The decrease of dihedral angle with increasing pressure at solid-melt-solid triple junctions in partially molten aggregates (Yoshino *et al.* 2007; Karato 2014), implying complete wetting of grain boundaries for melt fractions as low as 1 per cent, is another potential factor in decreasing the viscosity. Acting together, these processes could decrease the viscosity of melt-rich material at the top of the transition zone by 3–4 o.o.m. (Kohlstedt & Zimmerman 1996; Warren & Hirth 2006). We therefore assign viscosities in the range 10^{15}–10^{19} Pa·s to the MRL layer in the sensitivity analysis.

A total of 400 model runs were performed for each ice model covering all possible combinations of MRL viscosity and thickness for the range of background UMV and LMV given above (including cases of MRL absence). For each model run, RSL curves were computed for ÅR and RG. In order to isolate the ice-induced deformation component of the signal, the contributions from other processes (ocean loading, rotational effects and eustatic sea level change) were removed. For each modelled RSL curve, decay times were computed using the same orthogonal distance regression method applied to the observational data. For ÅR, this analysis was performed using model output from 8 kyr to present, whereas this timescale was shortened to 7 kyr to present for RG. These timescales were chosen to ensure that local ice had completely melted and thus the GIA signal was unaffected by ongoing glacial loading (Walcott 1980). Glaciation in Hudson Bay persisted for longer than in Fennoscandia, therefore we are able to extend our analysis for ÅR further into the past. These timescales match the span of the available observational RSL data.

For some model parameter sets, the computed RSL curves did not exhibit an exponential form (Fig. S1, Supporting Information). As a consequence, the computed decay time in these cases is inaccurate and so we do not consider them in the following analysis (except for identifying them in relevant figures as being unreliable). We rule out these non-exponential RSL curves simply on the basis that the observational data does behave according to a pattern of exponential decay.

3 RESULTS AND DISCUSSION

3.1 Sensitivity analysis

3.1.1 Postglacial decay times

RSL curves for both ÅR and RG were generated using a fixed background mantle viscosity model and MRL thickness (Fig. 2). Inspecting these curves, we see that a decrease in MRL viscosity accelerates the rate of RSL change, consequently causing a decrease in decay time (eq. 1). Lower decay time values will be produced by any model variations which yield more rapid RSL change, such as reduction in MRL viscosity. Comparing the determined RSL curves in Fig. 2, it is apparent that RSL changes at these locations respond differently to MRL properties. These sensitivity variations are expected due to the varying depth dependence of the isostatic response to viscosity structure at these locations. As a consequence of the greater lateral scale of glacial loading in North America compared to Fennoscandia, RSL changes in RG are more dependent on viscosity structure at greater depths (see Mitrovica & Peltier 1991; Mitrovica 1996). Consequently, the isostatic response at ÅR is more sensitive to MRL properties.

Fig. 3(a) shows the array of decay times computed at ÅR using ICE-5G for a fixed LMV of 10^{22} Pa·s and all considered UMV values. Inspecting these results for a 10 km thick MRL and 5 $\times$ 10^{20} Pa·s UMV, one can relate these model decay times to the RSL curves shown in Fig. 2. It is clear that decreasing MRL viscosity typically has the effect of reducing decay time, and that the magnitude of this effect is, in general, greater when the layer is relatively thick. Changing the viscosity of the entire upper mantle produces a similar effect in that progressively reducing the viscosity in this region systematically reduces the calculated decay times (as shown by the coloured horizontal lines). One exception to this trend of shorter decay times for lower viscosities is observed in the case of a 1 km thick MRL. Reductions in the viscosity of these thin MRLs often have the effect of increasing decay times, albeit usually insignificantly. This might be related to a strong lateral flow in the MRL given the vertical restriction of the layer and low viscosities involved.

On evaluating our modelling output, it is clear that decay time changes induced by MRL property variations do not occur independently of the background mantle viscosity model. The results shown in Fig. 3(a) indicate that models with relatively low UMVs are less sensitive to the properties of the layer. For example, compare the reduction in the decay times when the viscosity of the 10 km layer is reduced from 10^{16} to 10^{15} Pa·s as the background UMV is increased from 10^{20} to 9 $\times$ 10^{20} Pa·s. The decrease in decay time is progressively larger for models with a greater UMV. This behaviour is consistent with the idea that as the ratio of background to layer viscosity is increased, a greater amount of deformation will occur within the low viscosity layer, thus increasing its influence

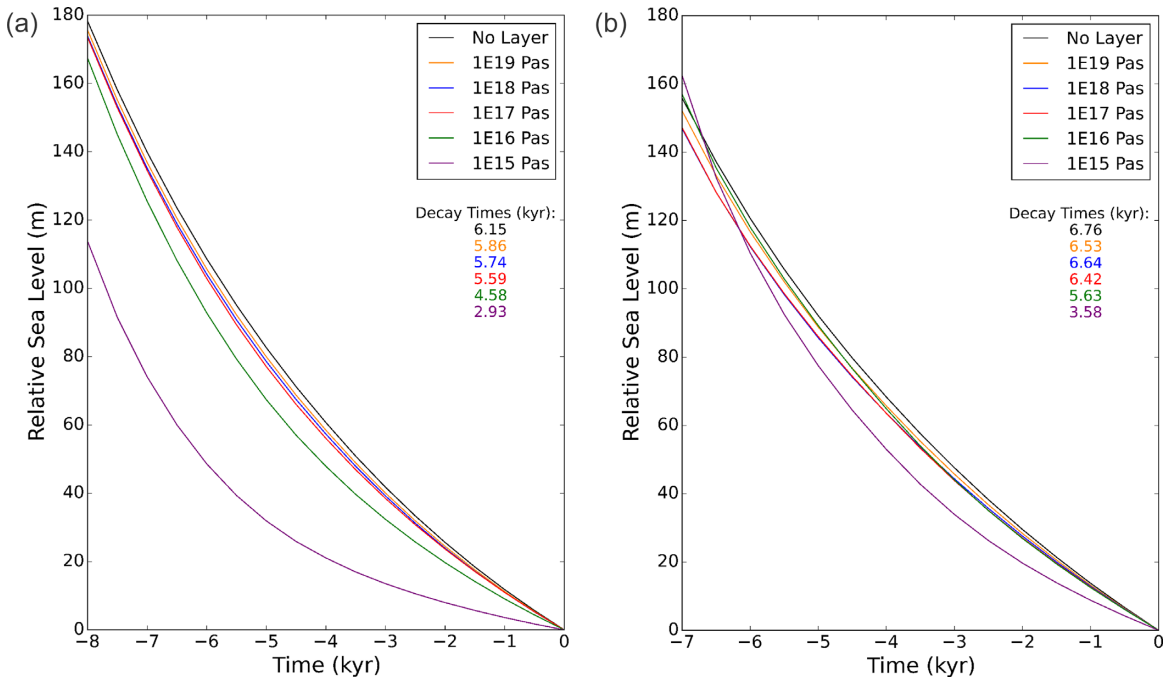

Figure 2. Modelled ice-related RSL curves for (a) ÅR and (b) RG for a 10 km thick hydrous MRL; the computed decay times for each curve are also listed according to colour. MRL viscosities are indicated in the key.

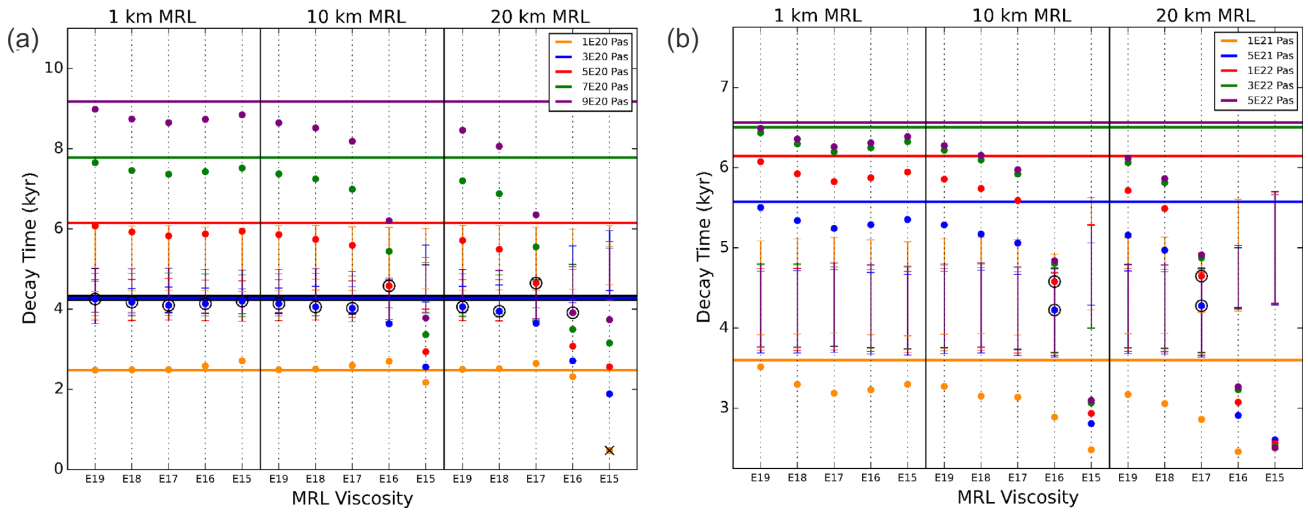

Figure 3. (a) Decay time results at ÅR for a fixed lower-mantle viscosity of 10^{22} Pa·s determined using the ICE-5G ice history model. The dots indicate the decay time values (vertical axis) for a given background viscosity (colour as indicated in key) and thickness and viscosity of an MRL (horizontal axis) just above 410 km depth. The coloured horizontal lines show the decay times for the upper-mantle viscosity values indicated in the key when no low viscosity layer is included. Model-specific observational decay time ranges ($\pm 2\sigma$) are illustrated by error bars. Decay times which satisfy observational constraints are indicated by black outlines. Decay times considered unacceptable due to non-exponential RSL curve behaviour are marked with a black 'x'. (b) As in (a) but for the case of a fixed upper-mantle viscosity of 5×10^{20} Pa·s and different values of lower-mantle viscosity (indicated in key).

on the predicted RSL curves and decay times. One illustration of this relationship can be seen in Fig. S4(A) (Supporting Information) where, for the model with the thickest MRL, the lowest decay time corresponds to an UMV of 5×10^{20} Pa·s instead of 10^{20} Pa·s as one might expect.

Fig. 3(b) shows the results for fixed UMV (5×10^{20} Pa·s) and all considered LMV values. Compared to the results in Fig. 3(a), LMV variations affect computed decay times in a manner analogous in behaviour but lesser in magnitude. Decreasing the LMV typically causes decay time reductions and diminishes sensitivity to MRL properties, albeit much less so than for varying the UMV. Due to this sensitivity reduction, models with the stiffest lower mantle exhibit the largest span of decay times, the lowest of which are produced when a 10^{15} Pa·s MRL is included.

Using the same mantle models considered in Fig. 3, we generated decay times for RG (Fig. 4). As previously explained, RG decay times should be less sensitive to MRL properties compared to ÅR due to the differences in ice load history (Mitrovica & Peltier 1991; Mitrovica 1996). Comparison of the results in Figs 3 and 4 supports this assertion: while the decay times determined for RG exhibit the same overall pattern as the results for ÅR, the magnitude of the changes incurred due to adding the MRL are smaller due to the

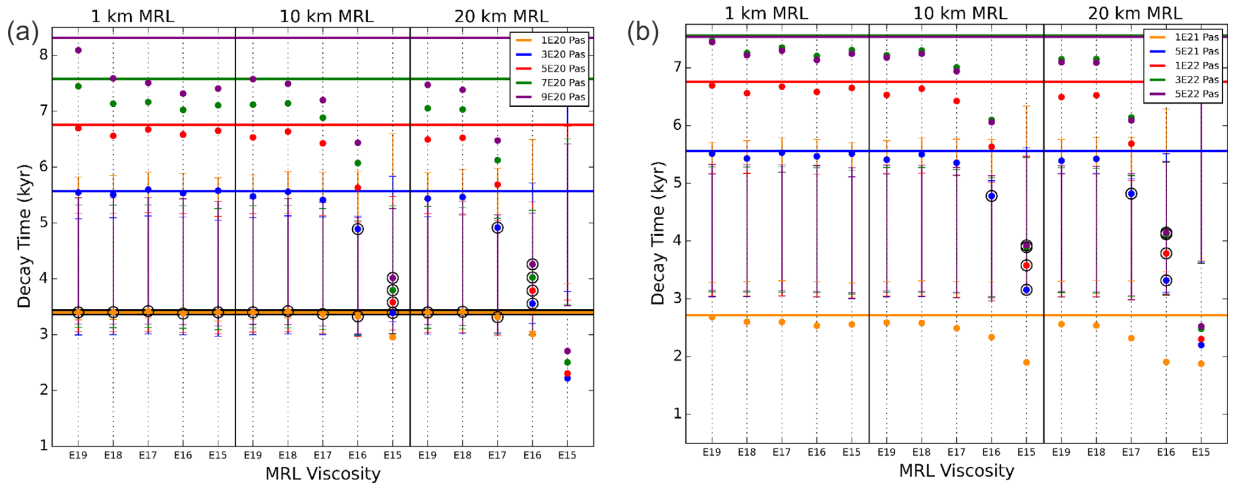

Figure 4. As Fig. 3 except for decay times determined for RG in Canada.

diminished dependence on viscosity structure at 410 km depth. With respect to background mantle models, the RG results are more readily perturbed by LMV variations relative to ÅR due to the greater depth sensitivity of the RG RSL data.

Thus far, we have considered only the sensitivity of model output to variations in Earth viscosity structure. We computed the results shown in Figs 3 and 4 for three additional ice loading histories. For ÅR, results are shown for the ANU and ICE-5G-FIS78311 ice models (Figs S2 and S3, Supporting Information, respectively); for RG, results are shown for the ANU and ICE-5G-NAIS9927 ice models (Figs S4 and S5, Supporting Information). Comparing results for ÅR for the case of a fixed LMV (Fig. 3a, and Figs S2a and S3a), it is evident that changing the ice model does impact the model output. Considering the results for which an MRL is absent (horizontal lines), the range in estimated decay times can exceed 1 kyr for viscosity models which are relatively stiff (e.g. UMV of 9×10^{20} Pa·s), but it is usually less than this value. For the three ice models considered for ÅR, the ANU model typically produced the lowest decay time and the ICE-5G-FIS78311 model the highest decay time. The changes to results for models with an MRL are similar to those which occur in MRL absence, in the sense that the estimated decay times are shifted by a similar amount when a different ice model is adopted. Consequently, regardless of ice model, the sensitivity of the results when changing MRL properties relative to a given background viscosity model is similar. Therefore, the conclusions explained above remain valid—such as models with a higher background viscosity showing greater sensitivity to changes in MRL properties.

The results for RG (Fig. 4, and Figs S4 and S5, Supporting Information) display similar ice model sensitivities in that there are clear differences as the background model is varied but the changes in decay times when MRL properties are varied relative to a given background model are similar, regardless of the adopted ice history. For this location, the ICE-5G model typically produces the greatest decay times for a given background viscosity model (compared to ICE-5G-FIS78311 for ÅR). The lowest decay times are most often given by the ICE-5G-NAIS9927 model. As noted above, the enhanced sensitivity of the results at RG to changes in LMV is evident for all three ice models considered.

The significance of the sensitivity to variations in the ice loading history can be assessed by determining by how much the subset of viscosity models that satisfy the observations (indicated by black circles in each figure) varies as the ice model is changed. It is clear on comparing the results in Figs 3 and 4, and Figs S2–S5 (Supporting Information) that the subset of models satisfying the observational constraints does change considerably between the ice models considered here at both locations (ÅR and RG). As a consequence, we only accept the viscosity models that fit the observations for all ice models considered (see Section 3.2). By doing this, we are able to incorporate uncertainty in the ice model input into our estimation of plausible MRL properties. Admittedly, our sample set of ice models is relatively small and so our estimate of the uncertainty in this GIA model input is crude.

Despite the differences in decay time sensitivity to viscosity structure between ÅR and RG, the results for both locations, regardless of the adopted ice model, are similar in terms of their sensitivity to the existence of an MRL at 410 km depth. For all background mantle models at both locations, decay times are affected most strongly by the presence of a 10 km thick, 10^{15} Pa·s layer, or a 20 km thick layer with viscosity of 10^{15}–10^{16} Pa·s. For the vast majority of mantle models, the contrast between the presence of a 1 km layer and its complete absence is within observational uncertainty, regardless of layer viscosity. For both locations, thicker and softer MRLs produce lower decay times. The exception to this, most frequently evident in the case of a 1 km thick MRL at ÅR, is a trend of increasing decay time for viscosity reductions below 10^{17} Pa·s. Again, we postulate that this reflects the influence of lateral flow within the 1 km thick low viscosity layer.

3.1.2 $\dot{J}_2$

In the case of the $\dot{J}_2$ observable, there is significantly greater dependence on variations in LMV relative to our decay time observations (see Mitrovica & Peltier 1993; Mitrovica & Forte 1997). This is readily apparent in Fig. 5. Despite this bias in sensitivity towards LMV variations, the $\dot{J}_2$ results do exhibit some sensitivity to MRL properties which differs from that of the decay times. Foremost, there is little variation between results for different layer thicknesses, indicating that $\dot{J}_2$ is not as sensitive to thickness variations of ∼10 km for the range of layer and background viscosities considered here. Furthermore, sensitivity to variations in the viscosity of the layer is non-monotonic, with $\dot{J}_2$ predictions showing an increase then decrease as the viscosity of the MRL is reduced. This non-monotonic sensitivity of $\dot{J}_2$ to mantle viscosity (particularly in

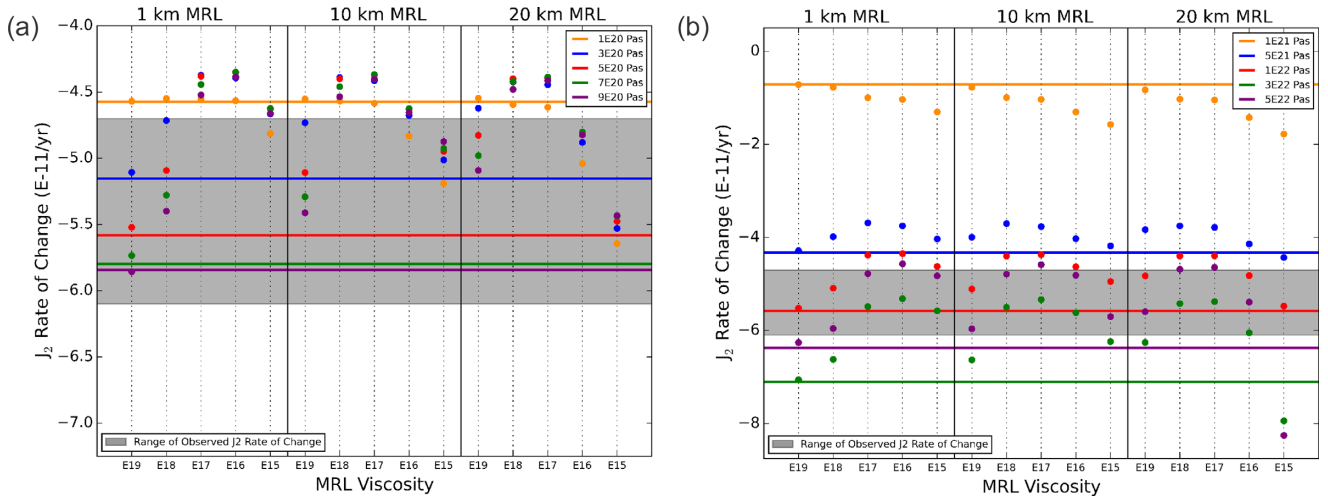

Figure 5. Predictions of $\dot{J}_2$ for a suite of Earth models with a lower-mantle viscosity of 10^{22} Pa·s determined using the ICE-5G ice history model. The dots indicate the $\dot{J}_2$ values (vertical axis) for a given background viscosity (colour as indicated in key) and thickness and viscosity of an MRL (horizontal axis) just above 410 km depth. The coloured horizontal lines show $\dot{J}_2$ values for the upper-mantle viscosity values indicated in the key when no low viscosity layer is included. (b) As in (a) but for the case of a fixed upper-mantle viscosity of 5×10^{20} Pa·s and different values of lower-mantle viscosity (indicated in key). The grey region defines the observed constraint on $\dot{J}_2$ as relating to GIA (see the main text for further information).

the lower mantle) has been noted and discussed in previous studies (e.g. Peltier 1983; Mitrovica & Peltier 1993; Milne *et al.* 1998; Nakada *et al.* 2015). This non-monotonicity can be explained as follows: relatively minor reductions in MRL viscosity cause the rate of isostatic relaxation to take place more rapidly since the end of major ice melting (∼7 kyr BP) to present, resulting in increased $\dot{J}_2$ values from then to the present. However, more extreme MRL viscosity reductions accelerate the solid Earth relaxation such that most of the isostatic recovery from past glacial loading occurs prior to the measurement of the modern $\dot{J}_2$ value, resulting in relatively low rates of change at present.

In spite of the differences between decay time and $\dot{J}_2$ results, they do share one feature: both are less affected by layer properties in cases of lower viscosity background mantle models, with $\dot{J}_2$ being particularly dependent on the lower mantle in this regard. While relatively low values of UMV still cause diminished MRL sensitivity, this effect is subordinate to that of the lower mantle. Assessing overall sensitivity of the $\dot{J}_2$ observable to MRL properties, it is apparent that there is greater sensitivity to changes in MRL viscosity compared to thickness. None of the models depicted in Fig. 5(b) are significantly affected by MRLs with viscosity of 10^{19} Pa·s. For MRLs with viscosities $\leq 10^{18}$ Pa·s, trends become more complex. For viscosities of 10^{18}–10^{16} Pa·s, sensitivity is often evident for relatively stiff (higher viscosity) background mantle models. The softest layers (10^{15} Pa·s) exhibit the greatest variations in behaviour, with some yielding $\dot{J}_2$ values close to that of the layer-free background model (e.g. 10 km MRL for the 3×10^{20} Pa·s upper mantle in Fig. 5a; 10 km MRL for the 5×10^{21} Pa·s lower mantle, and 20 km MRL for the 10^{22} Pa·s lower mantle in Fig. 5b), and others producing the greatest deviations from the background model (e.g. all MRL thicknesses for the 1×10^{20} Pa·s upper mantle in Fig. 5a). Due to the non-monotonic behaviour of the results, $\dot{J}_2$ values determined for low viscosity layers may not deviate significantly from that of the background mantle model, despite sensitivity being evident for stiffer layers, leading to a non-uniqueness issue for this particular datum.

The sensitivity of $\dot{J}_2$ to ice model input can be assessed by comparing Fig. 5, and Figs S6 and S7 (Supporting Information). We do not consider the ICE-5G-FIS78311 model in this case as the influence of the North American ice sheets will be more significant on $\dot{J}_2$ given their greater volume and spatial extent. In a similar fashion to the decay time results, the differences are dominated by a shift in the rates associated with a given background viscosity model. In this case, the ANU model produces rates that are generally greater in magnitude than those for the two other models (which give similar results since only the North American component differs between the two). This stronger GIA contribution from the ANU model is likely dominated by the larger deglacial mass loss from Antarctica in this model (∼10 m of sea-level equivalent more than in the ICE-5G Antarctic component). The variation in the model output associated with changes in MRL properties is similar between the different ice models. When comparing the model output to the observed $\dot{J}_2$ value, it is clear that a different subset of models fit the data for a given ice model. This is particularly evident for the case of a fixed LMV of 10^{22} Pa·s, where the lower values given by the ANU model result in a significantly larger number of models falling within the observed range. This will be discussed further in Section 3.2.

3.2 Constraining viscosity structure

Our sensitivity analysis indicates that, to address the primary aim of this study, it is necessary to consider the viscosity of the entire mantle (not only that of an MRL at the top of the transition zone) as well as a suite of ice histories. In this section, we use our model output—a subset of which is shown in Figs 3–5, and Figs S2–S7 (Supporting Information)—to determine whether the GIA-related observables considered here are compatible with the presence of such a layer and, if so, seek to place constraints on its thickness and/or viscosity. Since we considered only a limited subset of plausible viscosity structures (background and for the MRL), our final conclusions in this regard will be incomplete. However, we believe that a sufficient range of parameters were explored to address the primary aim and provide a set of results that future studies can build upon.

We begin by considering the decay time results which provide constraints on viscosity structure beneath ÅR and RG. Table S2 (Supporting Information) shows the subset of 13 viscosity models that were compatible with the estimated ÅR decay times for all three ice models (ICE-5G, ANU and ICE-5G-FIS78311). As noted above, by accepting only viscosity models that fit the observational constraints regardless of the adopted ice model, we are able to account (albeit crudely) for uncertainty in this GIA model input. The accepted viscosity models at ÅR consist generally of two 'background' mantle model configurations: either 3×10^{20} Pa·s UMV and one of the two stiffest LMVs, or 10^{21} Pa·s LMV and one of the two stiffest UMVs. The acceptance of these two configurations illustrates the trade-off between UMV and LMV, and the non-uniqueness which inevitably results from it. The change required by each of these parameters for equivalent trade-off reflects the greater sensitivity of decay times in this region to the UMV relative to the LMV (Mitrovica 1996; Lau *et al.* 2016). Of the two identified general background mantle configurations, the combination of 3×10^{20} Pa·s UMV and a stiff LMV is compatible with previous viscosity estimates based on the ÅR decay time constraint (e.g. Nordman *et al.* 2015; Lau *et al.* 2016).

As for the role of an MRL, only the combination of the stiffest UMV and weakest LMV permit the presence of an MRL of 10 km or thicker. All other accepted viscosity models at ÅR require a 1 km MRL at most. Of the accepted models which allow MRL presence, all but one require an MRL viscosity of 10^{18} Pa·s or greater. The single instance of a 10^{17} Pa·s MRL viscosity is seen for a 1 km layer thickness. Given the ice and Earth model parameter set considered here, decay time estimates from ÅR RSL observations are unable to uniquely support or refute the existence of an MRL in this region. However, these results do suggest that if such a layer exists its viscosity should be no less than $\sim 10^{17}$ Pa·s. Additionally, thicker layers (10 and 20 km) are restricted further to viscosities of at least 10^{18} Pa·s.

Despite having much larger ranges of decay time uncertainty (compare observational ranges in Tables S2 and S3, Supporting Information), the constraints at RG are compatible with only a slightly greater number of viscosity models (15) as compared to ÅR. The majority of the viscosity models accepted at RG consist of both a 3×10^{20} Pa·s UMV and 5×10^{21} Pa·s LMV. There are a total of four models which differ slightly from this configuration, half of which involve changing the UMV to 5×10^{20} Pa·s, while the other half switch the LMV to 10^{22} Pa·s. Although these two possible mantle viscosity deviations must occur exclusive to one another, they both require the presence of a 10 km MRL (10^{16} Pa·s) or a 20 km MRL (10^{17} Pa·s). Similarly to ÅR, this array of permitted viscosity structures clearly demonstrates the influence of parameter trade-offs in our model output. A stiffening of the background mantle (either UMV or LMV) must be compensated by the inclusion of a significant MRL. Within said MRL, an increase in thickness must be neutralized by an increase in the MRL viscosity (or decrease in the difference between MRL and background UM viscosity). Likewise, a UMV increase must be balanced by an LMV decrease of greater magnitude in order to remain in the permitted decay time range. The greater LMV sensitivity of RG is well illustrated here as the magnitude of LMV change required to offset an opposing UMV change is less extreme compared to ÅR.

Among all permitted MRL properties at RG, 10 km layers are restricted to 10^{16} Pa·s or greater, whereas 20 km layers are restricted to 10^{17} Pa·s or greater. Conversely, all viscosities are possible for a 1 km MRL. There are a total of three possible background mantle viscosity configurations for RG, only one of which allows either a 1 km MRL or MRL absence. Curiously, among the four possible mantle viscosity configurations at ÅR, none are in agreement with those of RG. Their only similarity is compatibility with a 3×10^{20} Pa·s UMV, but even that is within the context of significantly different LMV values. Among the 400 possible viscosity structures considered in this study, none simultaneously satisfy the constraints of the decay times from both locations. This complete lack of overlap between location-specific results demonstrates that the observational data do not support consistent Earth viscosity structure in these two regions. However, what these two regions do have in common is the allowance of any of the considered MRL thicknesses. With respect to MRL viscosity, RG is slightly more permissive. It can accommodate MRL viscosities 1–2 o.o.m. less than those of ÅR for equivalent thicknesses.

Due to its significantly greater LMV dependence, the $\dot{J}_2$ datum provides a constraint that is distinct and complementary to those of the decay times. The viscosity constraint cannot be associated with a specific region but instead reflects Earth deformation at the global scale associated with loading focused in all glaciated regions, in addition to the more subtle ocean loading associated with the increase and redistribution of ocean mass since the last glacial maximum. A total of 63 viscosity models were compatible with the observational estimate adopted here (Table S4, Supporting Information). While all of the considered UMV values are included in this 63 model subset, with an approximately even distribution across the 5 values, only LMV values greater than or equal to 10^{22} Pa·s are present. In the set of accepted LMV values, only 10 are 10^{22} Pa·s and so the $\dot{J}_2$ datum clearly prefers relatively high values of this parameter. The reason for this is evident in Fig. 5, and Figs S6 and S7 (Supporting Information), which show that the predicted value is consistently too large for LMV values of 1 and 5×10^{21} Pa·s (except for the case of the ANU model due to its large Antarctic mass loss). The finding that this observable prefers relatively high values of LMV is compatible with the results of previous analyses (e.g. Nakada *et al.* 2015; Lau *et al.* 2016).

All of the accepted viscosity models, with the exception of one, include an MRL. From the results in Table S4 (Supporting Information), there is no strong bias to a given thickness or viscosity of the MRL for the range of background viscosities considered. These results demonstrate that the utility of $\dot{J}_2$ as a constraint is greatest for seeking to determine LMV. With respect to the MRL itself, $\dot{J}_2$ is far more sensitive to MRL viscosity than thickness, and thus could be used to constrain the former property most effectively. Particularly if the values of other parameters (e.g. LMV) can be more precisely constrained using other methods and/or data sets.

In testing this broad array of Earth models, we find that none of the considered viscosity structures can satisfy the observational restrictions of both ÅR and RG. The results provided by these two locations are regional in nature and so the lack of agreement is not unexpected. Additionally, the global $\dot{J}_2$ observable would likely refute any model found to be permitted by both regions. The strong preference of the $\dot{J}_2$ observable for stiffer LMV values eliminates all viscosity structures considered valid for RG, and all but one for ÅR. Of course, as noted above, our viscosity model subset is incomplete in terms of the depth parameterisations and viscosity values considered. This limitation should be borne in mind when interpreting our results.

4 CONCLUSIONS

We have presented a sensitivity analysis aimed at testing whether observables related to GIA can support or refute the widespread existence of a low viscosity MRL located above the mantle transition zone (Bercovici & Karato 2003). In total, 1600 model runs were performed sampling a range of MRL thicknesses and viscosities, plausible viscosity values in the upper and lower mantle, and four different global ice histories. Our model output shows that postglacial decay times (estimated at ÅR, Sweden and RG, Canada) and $\dot{J}_2$ are sensitive to the existence of an MRL and reasonable variations in its thickness (1–20 km) and viscosity (10^{15}–10^{19} Pa·s). The magnitude and nature of this sensitivity varies between the two data types as well as the adopted background viscosity structure (i.e. within the upper- and lower-mantle regions).

Comparing model output to observations of postglacial decay times and $\dot{J}_2$, we conclude that a number of solutions are possible, largely as a result of parameter trade-off. The decay time observations for both ÅR and RG do not uniquely support or exclude the existence of an MRL in this region. However, they do both offer constraints on MRL viscosity for given thicknesses. ÅR is more restrictive than RG in this regard. RG constraints allow MRL viscosities as low as 10^{16} and 10^{17} Pa·s for 10 and 20 km layers, respectively. The ÅR results narrow these permitted viscosity ranges to between 10^{18} and 10^{19} Pa·s for both 10 and 20 km MRL thicknesses. For models with a 1 km thick MRL, ÅR constraints allow a minimum viscosity of 10^{17} Pa·s, whereas those of RG permit any value within the explored range. With respect to 'background' mantle viscosity, the RG observations can only be satisfied by UMV values of 3–5 $\times$ 10^{20} Pa·s and LMV values of 5–10 $\times$ 10^{21} Pa·s. Conversely, ÅR results depict two satisfactory mantle viscosity configurations: either an LMV of 10^{21} Pa·s and a stiff UMV (7–9 $\times$ 10^{20} Pa·s), or a UMV of 3 $\times$ 10^{20} Pa·s and a stiff LMV (3–5 $\times$ 10^{22} Pa·s). The latter of these configurations is compatible with results from a recent study (Lau *et al.* 2016).

Finally, comparing model output to the observed $\dot{J}_2$ value (with the effect of recent ice melting removed) did not provide any constraints on MRL properties. However, our results show that this observable has a strong preference for viscosity values in the lower mantle that are equal to or greater than 10^{22} Pa·s, as found in other recent studies (Nakada *et al.* 2015; Lau *et al.* 2016).

REFERENCES

Benz, H.M. & McCarthy, J., 1994. Evidence for an upper mantle low velocity zone beneath the southern Basin and Range-Colorado Plateau transition zone, *Geophys. Res. Lett.,* **21**(7), 509–512.

Bercovici, D. & Karato, S.-I., 2003. Whole-mantle convection and the transition zone water filter, *Nature,* **425,** 39–44.

Boggs, P.T., Byrd, R.H., Rogers, J.E. & Schnabel, R.B., 1992. *User's Reference Guide for ODRPACK Version 2.01 Software for Weighted Orthogonal Distance Regression,* Computing and Applied Mathematics Laboratory, U.S. Department of Commerce, Gaithersburg, MD.

Boggs, P.T., Donaldson, J.R., Byrd, R.H. & Schnabel, R.B., 1989. ALGORITHM 676 ODRPACK: software for weighted orthogonal distance regression, *ACM Trans. Math. Softw.,* **15**(4), 348–364.

Chen, J., Liu, H. & Girard, J., 2011. Comparative in-situ X-ray diffraction study of San Carlos olivine: influence of water on the 410 km seismic velocity jump in Earth's mantle, *Am. Mineral.,* **96,** 697–702.

Chu, R., Schmandt, B. & Helmberger, D.V., 2012. Upper mantle *P* velocity structure beneath the Midwestern United States derived from triplicated waveforms, *Geochem. Geophys. Geosyst.,* **13,** Q0AK04, doi:10.1029/2011GC003818.

Courtier, A.M. & Revenaugh, J., 2007. Deep upper-mantle melting beneath the Tasman and Coral Seas detected with multiple *ScS* reverberations, *Earth planet. Sci. Lett.,* **259,** 66–76.

Dziewonski, A.M. & Anderson, D.L., 1981. Preliminary reference Earth model, *Phys. Earth planet. Inter.,* **25**(4), 297–356.

Fang, M. & Hager, B.H., 2002. On the apparent exponential relaxation curves at the central regions of the Late Pleistocene ice sheets, in *Ice Sheets, Sea Level and the Dynamic Earth,* pp. 201–218, eds Mitrovica, J.X. & Vermeersen, L.L.A., American Geophysical Union.

Gao, W., Matzel, E. & Grand, S.P., 2006. Upper mantle seismic structure beneath eastern Mexico determined from P and S waveform inversion and its implications, *J. geophys. Res.,* **111,** B08307, doi:10.1029/2006JB004304.

Gilbert, H.J., Sheehan, A.F., Dueker, K.G. & Molnar, P., 2003. Receiver functions in the western United States, with implications for upper mantle structure and dynamics, *J. geophys. Res.,* **108**(B5), 2229, doi:10.1029/2001JB001194.

Hae, R., Ohtani, E., Kubo, T., Koyama, T. & Utada, H., 2006. Hydrogen diffusivity in wadsleyite and water distribution in the mantle transition zone, *Earth planet. Sci. Lett.,* **243,** 141–148.

Han, H.K. & Gomez, N., 2018. The impact of water loading on postglacial decay times in Hudson Bay, *Earth planet. Sci. Lett.,* **489,** 1–10.

Hardy, L., 1976. *Contribution à l'étude Géomorphologique de la Portion Québécoise des Basses Terres de la Baie de James,* PhD Thesis, McGill University, Canada.

Hardy, L., 1977. La déglaciation et les épisodes lacustre et marin sur les versants de la partie québécoise des basses terres de la baie de James, *Géog. Phys. Quat.,* **31,** 261–273.

Hier-Majumder, S. & Courtier, A., 2011. Seismic signature of small melt fraction atop the transition zone, *Earth planet. Sci. Lett.,* **308,** 334–342.

Hillaire-Marcel, C., 1976. La déglaciation et le relèvement isostatique sur la côte est de la baie d'Hudson, *Cah. Géog. Québec,* **20,** 185–220.

Hirschmann, M.M., 2006. Water, melting, and the deep earth H_2O cycle, *Annu. Rev. Earth planet. Sci.,* **34,** 629–653.

Hirschmann, M.M., Aubaud, C. & Withers, A.C., 2005. Storage capacity of H_2O in nominally anhydrous minerals in the upper mantle, *Earth planet. Sci. Lett.,* **236,** 167–181.

Hirth, G. & Kohlstedt, D.L., 1995a. Experimental constraints on the dynamics of the partially molten upper mantle: deformation in the diffusion creep regime, *J. geophys. Res.,* **100**(B2), 1981–2001.

Hirth, G. & Kohlstedt, D.L., 1995b. Experimental constraints on the dynamics of the partially molten upper mantle: 2. deformation in the dislocation creep regime, *J. geophys. Res.,* **100**(B8), 15441–15449.

Houser, C., 2016. Global seismic data reveal little water in the mantle transition zone, *Earth planet. Sci. Lett.,* **448,** 94–101.

Jasbinsek, J. & Dueker, K., 2007. Ubiquitous low-velocity layer atop the 410-km discontinuity in the northern Rocky Mountains, *Geochem. Geophys. Geosyst.,* **8,** Q10004, doi:10.1029/2007GC001661.

Jasbinsek, J.J., Dueker, K.G. & Hansen, S.M., 2010. Characterizing the 410 km discontinuity low-velocity layer beneath the LA RISTRA array in the North American Southwest, *Geochem. Geophys. Geosyst.,* **11,** Q03008, doi:10.1029/2009GC002836.

Karato, S.-I., 2011. Water distribution across the mantle transition zone and its implications for global material circulation, *Earth planet. Sci. Lett.,* **301,** 413–423.

Karato, S.-I., 2014. Does partial melting explain geophysical anomalies? *Phys. Earth planet. Inter.,* **228,** 300–306.

Karato, S.-I., Bercovici, D., Leahy, G., Richard, G. & Jing, Z., 2006. The transition-zone water filter model for global material circulation: Where do we stand?in *Earth's Deep Water Cycle,* pp. 289–313, eds Jacobsen, S.D. & Van Der Lee, S., American Geophysical Union.

Kendall, R.A., Mitrovica, J.X. & Milne, G.A., 2005. On post-glacial sea level—II. Numerical formulation and comparative results on spherically symmetric models, *Geophys. J. Int.,* **161**(3), 679–706.

Kohlstedt, D.L. & Zimmerman, M.E., 1996. Rheology of partially molten mantle rocks, *Annu. Rev. Earth planet. Sci.,* **24,** 41–62.

Lambeck, K., 1993. Glacial rebound of the British Isles-11. A high resolution, high-precision model, *Geophys. J. Int.,* **115,** 960–990.

Lambeck, K., Smither, C. & Johnston, P., 1998. Sea level change, glacial rebound and mantle viscosity for northern Europe, *Geophys. J. Int.,* **134**(1), 102–144.

Lambeck, K., Rouby, H, Purcell, A, Sun, Y. & Sambridge, M., 2014. Sea level and global ice volumes from the last glacial maximum to the holocene, *Proc. Natl. Acad. Sci.,* **111**(43), 15296–15303.

Lambeck, K., Purcell, A. & Zhao, S., 2017. The North American Late Wisconsin ice sheet and mantle viscosity from glacial rebound analyses, *Quat. Sci. Rev.,* **158,** 172–210.

Lau, H.C.P., Mitrovica, J.X., Austermann, J., Al-Attar, D., Crawford, O. & Latychev, K., 2016. Inferences of mantle viscosity based on ice age data sets: Radial structure, *J. geophys. Res.,* **121**(10), 6991–7012.

Leahy, G. & Bercovici, D., 2010. Reactive infiltration of hydrous melt above the mantle transition zone, *J. geophys. Res.,* **115,** B08406, doi:10.1029/2009JB006757.

Litasov, K., Ohtani, E., Kagi, H., Jacobsen, S.D. & Ghosh, S., 2007. Temperature dependence and mechanism of hydrogen incorporation in olivine at 12.5 – 14.0 GPa, *Geophys. Res. Lett.,* **34,** L16314, doi:10.1029/2007GL030737.

Litasov, K.D., Shatskiy, A., Ohtani, E. & Katsura, T., 2011. Systematic study of hydrogen incorporation into Fe-free wadsleyite, *Phys. Chem. Miner.,* **38**(1), 75–84.

Liu, Z., Park, J. & Karato, S.-I., 2016. Seismological detection of low-velocity anomalies surrounding the mantle transition zone in Japan subduction zone, *Geophys. Res. Lett.,* **43**(6), 2480–2487.

Matsukage, K.N., Jing, Z. & Karato, S.-I., 2005. Density of hydrous silicate melt at the conditions of Earth's deep upper mantle, *Nature,* **438,** 488–491.

Métivier, L., Caron, L., Greff-Lefftz, M., Pajot-Métivier, G., Fleitout, L. & Rouby, H., 2016. Evidence for postglacial signatures in gravity gradients: a clue in lower mantle viscosity, *Earth planet. Sci. Lett.,* **452,** 146–156.

Milne, G.A. & Mitrovica, J.X., 1998. Postglacial sea-level change on a rotating Earth, *Geophys. J. Int.,* **133**(1), 1–19.

Milne, G.A., Mitrovica, J.X. & Forte, A.M., 1998. The sensitivity of glacial isostatic adjustment predictions to a low-viscosity layer at the base of the upper mantle, *Earth planet. Sci. Lett.,* **154,** 265–278.

Mitrovica, J.X., 1996. Haskell [1935]revisited, *J. geophys. Res.,* **101**(B1), 555–569.

Mitrovica, J.X. & Forte, A.M., 1997. Radial profile of mantle viscosity: results from the joint inversion of convection and postglacial rebound observables, *J. geophys. Res.,* **102**(B2), 2751–2769.

Mitrovica, J.X. & Forte, A.M., 2004. A new inference of mantle viscosity based upon joint inversion of convection and glacial isostatic adjustment data, *Earth planet. Sci. Lett.,* **225,** 177–189.

Mitrovica, J.X., Forte, A.M. & Simons, M., 2000. A reappraisal of postglacial decay times from Richmond Gulf and James Bay, Canada, *Geophys. J. Int.,* **142**(3), 783–800.

Mitrovica, J.X. & Milne, G.A., 2002. On the origin of postglacial ocean syphoning, *Quat. Sci. Rev.,* **21,** 2179–2190.

Mitrovica, J.X. & Milne, G.A., 2003. On post-glacial sea level: I. General theory, *Geophys. J. Int.,* **154**(2), 253–267.

Mitrovica, J.X. & Peltier, W.R., 1991. A complete formalism for the inversion of post-glacial rebound data: resolving power analysis, *Geophys. J. Int.,* **104**(2), 267–288.

Mitrovica, J.X. & Peltier, W.R., 1993. Present-day secular variations in the zonal harmonics of Earth's geopotential, *J. geophys. Res.,* **98**(B3), 4509–4526.

Mitrovica, J.X. & Peltier, W.R., 1995. Constraints on mantle viscosity based upon the inversion of post-glacial uplift data from the Hudson Bay region, *Geophys. J. Int.,* **122**(2), 353–377.

Mitrovica, J.X., Wahr, J., Matsuyama, I. & Paulson, A., 2005. The rotational stability of an ice-age Earth, *Geophys. J. Int.,* **161**(2), 491–506.

Nakada, M., Okuno, J., Lambeck, K. & Purcell, A., 2015. Viscosity structure of Earth's mantle inferred from rotational variations due to GIA process and recent melting events, *Geophys. J. Int.,* **202**(2), 976–992.

Nordman, M., Milne, G. & Tarasov, L., 2015. Reappraisal of the Angerman River decay time estimate and its application to determine uncertainty in Earth viscosity structure, *Geophys. J. Int.,* **201**(2), 811–822.

Ohtani, E., Amaike, Y., Kamada, S., Ohira, I. & Mashino, I., 2016. Stability of hydrous minerals and water reservoirs in the deep Earth interior, in *Deep Earth: Physics and Chemistry of the Lower Mantle and Core,* pp. 265–275, eds Terasaki, H. & Fischer, R.A., American Geophysical Union.

Ohtani, E., Litasov, K., Hosoya, T., Kubo, T. & Kondo, T., 2004. Water transport into the deep mantle and formation of a hydrous transition zone, *Phys. Earth planet. Inter.,* **143–144,** 255–269.

Paulson, A. & Richards, M.A., 2009. On the resolution of radial viscosity structure in modelling long-wavelength postglacial rebound data, *Geophys. J. Int.,* **179,** 1516–1526.

Pearson, D.G. *et al.*, 2014. Hydrous mantle transition zone indicated by ringwoodite included within diamond, *Nature,* **507,** 221–224.

Peltier, W.R., 1974. The impulse response of a Maxwell Earth, *Rev. Geophys.,* **12**(4), 649–669.

Peltier, W.R., 1983. Constraints on deep mantle viscosity from LAGEOS acceleration data, *Nature,* **304,** 434–436.

Peltier, W.R., 1998. Postglacial variations in the level of the sea: implications for climate dynamics and solid-earth geophysics, *Rev. Geophys.,* **36**(4), 603–689.

Peltier, W.R., 2004. Global glacial isostasy and the surface of the ice-age Earth: the ICE-5 G (VM2) model and GRACE, *Ann. Rev. Earth planet. Sci.,* **32,** 111–149.

Peltier, W.R. & Andrews, J.T., 1976. Glacial-isostatic adjustment—I. The forward problem, *Geophys. J. R. astr. Soc.,* **46,** 605–646.

Pendea, I.F., Costopoulos, A., Nielsen, C. & Chmura, G.L., 2010. A new shoreline displacement model for the last 7 ka from eastern James Bay, Canada, *Quat. Res.,* **73**(3), 474–484.

Reimer, P.J. *et al.*, 2013. IntCal13 and Marine13 radiocarbon age calibration curves 0–50,000 years cal BP, *Radiocarbon,* **55**(4), 1869–1887.

Revenaugh, J. & Sipkin, S.A., 1994. Seismic evidence for silicate melt atop the 410-km mantle discontinuity, *Nature,* **369,** 474–476.

Schaeffer, A.J. & Bostock, M.G., 2010. A low-velocity zone atop the transition zone in northwestern Canada, *J. geophys. Res.,* **115,** B06302, doi:10.1029/2009JB006856.

Schmandt, B., Dueker, K.G., Hansen, S.M., Jasbinsek, J.J. & Zhang, Z., 2011. A sporadic low-velocity layer atop the western U.S. mantle transition zone and short-wavelength variations in transition zone discontinuities, *Geochem. Geophys. Geosyst.,* **12,** Q08014, doi:10.1029/2011GC003668.

Schmerr, N. & Garnero, E.J., 2007. Upper mantle discontinuity topography from thermal and chemical heterogeneity, *Science,* **318**(5850), 623–626.

Soldati, G., Boschi, L., Deschamps, F. & Giardini, D., 2009. Inferring radial models of mantle viscosity from gravity (GRACE) data and an evolutionary algorithm, *Phys. Earth planet. Inter.,* **176,** 19–32.

Stuiver, M. & Reimer, P.J., 1993. Extended C-14 database and revised Calib 3.0 C-14 age calibration program, *Radiocarbon,* **35**(1), 215–230.

Tarasov, L., 2013. GLAC-1b: a new data-constrained global deglacial ice sheet reconstruction from glaciological modelling and the challenge of missing ice, in *European Geophysical Union General Assembly 2013, Abstracts,* **15,** EGU2013–12342.

Tarasov, L., Dyke, A.S., Neal, R.M. & Peltier, W., 2012. A data-calibrated distribution of deglacial chronologies for the North American ice complex from glaciological modeling, *Earth planet. Sci. Lett.,* **315–316,** 30–40.

Tauzin, B., Debayle, E. & Wittlinger, G., 2010. Seismic evidence for a global low-velocity layer within the Earth's upper mantle, *Nat. Geosci.,* **3,** 718–721.

Thio, V., Cobden, L. & Trampert, J., 2016. Seismic signature of a hydrous mantle transition zone, *Phys. Earth planet. Inter.,* **250,** 46–63.

Trupin, A.S., Meier, M.F. & Wahr, J.M., 1992. Effect of melting glaciers on the Earth's rotation and gravitational field: 1965–1984, *Geophys. J. Int.,* **108,** 1–15.

Vaughan, P.J. & Coe, R.S., 1981. Creep mechanism in Mg_2GeO_4: effects of a phase transition, *J. geophys. Res.,* **86**(B1), 389–404.

Vinnik, L., Ren, Y., Stutzmann, E., Farra, V. & Kiselev, S., 2010. Observations of *S*410*p* and *S*350*p* phases at seismograph stations in California, *J. geophys. Res.,* **115,** B05303, doi:10.1029/2009JB006582.

Wahr, J., Dazhong, H., Trupin, A. & Lindqvist, V., 1993. Secular changes in rotation and gravity: Evidence of post-glacial rebound or of changes in polar ice? *Adv. Space Res.,* **13**(11), 257–269.

Walcott, R.I., 1972. Late Quaternary vertical movements in Eastern North America: quantitative evidence for glacio-isostatic rebound, *Rev. Geophys. Space Phys.,* **10**(4), 849–884.

Walcott, R.I., 1980. Rheological models and observational data of glacio-isostatic rebound, in *Earth Rheology, Isostasy and Eustasy,* pp. 3–10, ed. Morner, N.-A., John Wiley.

Warren, J.M. & Hirth, G., 2006. Grain size sensitive deformation mechanisms in naturally deformed peridotites, *Earth planet. Sci. Lett.,* **248,** 423–435.

Wu, P. & Peltier, W.R., 1982. Viscous gravitational relaxation, *Geophys. J. R. astr. Soc.,* **70,** 435–485.

Wu, P. & Peltier, W.R., 1983. Glacial isostatic adjustment and the free air gravity anomaly as a constraint on deep mantle viscosity, *Geophys. J. R. astr. Soc.,* **74,** 377–449.

Yoder, C.F. & Ivins, E.R., 1985. Changes in the Earth's gravity field from Pleistocene deglaciation and present-day glacial melting, *EOS, Trans. Am. geophys. Un.,* **66**(18), 245.

Yoshino, T., Nishihara, Y. & Karato, S.-I., 2007. Complete wetting of olivine grain boundaries by a hydrous melt near the mantle transition zone, *Earth planet. Sci. Lett.,* **256,** 466–472.

Yoder, C.F., Williams, J.G., Dickey, J.O., Schutz, B.E., Eanes, R.J. & Tapley, B.D., 1983. Secular variations of Earth's gravitational harmonic J_2 coefficient from Lageos and nontidal acceleration of Earth rotation. *Nature,* **303,** 757–762.

SUPPORTING INFORMATION

Supplementary data are available at *GJI* online.

Table S1. RG observational RSL data aggregated by Mitrovica *et al.* (2000). Calibrated ages determined using the Reimer *et al.* (2013) marine calibration curve and the Calib 3.0 software (Stuiver & Reimer 1993).

Table S2. Decay time results at ÅR for Earth viscosity models where the observational constraint is satisfied for all three considered ice histories. Upper- and lower-mantle viscosities are given in units of 10^{21} Pa·s, and decay times are stated in kyr. MRL viscosity is expressed as an o.o.m., with the exception of 'NA' which indicates that MRL viscosity is not applicable in cases where the MRL thickness is zero.

Table S3. As Table S2, but for decay time results at RG.

Table S4. $\dot{J}_2$ results for Earth viscosity models where the observational constraint is satisfied for all three considered ice histories. Upper- and lower-mantle viscosities are given in units of 10^{21} Pa·s. MRL viscosity is expressed as an o.o.m., with the exception of 'NA' which indicates that MRL viscosity is not applicable in cases where the MRL thickness is zero. The observed $\dot{J}_2$ range is -5.4 $\pm$ 0.7 (2σ). All $\dot{J}_2$ values stated here are in units of 10^{-11} yr^{-1}.

Figure S1. Examples of non-exponential modelled ice-related RSL curves determined using the ICE-5G-FIS78311 ice history model at ÅR for a 10^{20} Pa·s upper-mantle viscosity, 10^{21} Pa·s lower-mantle viscosity, and a 10 km thick hydrous MRL. MRL viscosities are indicated in the key.

Figure S2. (a) Decay time results at ÅR for a fixed lower-mantle viscosity of 10^{22} Pa·s determined using the ANU ice history model. The dots indicate the decay time values (vertical axis) for a given background viscosity (colour as indicated in key) and thickness and viscosity of an MRL (horizontal axis) just above 410 km depth. The coloured horizontal lines show the decay times for the upper-mantle viscosity values indicated in the key when no low viscosity layer is included. Model-specific observational decay time ranges ($\pm$ 2σ) are illustrated by error bars. Decay times which satisfy observational constraints are indicated by black outlines. Decay times considered unacceptable due to non-exponential RSL curve behaviour are marked with a black 'x'. (b) As in (a), but for the case of a fixed upper-mantle viscosity of 5×10^{20} Pa·s and different values of lower-mantle viscosity (indicated in key).

Figure S3. As Fig. S2 except for decay times determined using the ICE-5G-FIS78311 ice history model.

Figure S4. (a) Decay time results at RG for a fixed lower-mantle viscosity of 10^{22} Pa·s determined using the ANU ice history model. The dots indicate the decay time values (vertical axis) for a given background viscosity (colour as indicated in key) and thickness and viscosity of an MRL (horizontal axis) just above 410 km depth. The coloured horizontal lines show the decay times for the upper-mantle viscosity values indicated in the key when no low viscosity layer is included. Model-specific observational decay time ranges ($\pm$ 2σ) are illustrated by error bars. Decay times which satisfy observational constraints are indicated by black outlines. Decay times considered unacceptable due to non-exponential RSL curve behaviour are marked with a black 'x'. (b) As in (a), but for the case of a fixed upper-mantle viscosity of 5×10^{20} Pa·s and different values of lower-mantle viscosity (indicated in key).

Figure S5. As Fig. S4 except for decay times determined using the ICE-5G-NAIS9927 ice history model.

Figure S6. Predictions of $\dot{J}_2$ for a suite of Earth models with a lower-mantle viscosity of 10^{22} Pa·s determined using the ANU ice history model. The dots indicate the $\dot{J}_2$ values (vertical axis) for a given background viscosity (colour as indicated in key) and thickness and viscosity of an MRL (horizontal axis) just above 410 km depth. The coloured horizontal lines show $\dot{J}_2$ values for the upper-mantle viscosity values indicated in the key when no low viscosity layer is included. (b) As in (a), but for the case of a fixed upper-mantle viscosity of 5×10^{20} Pa·s and different values of lower-mantle viscosity (indicated in key). The grey region defines the observed constraint on $\dot{J}_2$ as relating to GIA (see the main text for further information).

Figure S7. As Fig. S6 except for predictions of $\dot{J}_2$ determined using the ICE-5G-NAIS9927 ice history model.

Please note: Oxford University Press is not responsible for the content or functionality of any supporting materials supplied by the authors. Any queries (other than missing material) should be directed to the corresponding author for the article.

Supplementary Section: Sensitivity of Glacial Isostatic Adjustment to a Partially Molten Layer at 410 km Depth

Alexander M. Hill[1], Glenn A. Milne[1,2], Joseph Kuchar[2], Giorgio Ranalli[3]

(1) Department of Earth and Environmental Sciences, University of Ottawa, Ottawa, Canada

(2) Department of Physics, University of Ottawa, Ottawa, Canada

(3) Department of Earth Sciences, Carleton University, Ottawa, Canada

Tables

Table S1. RG observational RSL data aggregated by Mitrovica et al. (2000). Calibrated ages determined using the Reimer et al. (2013) marine calibration curve and the Calib 3.0 software (Stuiver & Reimer 1993).

Latitude	Longitude	C14 Age (kyr)	C14 Age Error (kyr)	Calibrated Age (kyr)	Calibrated Age Error (kyr)	Height (m)	Height Error (m)
56.28	-76.5	-6.43	0.15	-6.91	0.3435	172	2.5
56.45	-76.5	-6.23	0.22	-6.71	0.4845	154	2.5
56.28	-76.5	-6	0.16	-6.43	0.367	137	2.5
55.63	-77.13	-3.48	0.1	-3.35	0.254	52.3	2.5
55.58	-77.32	-3.36	0.06	-3.21	0.1615	58	2.5
55.63	-77.13	-2.86	0.1	-2.58	0.237	34.3	1.715
55.58	-77.3	-2.76	0.08	-2.51	0.194	44	2.2
55.63	-77.13	-2.51	0.08	-2.15	0.1915	32	1.6
55.36	-77.62	-2.47	0.1	-2.11	0.2335	31.7	1.585
55.36	-77.62	-2.43	0.1	-2.08	0.2355	28.9	1.445
55.63	-77.13	-2.41	0.09	-2.07	0.222	31.5	1.575
55.36	-77.62	-2.26	0.1	-1.86	0.2505	26.6	1.33
55.36	-77.62	-2.23	0.1	-1.83	0.2495	29.9	1.495
55.36	-77.62	-2.05	0.1	-1.62	0.236	21.9	1.095
55.58	-77.3	-2.03	0.06	-1.6	0.163	29	1.45
55.36	-77.62	-2.026	0.1	-1.59	0.235	27.3	1.365
55.36	-77.62	-2.02	0.1	-1.59	0.234	23.7	1.185
55.58	-77.3	-1.79	0.05	-1.36	0.1105	22	1.1
55.36	-77.62	-1.76	0.09	-1.33	0.192	20.4	1.02
55.36	-77.62	-1.68	0.09	-1.22	0.197	18.8	0.94
55.39	-77.5	-1.68	0.39	-1.31	0.7995	21.4	1.07
55.36	-77.62	-1.49	0.09	-1.06	0.1905	17.3	0.865
55.58	-77.3	-0.89	0.1	-0.48	0.1695	13.3	0.665
55.63	-77.13	-0.67	0.08	-0.3	0.1775	4.7	0.5

Table S2. Decay time results at ÅR for Earth viscosity models where the observational constraint is satisfied for all 3 considered ice histories. Upper and lower mantle viscosity are given in units of 10^{21} Pas, and decay times are stated in kyr. MRL viscosity is expressed as an o.o.m., with the exception of 'NA' which indicates that MRL viscosity is not applicable in cases where the MRL thickness is zero.

Earth Viscosity Model				ICE-5G		ANU		ICE-5G-FIS78311	
UMV	LMV	MRL Thickness (km)	MRL Viscosity	Model Decay Time	Observational Decay Time Range (2σ)	Model Decay Time	Observational Decay Time Range (2σ)	Model Decay Time	Observational Decay Time Range (2σ)
0.3	30	0	NA	4.53	3.66 - 4.72	3.98	3.87 - 4.54	5.21	4.04 - 5.34
0.3	30	1	E19	4.5	3.66 - 4.73	3.95	3.88 - 4.55	5.2	4.05 - 5.35
0.3	50	0	NA	4.58	3.67 - 4.73	4.02	3.88 - 4.54	5.29	4.05 - 5.34
0.3	50	1	E18	4.47	3.91 - 4.55	3.92	3.91 - 4.59	5.25	4.08 - 5.4
0.3	50	1	E19	4.55	3.67 - 4.74	3.99	3.88 - 4.55	5.28	4.05 - 5.35
0.7	1	0	NA	4.41	4.0 - 5.18	4.6	4.09 - 4.79	5.08	4.09 - 5.38
0.7	1	1	E19	4.27	3.99 - 5.17	4.46	4.09 - 4.79	4.9	4.1 - 5.4
0.9	1	1	E17	4.35	4.04 - 5.25	4.68	4.15 - 4.87	5.17	4.12 - 5.41
0.9	1	1	E18	4.49	4.04 - 5.25	4.8	4.13 - 4.85	5.3	4.11 - 5.4
0.9	1	10	E18	4.31	4.04 - 5.24	4.62	4.14 - 4.87	5.12	4.12 - 5.41
0.9	1	10	E19	4.45	4.04 - 5.24	4.76	4.13 - 4.85	5.25	4.11 - 5.4
0.9	1	20	E18	4.18	4.02 - 5.22	4.48	4.14 - 4.86	5.05	4.12 - 5.43
0.9	1	20	E19	4.32	4.03 - 5.24	4.63	4.13 - 4.86	5.1	4.12 - 5.41

Table S3. As Table S2 but for decay time results at RG.

Earth Viscosity Model				ICE-5G		ANU		ICE-5G-NAIS9927	
UMV	LMV	MRL Thickness (km)	MRL Viscosity	Model Decay Time	Observational Decay Time Range (2σ)	Model Decay Time	Observational Decay Time Range (2σ)	Model Decay Time	Observational Decay Time Range (2σ)
0.3	5	0	NA	4.67	3.0 - 5.11	4.61	3.41 - 6.51	4.45	3.76 - 7.72
0.3	5	1	E15	4.68	2.99 - 5.1	4.31	3.4 - 6.54	4.12	3.74 - 7.86
0.3	5	1	E16	4.65	3.02 - 5.16	4.48	3.43 - 6.6	4.24	3.78 - 7.95
0.3	5	1	E17	4.7	3.03 - 5.18	4.59	3.45 - 6.64	4.33	3.79 - 7.96
0.3	5	1	E18	4.63	3.01 - 5.14	4.56	3.43 - 6.58	4.34	3.77 - 7.83
0.3	5	1	E19	4.65	3.0 - 5.12	4.6	3.41 - 6.52	4.42	3.76 - 7.74
0.3	5	10	E17	4.56	3.02 - 5.16	4.4	3.43 - 6.61	4.13	3.77 - 7.98
0.3	5	10	E18	4.67	3.03 - 5.18	4.57	3.45 - 6.64	4.29	3.79 - 7.97
0.3	5	10	E19	4.6	3.01 - 5.14	4.54	3.43 - 6.58	4.3	3.77 - 7.84
0.3	5	20	E18	4.6	3.04 - 5.2	4.5	3.45 - 6.67	4.19	3.79 - 8.03
0.3	5	20	E19	4.58	3.02 - 5.16	4.51	3.44 - 6.62	4.24	3.78 - 7.91
0.3	10	10	E16	4.89	3.0 - 5.12	4.39	3.43 - 6.61	3.92	3.75 - 8.04
0.3	10	20	E17	4.92	3.02 - 5.15	4.57	3.44 - 6.61	4.05	3.77 - 8.05
0.5	5	10	E16	4.78	2.97 - 5.05	4.22	3.44 - 6.61	4.1	3.71 - 7.51
0.5	5	20	E17	4.82	2.98 - 5.08	4.41	3.45 - 6.61	4.25	3.73 - 7.55

Table S4. $\dot{J}_2$ results for Earth viscosity models where the observational constraint is satisfied for all 3 considered ice histories. Upper and lower mantle viscosity are given in units of 10^{21} Pas. MRL viscosity is expressed as an o.o.m., with the exception of 'NA' which indicates that MRL viscosity is not applicable in cases where the MRL thickness is zero. The observed $\dot{J}_2$ range is -5.4±0.7 (2σ). All $\dot{J}_2$ values stated here are in units of 10^{-11}/yr.

Earth Viscosity Model				ICE-5G	ANU	ICE-5G-NAIS9927
UMV	LMV	MRL Thickness (km)	MRL Viscosity	Model $\dot{J}_2$	Model $\dot{J}_2$	Model $\dot{J}_2$
0.1	10	10	E15	-5.19	-5.69	-4.81
0.1	10	20	E16	-5.04	-5.63	-4.73
0.3	10	1	E19	-5.11	-6.09	-5
0.5	10	1	E18	-5.09	-6.08	-5
0.5	10	10	E19	-5.11	-6.1	-5.01
0.5	10	20	E15	-5.48	-6.07	-5.12
0.5	10	20	E19	-4.83	-5.77	-4.74
0.7	10	20	E15	-5.44	-6.06	-5.09
0.7	10	20	E19	-4.98	-5.99	-4.89
0.9	10	20	E15	-5.43	-6.07	-5.1
0.3	30	1	E15	-5.59	-5.93	-5.25
0.3	30	1	E16	-5.33	-5.86	-5.11
0.3	30	1	E17	-5.49	-5.95	-5.22
0.3	30	10	E16	-5.71	-5.96	-5.29
0.3	30	10	E17	-5.43	-5.88	-5.14
0.3	30	10	E18	-5.43	-5.97	-5.23
0.3	30	20	E17	-5.48	-5.91	-5.17
0.3	30	20	E18	-5.48	-5.92	-5.2
0.5	30	1	E15	-5.58	-5.9	-5.18
0.5	30	1	E16	-5.32	-5.85	-5.05
0.5	30	1	E17	-5.49	-6.05	-5.24
0.5	30	10	E16	-5.62	-5.91	-5.14
0.5	30	10	E17	-5.34	-5.87	-5.06
0.5	30	10	E18	-5.5	-6.06	-5.25
0.5	30	20	E17	-5.38	-5.87	-5.02
0.5	30	20	E18	-5.42	-5.95	-5.16
0.7	30	1	E15	-5.6	-5.94	-5.21
0.7	30	1	E16	-5.34	-5.91	-5.09
0.7	30	10	E16	-5.64	-5.98	-5.24
0.7	30	10	E17	-5.36	-5.93	-5.1
0.7	30	20	E17	-5.39	-5.95	-5.12
0.7	30	20	E18	-5.47	-6.04	-5.23
0.9	30	1	E15	-5.68	-6.06	-5.3

0.9	30	1	E16	-5.43	-6.03	-5.18
0.9	30	10	E17	-5.43	-6.04	-5.19
0.9	30	20	E17	-5.46	-6.06	-5.21
0.1	50	0	NA	-5.75	-5.98	-5.42
0.1	50	1	E15	-5.66	-5.7	-5.18
0.1	50	1	E16	-5.43	-5.64	-5.07
0.1	50	1	E17	-5.5	-5.65	-5.15
0.1	50	1	E18	-5.66	-5.87	-5.33
0.1	50	1	E19	-5.74	-5.96	-5.41
0.1	50	10	E16	-5.72	-5.76	-5.25
0.1	50	10	E17	-5.45	-5.65	-5.09
0.1	50	10	E18	-5.51	-5.66	-5.16
0.1	50	10	E19	-5.67	-5.88	-5.34
0.1	50	20	E17	-5.5	-5.71	-5.14
0.1	50	20	E18	-5.51	-5.66	-5.15
0.1	50	20	E19	-5.63	-5.82	-5.29
0.3	50	1	E18	-5.7	-6.04	-5.41
0.3	50	10	E15	-5.79	-5.59	-5.22
0.3	50	10	E19	-5.71	-6.05	-5.42
0.3	50	20	E16	-5.56	-5.46	-5.06
0.3	50	20	E19	-5.41	-5.72	-5.13
0.5	50	10	E15	-5.7	-5.49	-5.14
0.5	50	20	E16	-5.39	-5.35	-4.9
0.5	50	20	E19	-5.6	-5.98	-5.32
0.7	50	10	E15	-5.72	-5.55	-5.11
0.7	50	20	E16	-5.48	-5.4	-5.01
0.9	50	1	E17	-4.99	-5.3	-4.74
0.9	50	10	E15	-5.82	-5.69	-5.29
0.9	50	10	E18	-4.99	-5.3	-4.74
0.9	50	20	E16	-5.57	-5.54	-5.11

Figures

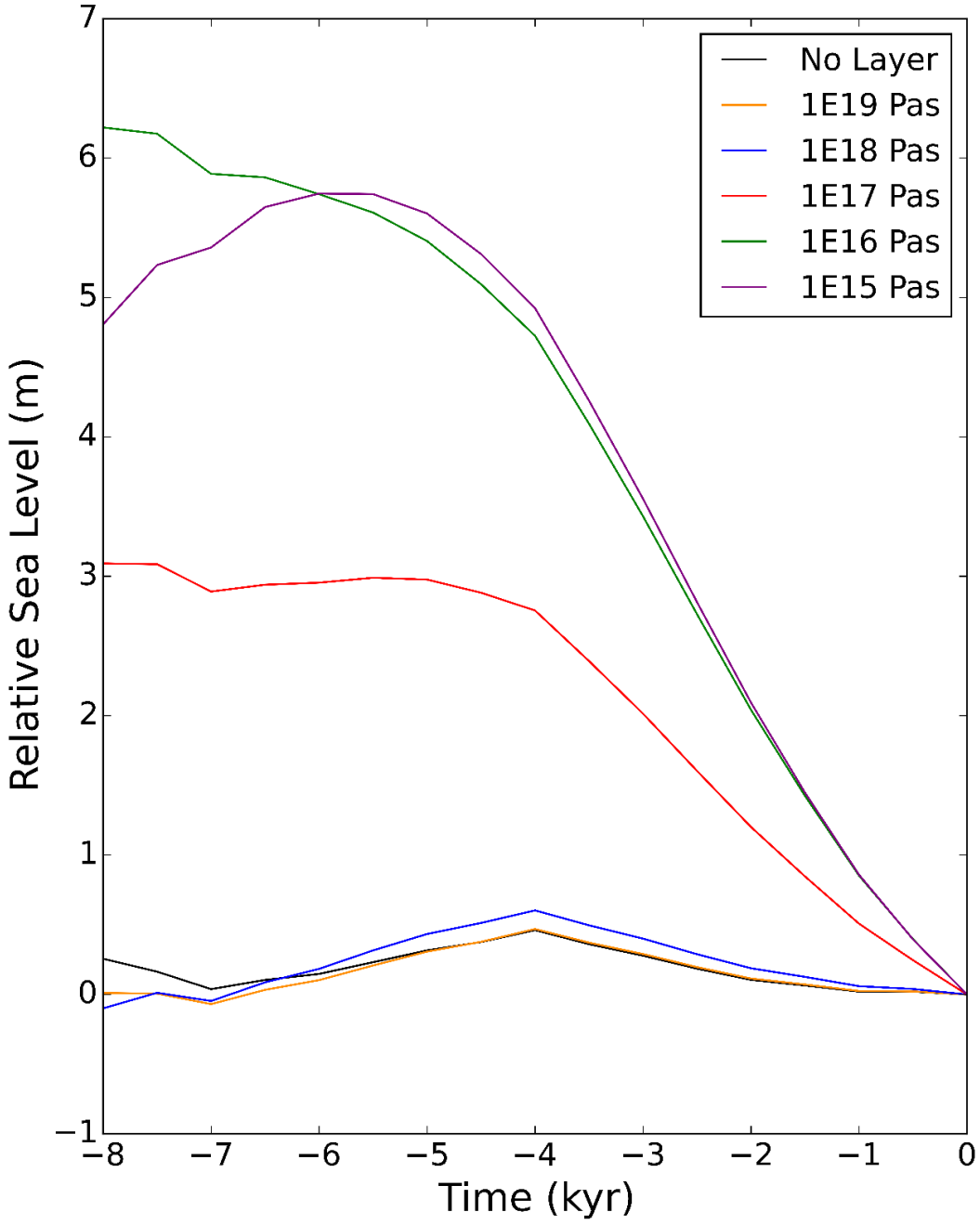

Figure S1. Examples of non-exponential modelled ice-related RSL curves determined using the ICE-5G-FIS78311 ice history model at ÅR for a 10^{20} Pas upper mantle viscosity, 10^{21} Pas lower mantle viscosity, and a 10 km thick hydrous MRL. MRL viscosities are indicated in the key.

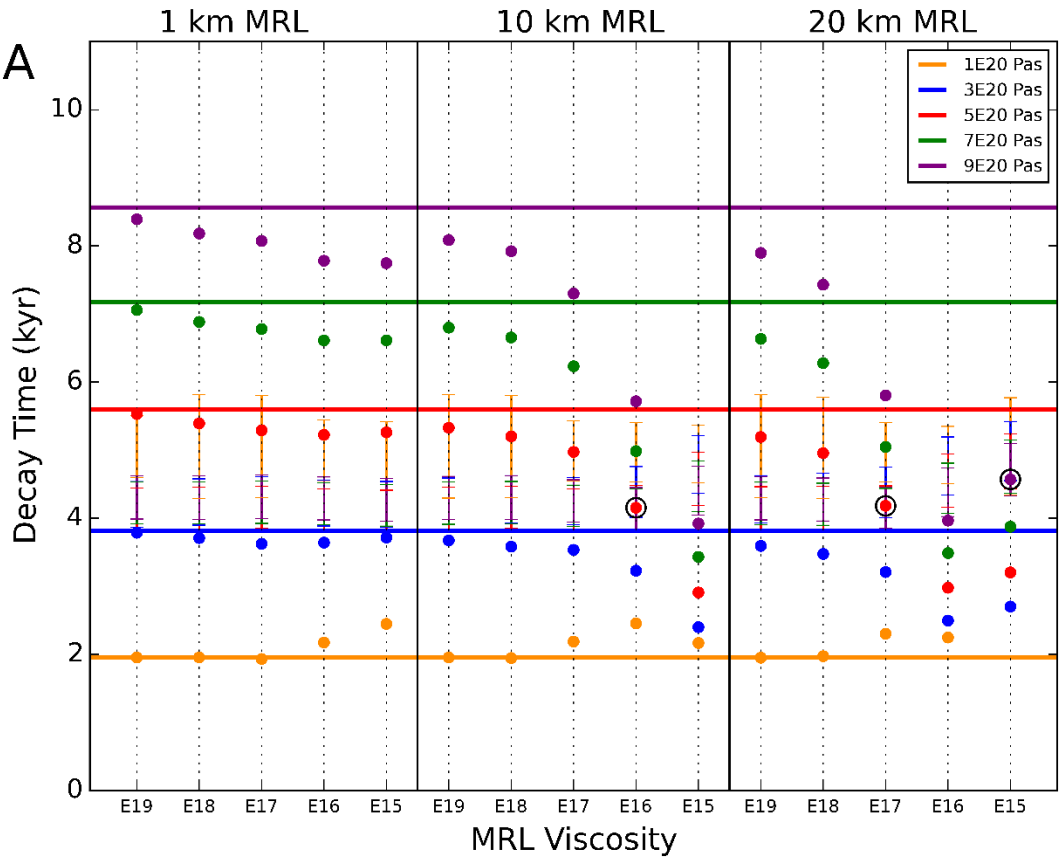

Figure S2. (A) Decay time results at ÅR for a fixed lower mantle viscosity of 10^{22} Pas determined using the ANU ice history model. The dots indicate the decay time values (vertical axis) for a given background viscosity (colour as indicated in key) and thickness and viscosity of a MRL (horizontal axis) just above 410 km depth. The coloured horizontal lines show the decay times for the upper mantle viscosity values indicated in the key when no low viscosity layer is included. Model-specific observational decay time ranges (±2σ) are illustrated by error-bars. Decay times which satisfy observational constraints are indicated by black outlines. Decay times considered unacceptable due to non-exponential RSL curve behaviour are marked with a black x. (B) As in (A) but for the case of a fixed upper mantle viscosity of 5×10^{20} Pas and different values of lower mantle viscosity (indicated in key).

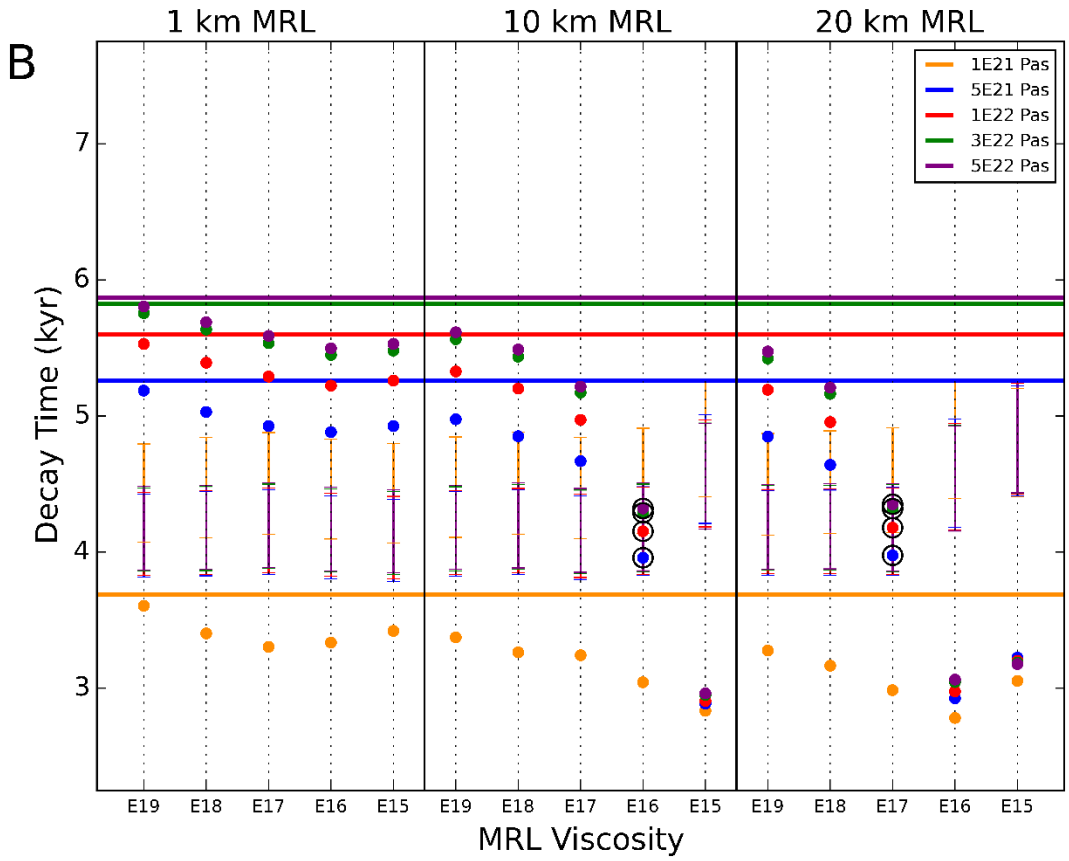

Figure S2 (continued).

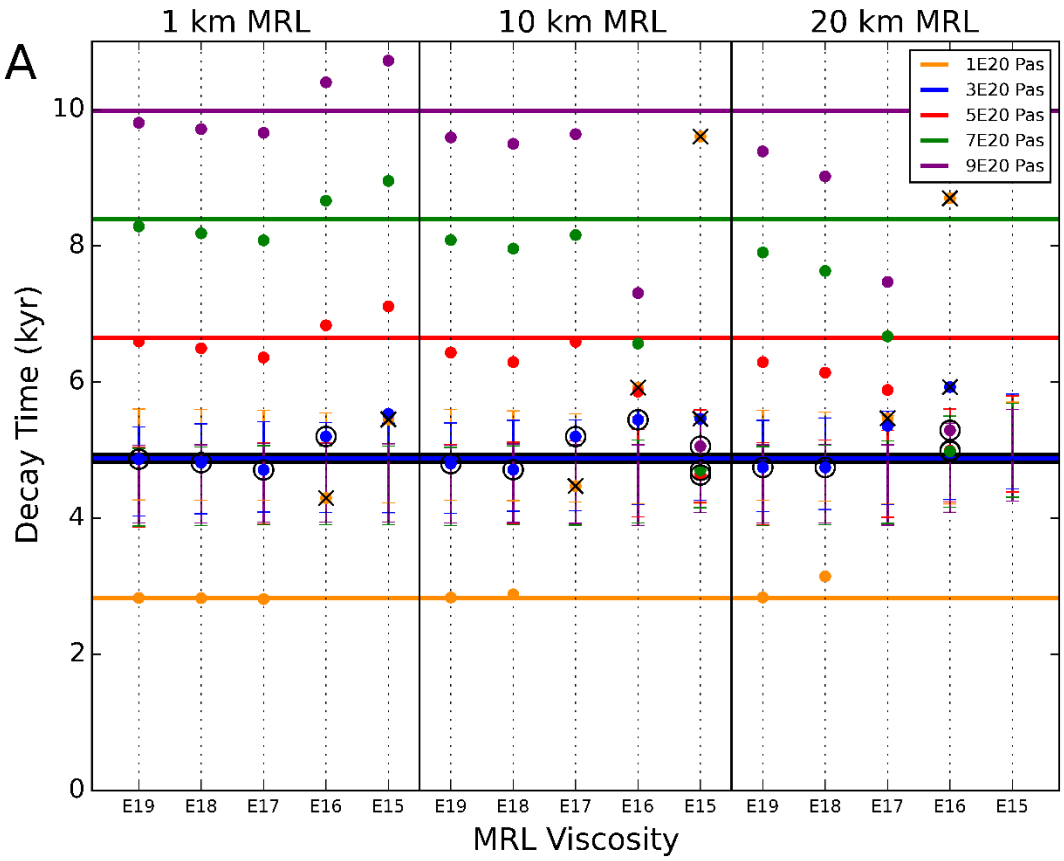

Figure 3. As Fig. S2 except for decay times determined using the ICE-5G-FIS78311 ice history model.

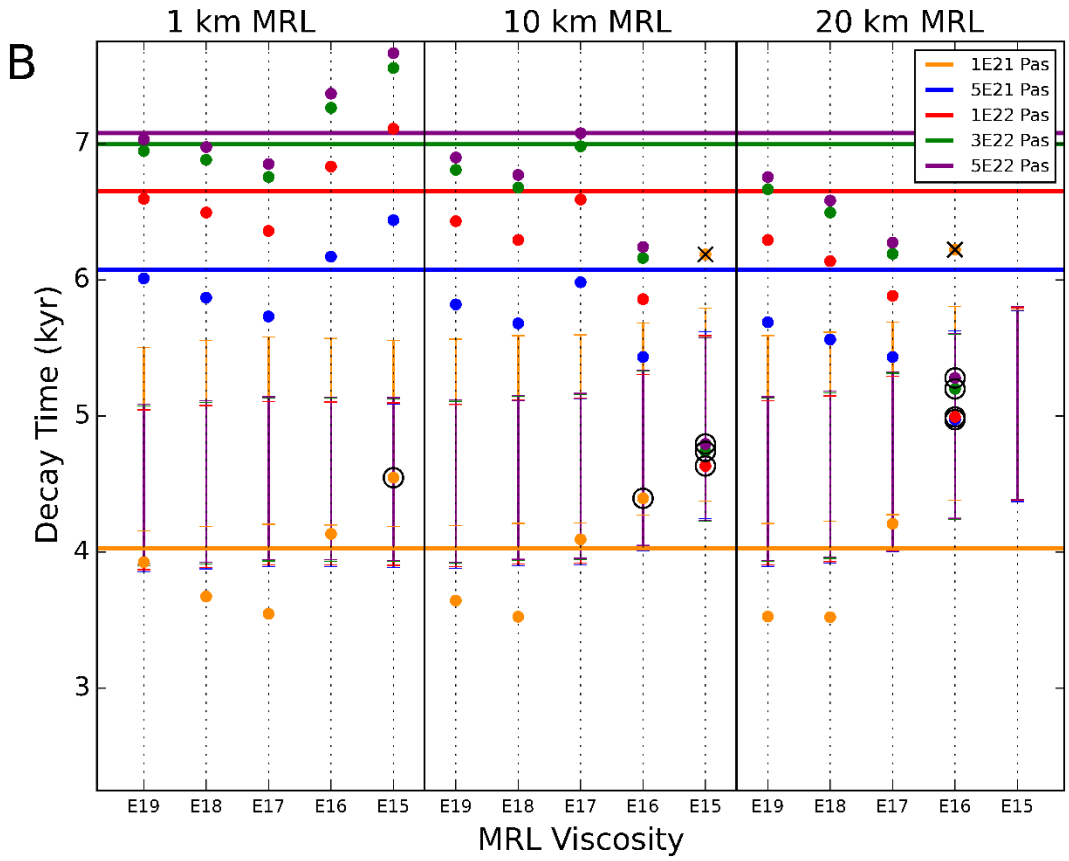

Figure S3 (continued).

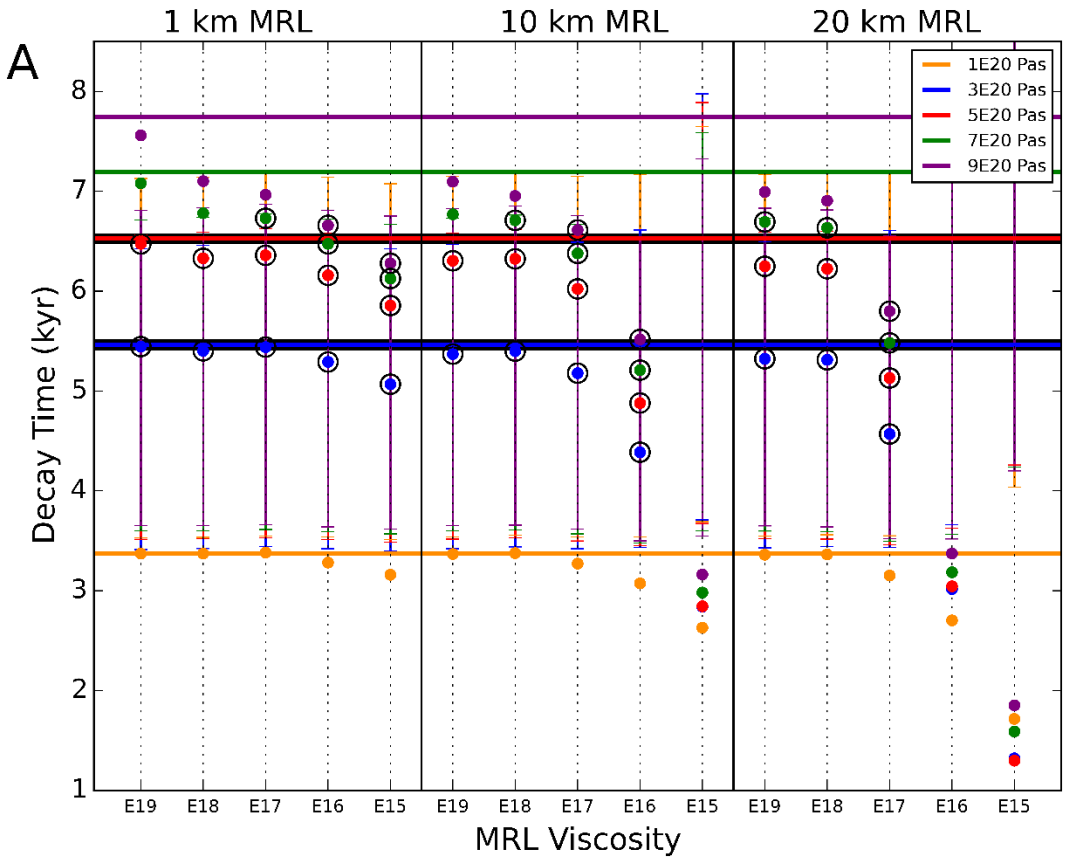

Figure S4. (A) Decay time results at RG for a fixed lower mantle viscosity of 10^{22} Pas determined using the ANU ice history model. The dots indicate the decay time values (vertical axis) for a given background viscosity (colour as indicated in key) and thickness and viscosity of a MRL (horizontal axis) just above 410 km depth. The coloured horizontal lines show the decay times for the upper mantle viscosity values indicated in the key when no low viscosity layer is included. Model-specific observational decay time ranges (±2σ) are illustrated by error-bars. Decay times which satisfy observational constraints are indicated by black outlines. Decay times considered unacceptable due to non-exponential RSL curve behaviour are marked with a black x. (B) As in (A) but for the case of a fixed upper mantle viscosity of 5×10^{20} Pas and different values of lower mantle viscosity (indicated in key).

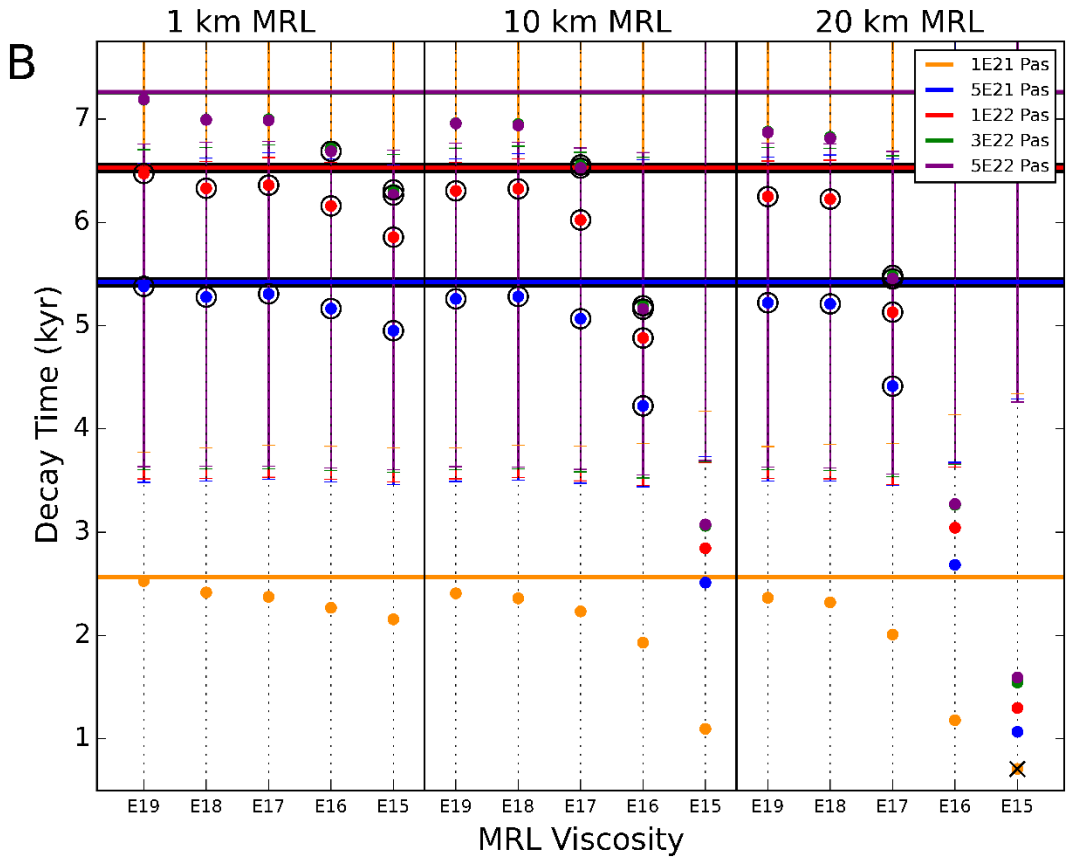

Figure S4 (continued).

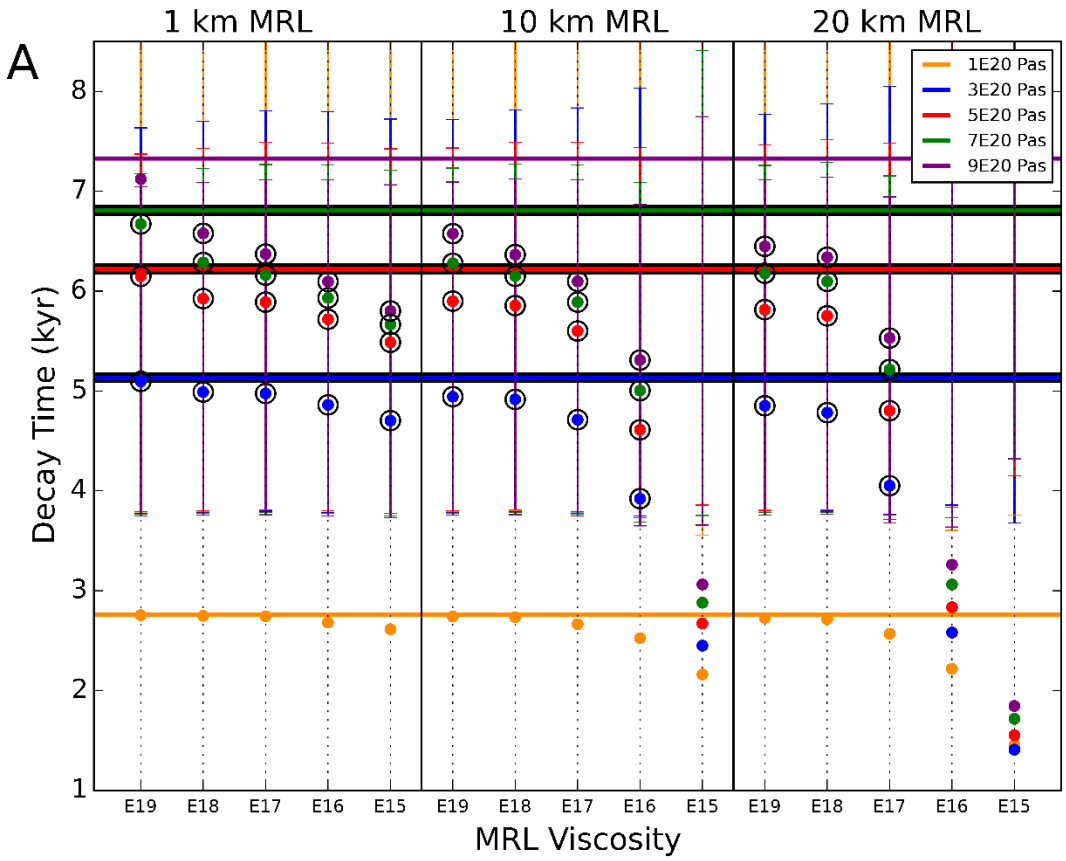

Figure S5. As Fig. S4 except for decay times determined using the ICE-5G-NAIS9927 ice history model.

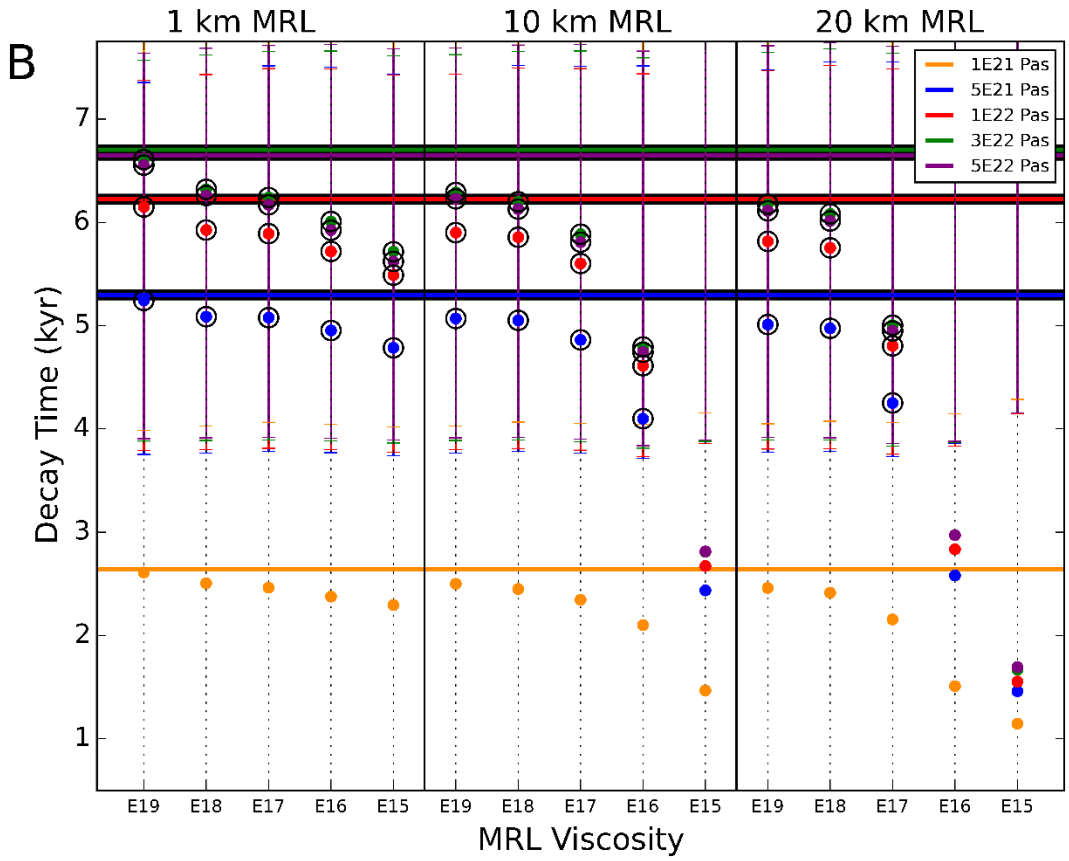

Figure S5 (continued).

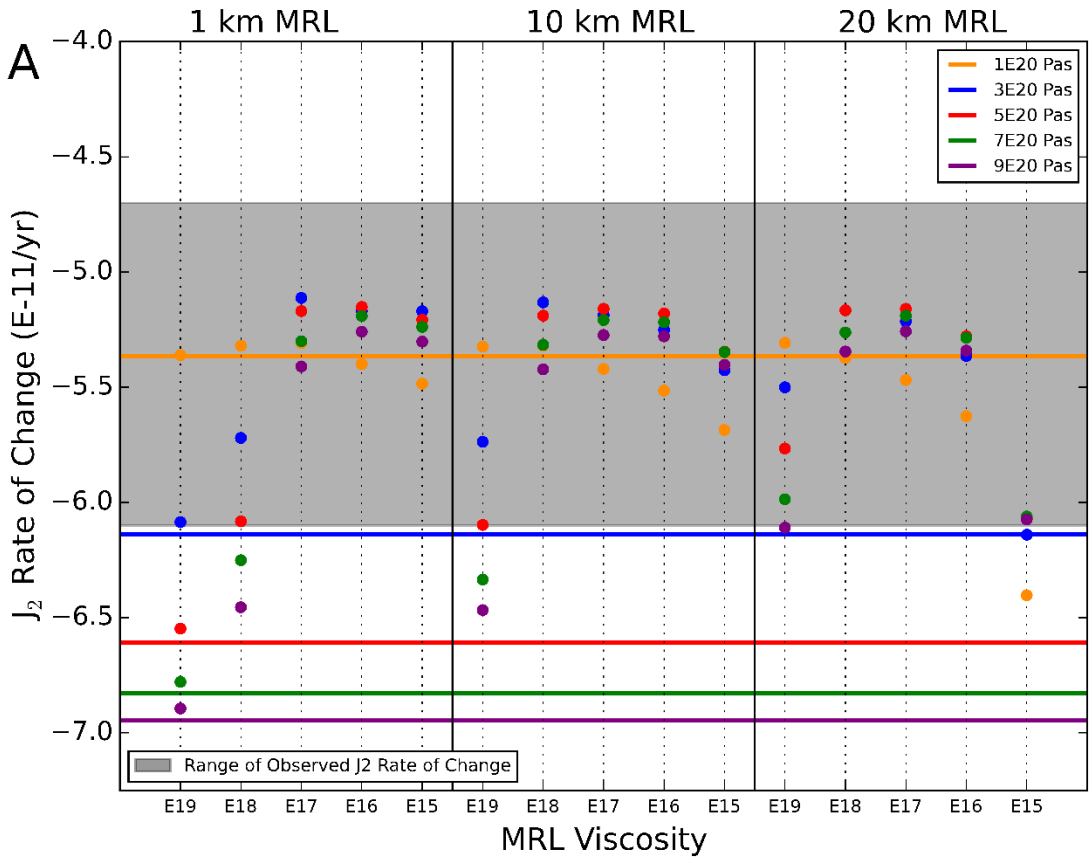

Figure S6. Predictions of $\dot{J}_2$ for a suite of Earth models with a lower mantle viscosity of 10^{22} Pas determined using the ANU ice history model. The dots indicate the $\dot{J}_2$ values (vertical axis) for a given background viscosity (colour as indicated in key) and thickness and viscosity of a MRL (horizontal axis) just above 410 km depth. The coloured horizontal lines show $\dot{J}_2$ values for the upper mantle viscosity values indicated in the key when no low viscosity layer is included. (B) As in (A) but for the case of a fixed upper mantle viscosity of 5×10^{20} Pas and different values of lower mantle viscosity (indicated in key). The grey region defines the observed constraint on $\dot{J}_2$ as relating to GIA (see main text for further information).

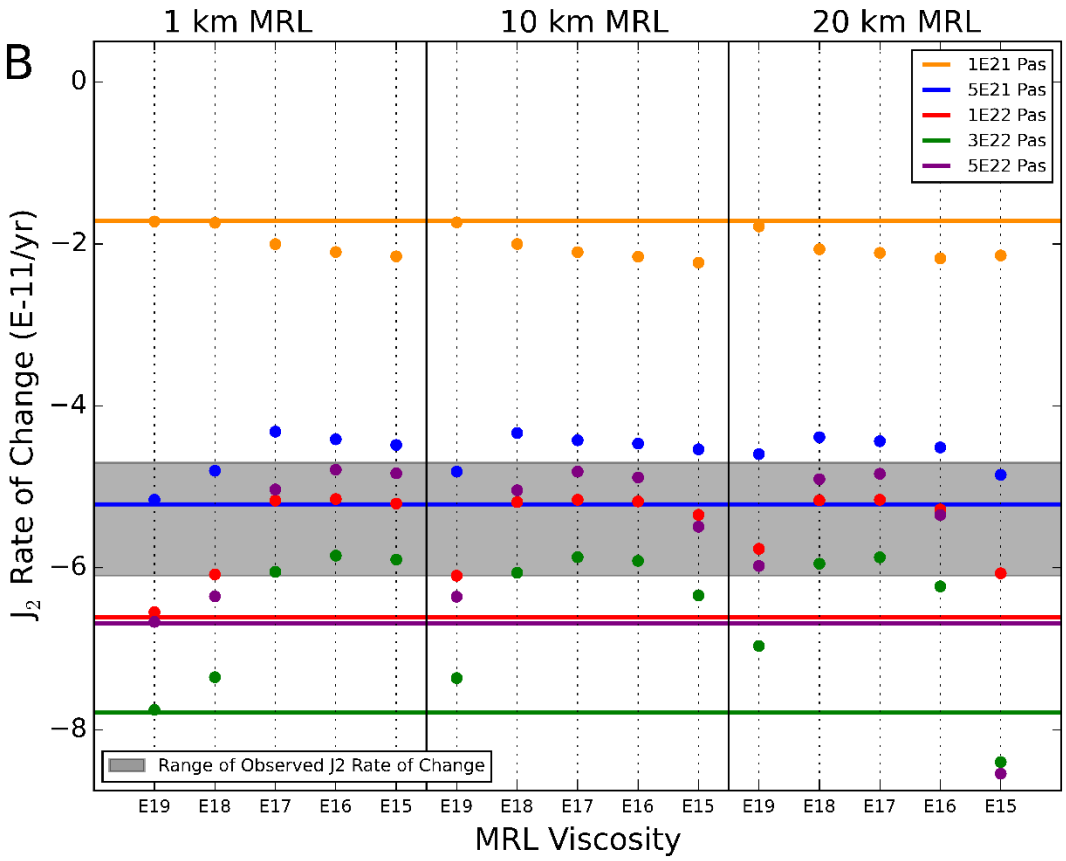

Figure S6 (continued).

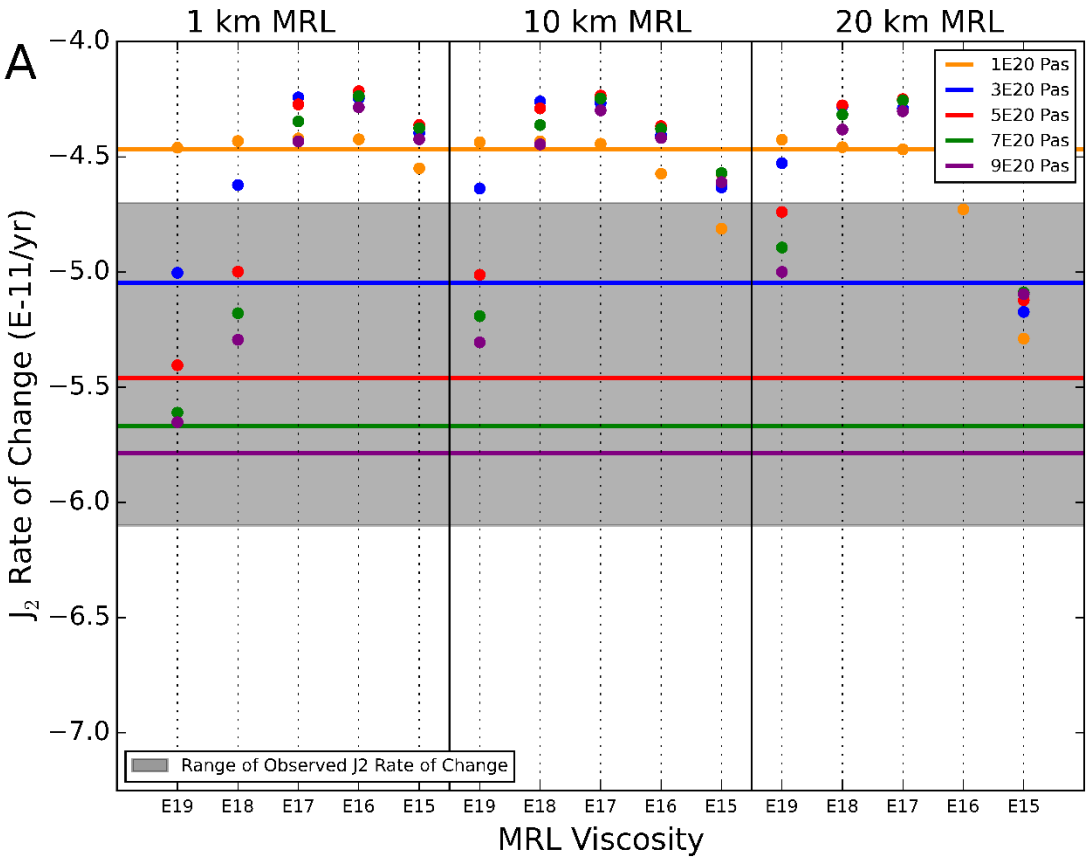

Figure S7. As Fig. S6 except for predictions of $\dot{J}_2$ determined using the ICE-5G-NAIS9927 ice history model.

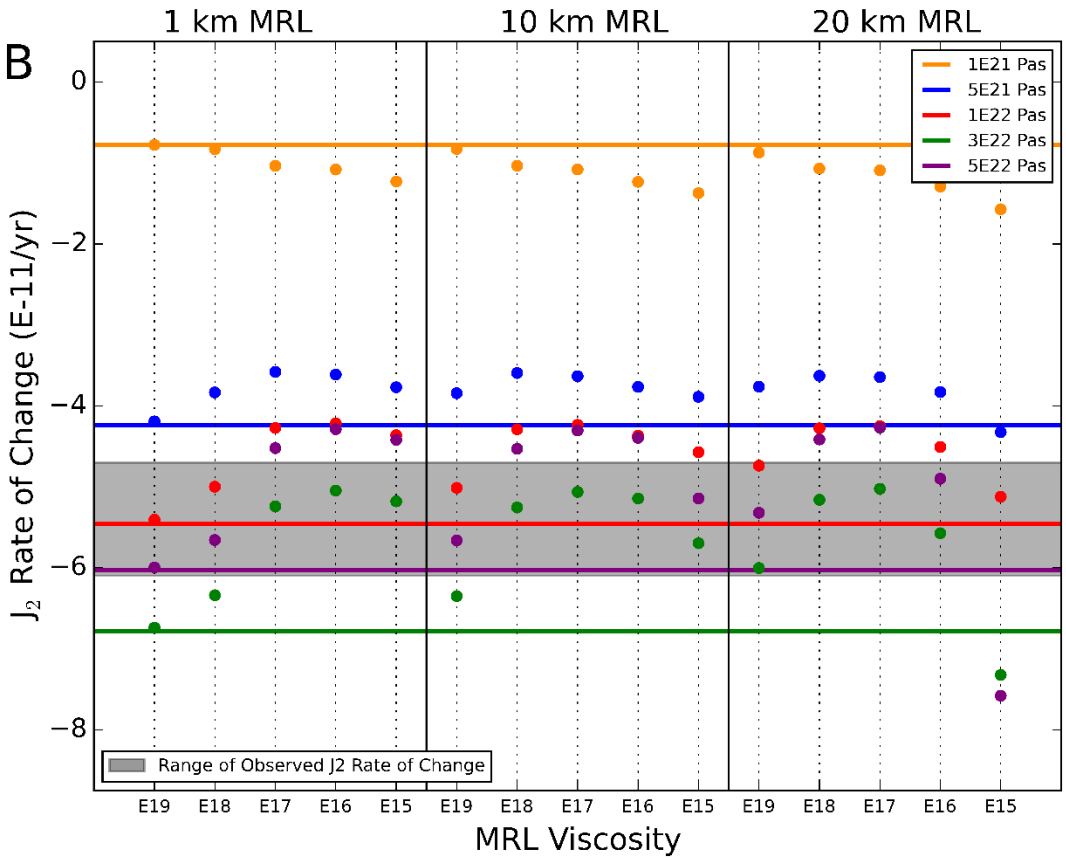

Figure S7 (continued).

Chapter 3

Constraining Lithosphere and Mantle Viscosity Structure Using Lower Mississippi River Long Profile Displacement

3.1 Introduction

Subsidence along the northern coast of the Gulf of Mexico is an ongoing problem which has major economic (Needham et al., 2012; Barnes et al., 2017) and sociological impacts (Glavovic, 2014). The societal cost of relative sea level rise in the Gulf Coast region has been significant historically (Salinas et al., 1986; Day & Templet, 1989; Penland & Ramsey, 1990; Morton et al., 2005), has accelerated in recent years (Dixon et al., 2006; Petterson et al., 2006), and is expected to intensify in the near future (Donoghue, 2011; Thatcher et al., 2013). Understanding the nature of subsidence in the Gulf Coast, and the factors that govern this process, is important for informed decision making related to mitigating these societal costs (Yuill et al., 2009; Dokka, 2011).

Subsidence in the Gulf Coast region is strongly influenced by the Mississippi River. This prominent hydrological feature extends through the central United States and terminates in the Gulf of Mexico in the form of a prograding delta. The Lower Mississippi River, which spans from south Illinois to the Gulf Coast, overlies a structural trough known as the Mississippi Embayment which is oriented southwest-northeast. The Mississippi Embayment developed during the Late Mesozoic and was subsequently infilled by fluvio-deltaic sediments, causing the shoreline to advance southwards (Cushing et al., 1964; Cox & Van Arsdale, 2002). Throughout the Cenozoic, the ancestral Mississippi River System advanced towards and into the modern-day Gulf of Mexico due to deltaic sediment deposition (Galloway et al., 2000, 2011; Craddock & Kylander-Clark, 2013). During the Quaternary, Mississippi River sediment has been deposited predominantly in south Louisiana and the northern Gulf of Mexico (Blum & Roberts, 2012). Since the inception of the Mississippi Embayment, the solid Earth underlying the modern-day Mississippi River has been subjected to stresses relating to isostatic compensation of sediment

loading and, more recently, Quaternary glaciation. In addition to its viscous effects, sediment loading has also affected brittle deformation in the region. The deposition of the sediment mass through time has driven tensional forces acting perpendicular to the coast, which consequently created synsedimentary normal faults oriented parallel to the coast (Nunn, 1985). This style of faulting, typically referred to as growth faulting, is a common feature of passive continental margins subjected to high sedimentation rates (Mauduit & Brun, 1998; Childs et al., 2003). In south Louisiana, where the Mississippi Delta system meets the northern Gulf of Mexico, a dense network of growth faults has formed due to the regional stress regime (Figure 3.1).

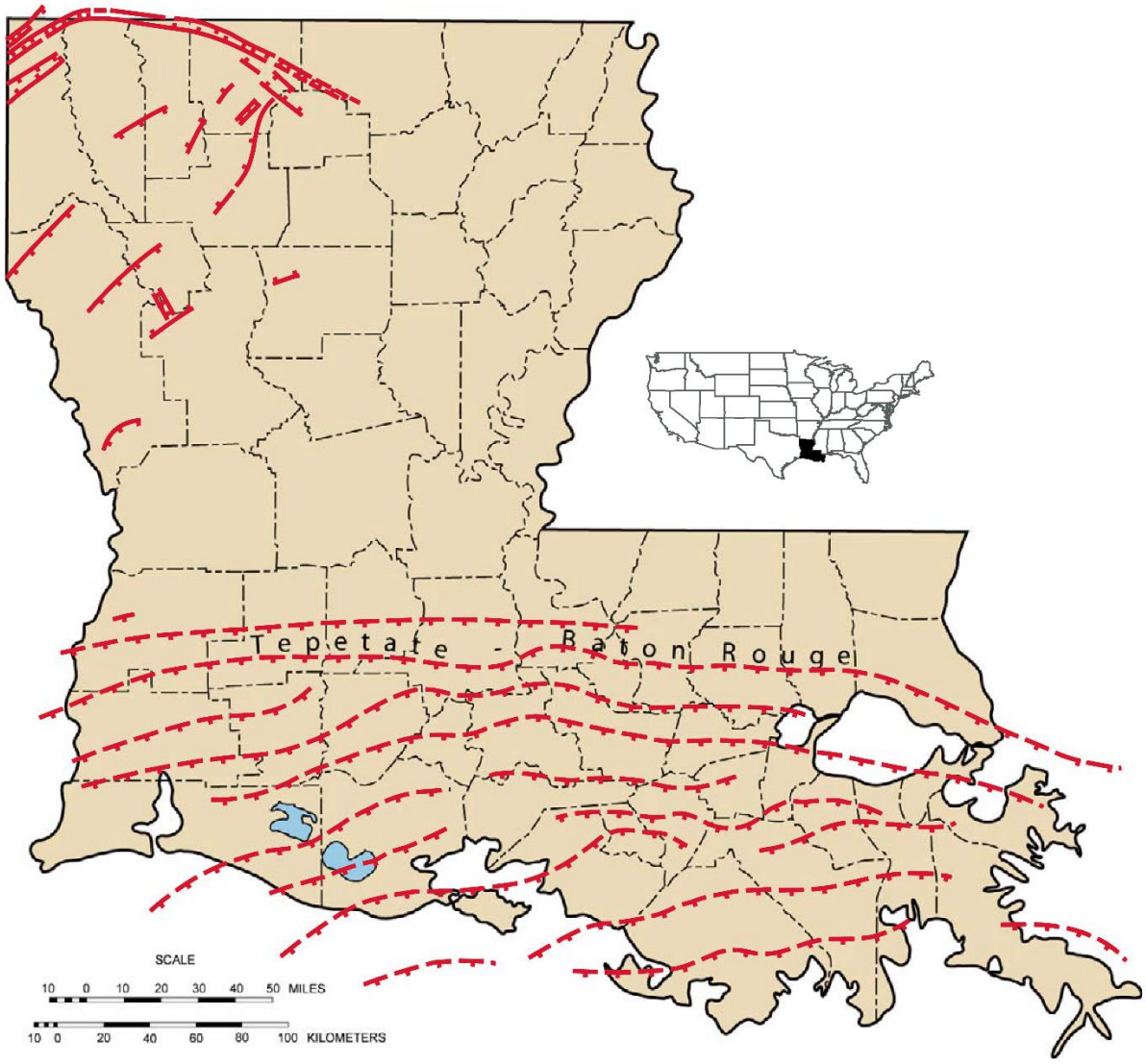

Figure 3.1. Surface expressions of fault systems (indicated in red) in the Mississippi Delta region of Louisiana (McCulloh & Heinrich, 2012).

This study seeks to examine the solid-Earth deformation associated with these surface loading changes by analyzing how the long profile (henceforth LP) of the river has changed over time. By modelling solid-Earth deformation in the south-central United States, constraints on Earth viscosity structure can be determined by comparing model output with observed LP displacement. There is evidence to suggest that a component of observed downward LP motion was accommodated by displacement within the fault systems of the Mississippi Delta region (Gagliano et al., 2003; McCulloh & Heinrich, 2012; Shen et al., 2017; Frederick et al., 2018), so two end-member faulting scenarios are accounted for during the modelling procedure applied here. Due to the localized spatial extent of sediment deposition, the mechanical structure of the lithosphere is expected to be a significant factor in the sediment isostatic adjustment process. For this reason, the data constraining changes in the LP through time are particularly well-suited for evaluating lithosphere structure in the region. In this study, two approaches to modelling the lithosphere are used: a traditional approach in which the lithosphere is modelled as an elastic layer and defined by its thickness, and a more complex approach where depth-dependent viscous structure is included as well as the Moho (Kuchar & Milne, 2015). Using the latter approach provides indirect information on subsurface thermal conditions due to the dependence of the viscosity structure on temperature (see Section 3.2.2.1). Using these modelling approaches, valuable insight can be gained into the thermal and mechanical structure of the Earth in this region as well as the relative contributions of isostatic deformation and fault displacement to the magnitude and geographic distribution of regional land subsidence.

This study builds on past work (Wolstencroft et al., 2014) in which a sensitivity analysis was performed to examine which components of the sediment load (delta, fan, paleovalley, shelf, canyon) dominate the LP displacement and which Earth model components (lithosphere thickness, upper mantle viscosity, lower mantle viscosity) have the largest impact on the modelled signal when varied. It was found that the shelf load dominates the curvature of the LP displacement, particularly at the southern end of the profile, while the ice load has a large effect on the absolute height and general north-south trend of the LP displacement (see Figure 9 of Wolstencroft et al., 2014). The research presented here improves upon this past work in several respects: (i) ocean loading is modelled in a gravitationally self-consistent manner (Dalca et al., 2013; see Section 3.2.2); (ii) our Earth model parameter set is much larger (300 compared to 8), allowing model parameters to be inferred with greater precision; (iii) lithosphere models with

viscous structure are considered (in addition to the more conventional elastic models); (iv) the influence of faulting is taken into account in the parameter inference procedure; (v) only relative height changes of the LP are modelled to remove sensitivity to the poorly known ice loading history and enhance sensitivity to the signal associated with the sediment load – this acts to better target Earth viscosity structure beneath the southern portion of the LP (details provided in Section 3.2.3).

Past studies (e.g. Love et al., 2016; Kuchar et al., 2018) have used relative sea level observations from the Gulf Coast region to infer Earth viscosity structure. However, such sea level data is sensitive to the signal associated with North American deglaciation and so the inferred viscosity values relate to the broad region separating the major glaciation centres (Canada) and the Gulf Coast. Specifically, the deformation signal captured by the sea level data is largely that associated with the evolution of the peripheral bulge of the Laurentide ice sheet (e.g. Kuchar et al., 2019). In contrast, the observations that constrain LP displacement, when considered in terms of profile shape (i.e. changes in relative height rather than total height), are dominated by sediment and ocean loading in the Gulf Coast region (Section 3.3.1; Wolstencroft et al., 2014) and so modelling these data more effectively targets Earth structure in this region.

3.2 Methods

3.2.1 Observational Data

The observed LP displacement is determined based on data from collected drill cores of Mississippi River sediments (Figure 3.2). The LP corresponding to Marine Isotope Stage 5a is identified in the sediment record using stratigraphic correlation as well as optically stimulated luminescence dating of quartz (Shen & Lang, 2016). It is assumed that the LP at 80 ka had a shape that is the same as that of the present-day Mississippi River so that the difference in height between the two profiles can be used as a measure of vertical land motion over the past 80 kyr. To account for the effect of fault displacement, two scenarios are considered: one assumes that 13% of total LP displacement between latitudes 29.6°N and 30.3°N can be attributed to fault displacement, whereas the other assumes a more extreme case of 40% fault displacement. For both of these end-member scenarios, the vertical displacement related to faulting is removed

from the observations in order to isolate the isostatic signal before comparing to model output (Figure 3.3). This fault correction scales with the magnitude of total displacement, such that more fault displacement is assumed further south along the long profile (compare total displacement with the adjusted displacements in Figure 3.3). As more of the total observed displacement is attributed to fault slippage, less isostasy-related surface displacement is needed to meet the observational constraints.

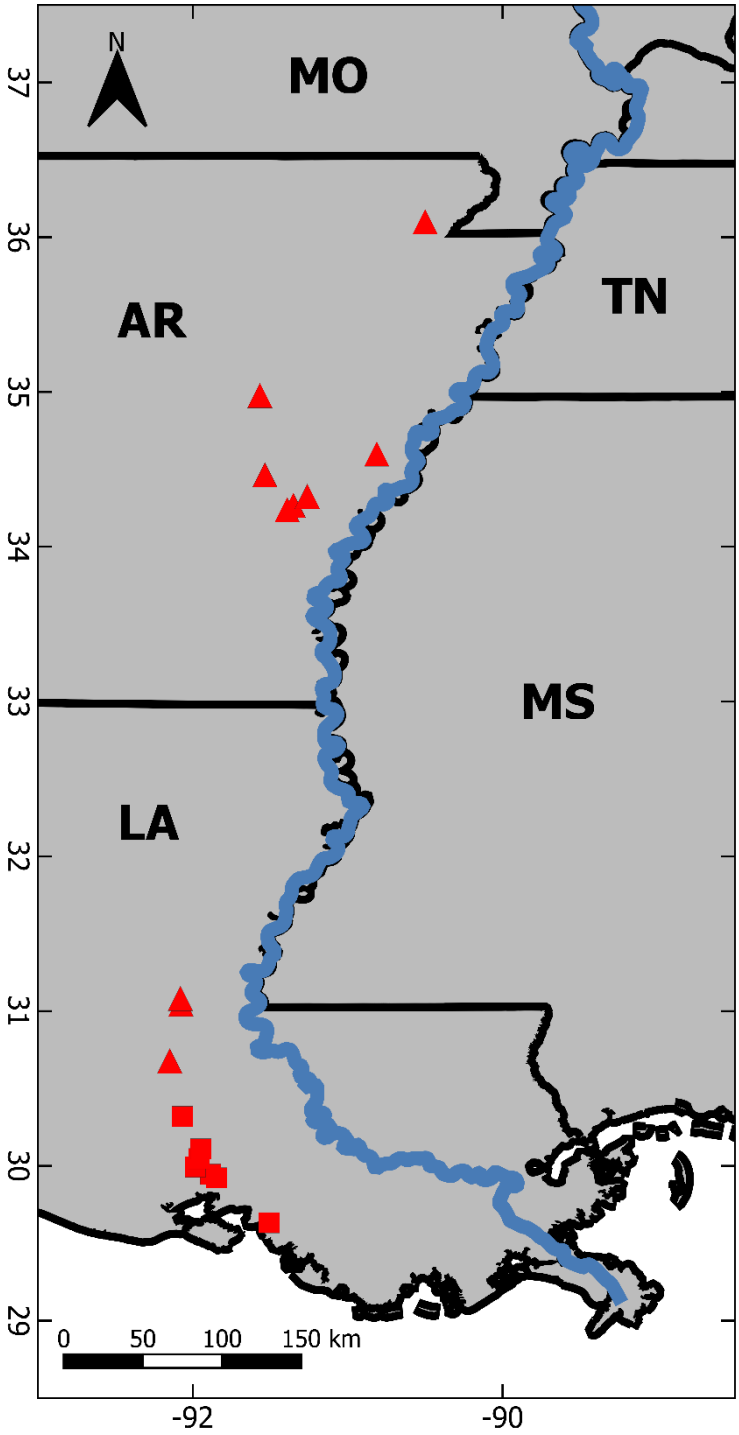

Figure 3.2. Geographic positions of observational data collection sites (in red). Observational data locations where the fault correction is applied are plotted as squares, and the remaining uncorrected data locations are plotted as triangles. The Mississippi River is plotted in blue and state boundaries in black. Abbreviated state names are labelled on the map. Latitude and longitude are indicated on the axes.

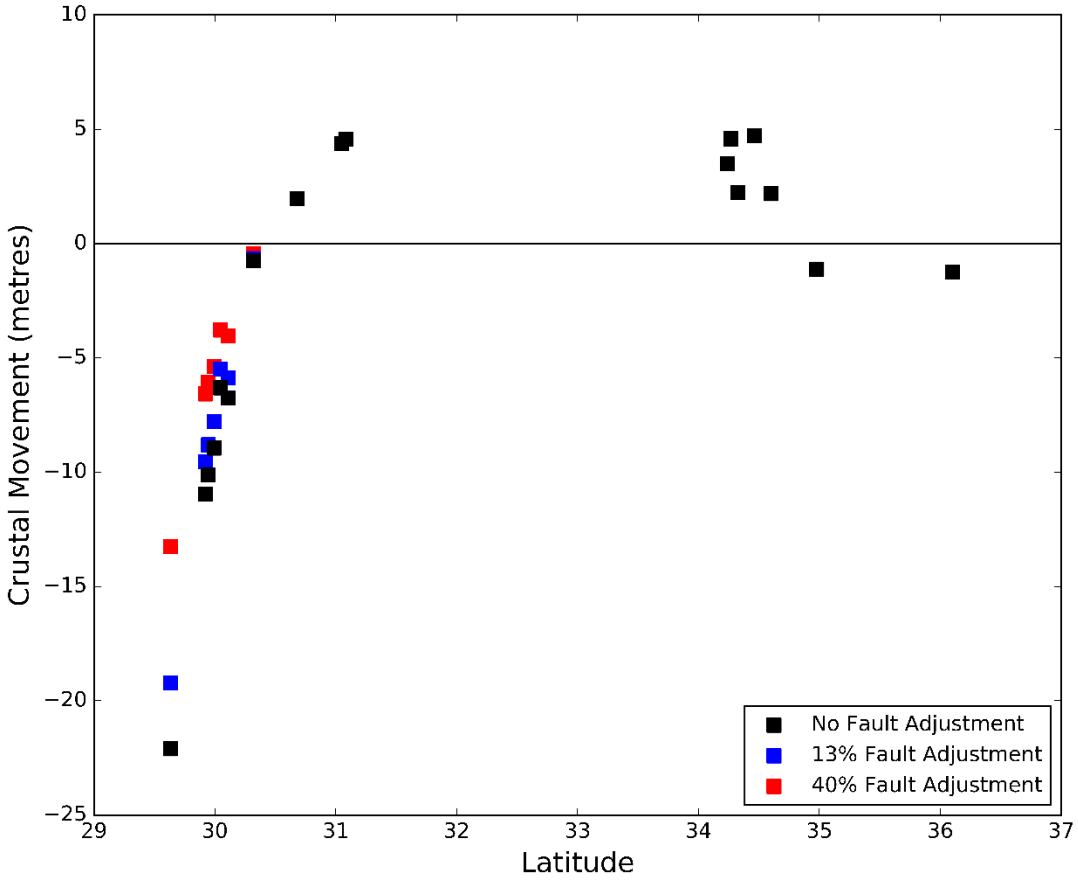

Figure 3.3. Observational LP displacement data with different fault-correction scenarios indicated in key.

3.2.2 Model

The model Earth is a spherically symmetric planet with a Maxwell viscoelastic rheology. Its response to surface loading is computed using the approach of Peltier (1974). The loading history is modelled from 122 ka to present. For ice-load modelling, the global ICE-5G model (Peltier, 2004) is employed but with the North American component replaced by a model (calibration 1243) provided by Tarasov et al. (2012). To model sediment isostatic adjustment, reconstructions of Mississippi Delta sediment deposition outlined in Wolstencroft et al. (2014, and references therein) are used. We compute the ocean load using the theory described in Dalca

et al. (2013), and so the displacement of water resulting from sediment deposition is accurately accounted for. This treatment of ocean loading is more realistic than the approach previously used by Wolstencroft et al. (2014), who simply altered the sediment densities to account for ocean water being displaced by sediment. A spherical harmonic truncation of 512 is used for all modelling, as this has been demonstrated to provide a resolution sufficient to model sediment isostatic adjustment in the Mississippi Delta region of the Gulf Coast (Wolstencroft et al., 2014).

To evaluate the sensitivity of LP displacement to Earth viscosity structure, the properties of both the lithosphere and mantle are varied. The sub-lithospheric mantle is separated into two (upper and lower) zones by a boundary at 670 km depth. Above this boundary, upper mantle viscosity (henceforth UMV) values of 0.08, 0.1, 0.3, 0.5 and 1×10^{21} Pas are considered. Below this boundary, lower mantle viscosity (henceforth LMV) values of 1, 2, 3, 5, 10, 20, 30, 50, 70 and 90×10^{21} Pas are considered. The density and elastic properties of the Earth models are equivalent to those of the Preliminary Reference Earth Model (Dziewonski & Anderson, 1981), except in the case of the modelled viscous lithospheres (see below for more information). For modelling of the lithosphere component of Earth structure, two general rheological scenarios are evaluated. In the simpler scenario, the lithosphere is assumed to have a very high (10^{42} Pas) and constant viscosity such that it behaves entirely elastic over the timescales considered here. For these 'elastic' lithosphere models, four distinct lithosphere thicknesses of 46, 71, 96, and 120 km are considered. The lithosphere models with more realistic viscous structure are determined using the method described in the following subsection.

3.2.2.1 Lithosphere Models with Viscous Structure

To determine lithosphere viscosity structure, the theory presented in Kuchar & Milne (2015, and references therein) is applied. Viscosity is a temperature-dependent property, so a geothermal profile must first be determined. This is done using the following analytical solution for lithosphere temperature (e.g. Turcotte & Schubert, 2014):

$$T(Z) = \frac{A_0 h^2}{K}\left(1 - e^{-Z/h}\right) + \left(T_0' - \frac{A_0 h}{K}\right)Z + T_0 \qquad (1)$$

where T is temperature (T_0 is surface temperature), Z is depth, A_0 is surface radiogenic heat production (set to 2592 W/km^3), h is a scaling parameter (set to 13 km) and K is thermal conductivity (set to 3 W/mK). Using this temperature profile, lithosphere viscosity at a given depth is computed by applying the following relationship (e.g. Turcotte & Schubert, 2014):

$$\eta = \frac{1}{2}\left(\frac{\dot{\varepsilon}^{1-n}}{A_D}\right)^{1/n} \exp\left(\frac{E_D}{nRT}\right) \quad (2)$$

where η is effective viscosity, R is the gas constant, T is temperature and $\dot{\varepsilon}$ is strain rate (set to 10^{-15} s^{-1}). n and A_D are empirically determined material-specific constants, and E_D is activation enthalpy. For crustal material, n, A_D and E_D are 2.72, 6.03×10^{-24} Pa^{-n}s^{-1}, and 1.34×10^5 Jmol^{-1}, respectively. For the lithospheric mantle, n, A_D and E_D are 4.2, 8.83×10^{-22} Pa^{-n}s^{-1}, and 4.45×10^5 Jmol^{-1}, respectively. For viscosity structure determination, a depth resolution of 1 km is used.

The lithosphere temperature profile computation requires a near-surface temperature gradient (T_0' in equation (1)) as a boundary condition. This information is provided by temperature data collected from petroleum wells drilled in the northern Gulf of Mexico (Forrest et al., 2007). Aggregated subsurface temperature measurements made in the Louisiana Shelf Domain, located at or near the southern end of the Mississippi River, display borehole temperature gradients that are most commonly between 25.7 to 32.6°C/km. These two boundary values are considered as representing end-member scenarios that are used to determine end-member geotherms and viscosity profiles based on equations (1) and (2), respectively.

Although it is far less important than the chosen surface temperature gradient, the determination of lithosphere viscosity models also requires that a Moho depth is specified. A Moho measurement from the southern end of the LP is preferred because this is where Earth structure sensitivity is shallowest as a result of the dominance of local sediment loading (see Section 3.3.1). For this, the results of the recent Gulf of Mexico Basin Opening (GUMBO) seismic surveys are referred to. The GUMBO seismic line 2 is closest to the southern end of the Mississippi River; the seismic observations of this survey place the Moho at a depth of 26 km (Eddy et al., 2018). This Moho depth is used for constructing the lithosphere viscosity structure models. The base of the lithosphere is a rheological boundary (Artemieva, 2011) and so we define it here as the depth at which the calculated viscosity is the same as that assumed for the

upper mantle. For this reason, the depth of the modelled lithosphere base will vary according to both the geotherm and the specified UMV.

3.2.3 Model Fit and Parameter Estimation

Modelled surface displacement is generated at the same geographic locations that the observational data were collected (Figure 3.2). For every considered configuration of Earth structure parameters, this modelled output is compared with the observational data using a data-model fit test. To assess model fit, the data-model misfit parameter δ is computed using the following equation:

$$\delta = \frac{\sum_{n=1}^{N} \frac{(O_n - M_n)^2}{\varepsilon_n^2}}{N} \tag{3}$$

where M is the modelled surface displacement, O is the observed surface displacement, ε is the observational uncertainty, and N is the total number of data points. Before this test of model fit is applied, the modelled LP displacement curve is shifted vertically by a fixed amount such that the northernmost points of the data and model output are aligned. This is done to remove the large model and data uncertainty associated with defining relative sea level at the Mississippi Delta during Marine Isotope Stage 5a. This procedure also has the effect of isolating model fit to the shape of the LP displacement curve rather than its absolute height. The height of the LP displacement curve is largely controlled by the ice-load component of the deformation (Wolstencroft et al., 2014; see Section 3.3.1 below), which includes a large degree of uncertainty due to lack of constraints on North American ice extent from 80 ka to the last glacial maximum. As discussed below, the shape of the LP is largely controlled by the sediment and ocean loading and so it is this aspect that is focused on by vertically shifting the model output to match the height of the northernmost datum. Furthermore, by reducing the influence of the ice loading, this procedure results in an inference of Earth viscosity structure that more effectively targets the Mississippi Delta region.

3.3 Results and Discussion

3.3.1 Component-Specific Deformation

The LP displacement is the sum of multiple distinct deformation components, each of which has its own spatial signature and sensitivity to Earth viscosity structure (Wolstencroft et al., 2014). The southern portion of the LP is dominated by sediment loading as a result of the southward progradation of the Mississippi Delta. When sediment is deposited it displaces water, causing a reduction in the ocean load which coincides with sediment deposition. The resulting ocean load change is opposite in effect but lesser in magnitude relative to sediment-related deformation, meaning that sedimentation still ultimately results in downward crustal flexure. This is illustrated in Figure 3.4 where the total LP displacement (black solid line) is tilted sharply downward in the south despite the upward displacement resulting from the removal of the ocean load (dotted line). Displacement in the northern portion of the LP is controlled entirely by ice loading (dashed line). Sediment loading exerts LP displacement which is far more localized due to the zone of sedimentation occupying a small area relative to the entire LP length. Consequently, the shape of the LP displacement curve is strongly controlled by sediment-related deformation, particularly that associated with the shelf component of the sediment load (Wolstencroft et al., 2014). The same can be said for ocean loading, but this is due to the aforementioned water displacement effect of sedimentation.

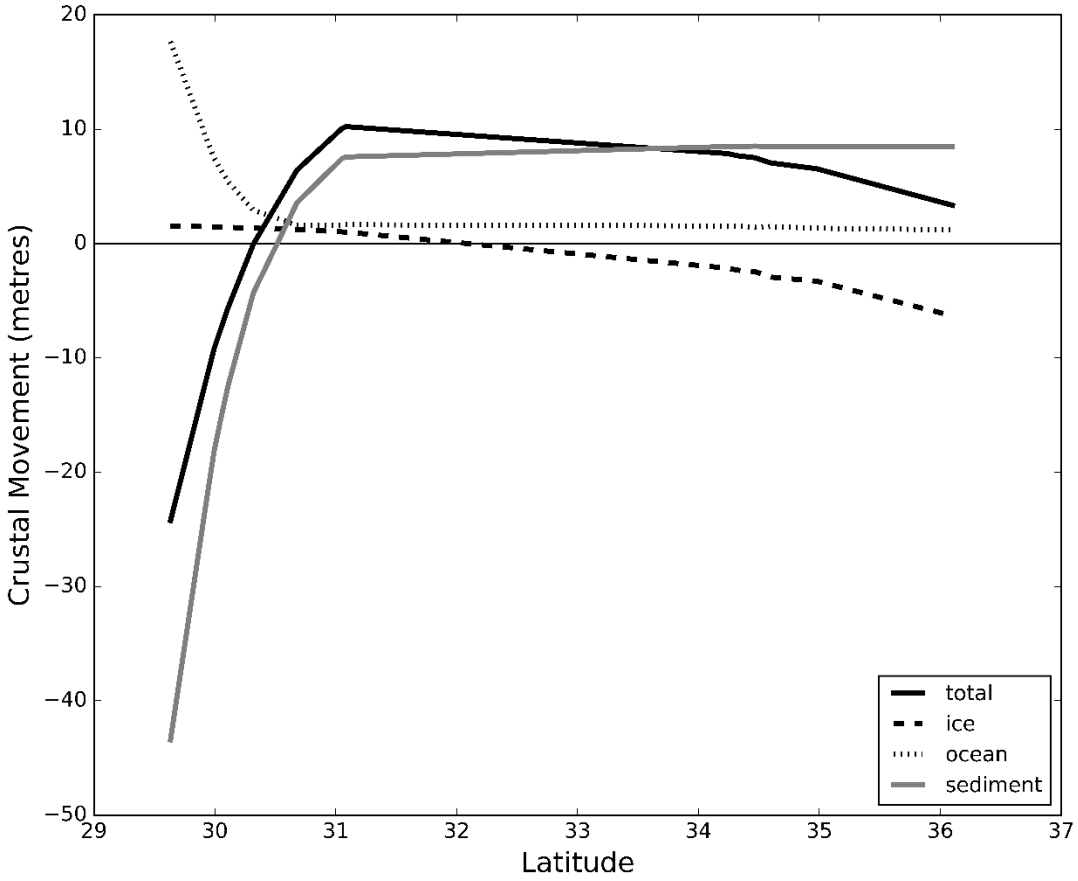

Figure 3.4. Components of modelled LP displacement determined using upper and lower mantle viscosity values of 3×10^{20} and 10^{21} Pas, respectively, and a near-surface geotherm of 25.7°C/km. Load-component symbology indicated in key.

Different portions of the LP displacement curve are controlled by different load components – this has implications for the sensitivity of the corresponding responses to viscosity structure. Different deformation components will have different depth sensitivity to Earth viscosity structure, depending on the lateral extent of the surface load and load proximity to the observations (Mitrovica & Peltier, 1991; Mitrovica, 1996). The continent-scale glaciation which governs the ice-loading component of LP displacement has a much greater lateral extent and is located much farther away than the shelf sediment deposition which dominates the sediment-loading effects in the LP. Consequently, the ice-load component of LP displacement is more

sensitive to viscosity structure at greater depths relative to the sediment-load component. A similar relationship is present for lateral sensitivity to viscosity structure. Glacial isostatic adjustment samples large-scale viscosity structure beneath the North American continental platform. Conversely, the sediment load is sensitive only to local viscosity structure due to its smaller lateral extent. Given that the shape of the LP displacement curve is more sensitive to sediment loading, it follows that the curve is mostly sensitive to viscosity structure which is both shallow and local to the area of sediment loading. Consequently, applying the vertical shift to model output when analyzing data-model fits (see Section 3.2.3) enhances the sensitivity of the results to viscosity structure which is both shallower and more local. This is desirable because one of the primary aims of this study is to analyze the sensitivity to, and constrain the properties of, mechanical structure of the lithosphere in the Mississippi Delta region of the Gulf Coast.

3.3.2 Sensitivity to Lithosphere Rheology

Varying lithosphere rheology does produce LP changes, but the significance of these changes is location-dependent. Variations in lithosphere properties manifest themselves most strongly in the southern portion of the LP displacement curve whereas they are negligible in the northern portion. As noted above, the southern portion has the shallowest depth sensitivity, so this is where changes in lithosphere properties produce changes which are most pronounced. As one would expect, the transition from an entirely elastic lithosphere to a lithosphere which incorporates viscous structure is a change which renders the lithosphere mechanically weaker. Among the two thermal scenarios considered for viscous lithospheres (25.7 and 32.6°C/km near-surface), the warmer geotherm results in a mechanically weaker lithosphere. A convenient and relevant way of thinking about lithosphere strength in this context is to invoke the concept of effective elastic thickness (EET; e.g. Burov & Diament, 1995). The EET of a viscous lithosphere refers to the thickness of a theorized elastic lithosphere which would respond the same way to an applied stress, such as that associated with a surface load resulting in flexure. As the viscosity of material within the lithosphere decreases, the EET is reduced. For an otherwise fixed set of conditions and material properties, a warmer lithosphere will always have a lower EET. This concept is demonstrated by the model output depicted in Figure 3.5. Localized sediment loading causes lithosphere flexure in the southern end of the LP. The variable viscosity lithospheres (in

colour), with their lower EET, are more able to bend to accommodate localized loading as compared to the elastic lithosphere (in black). This results in more vertical displacement proximal to the loading, and less vertical displacement further away, relative to a more rigid lithosphere. In other words, the mechanically weaker lithosphere models exhibit lithospheric flexure which is comparatively higher amplitude and shorter wavelength.

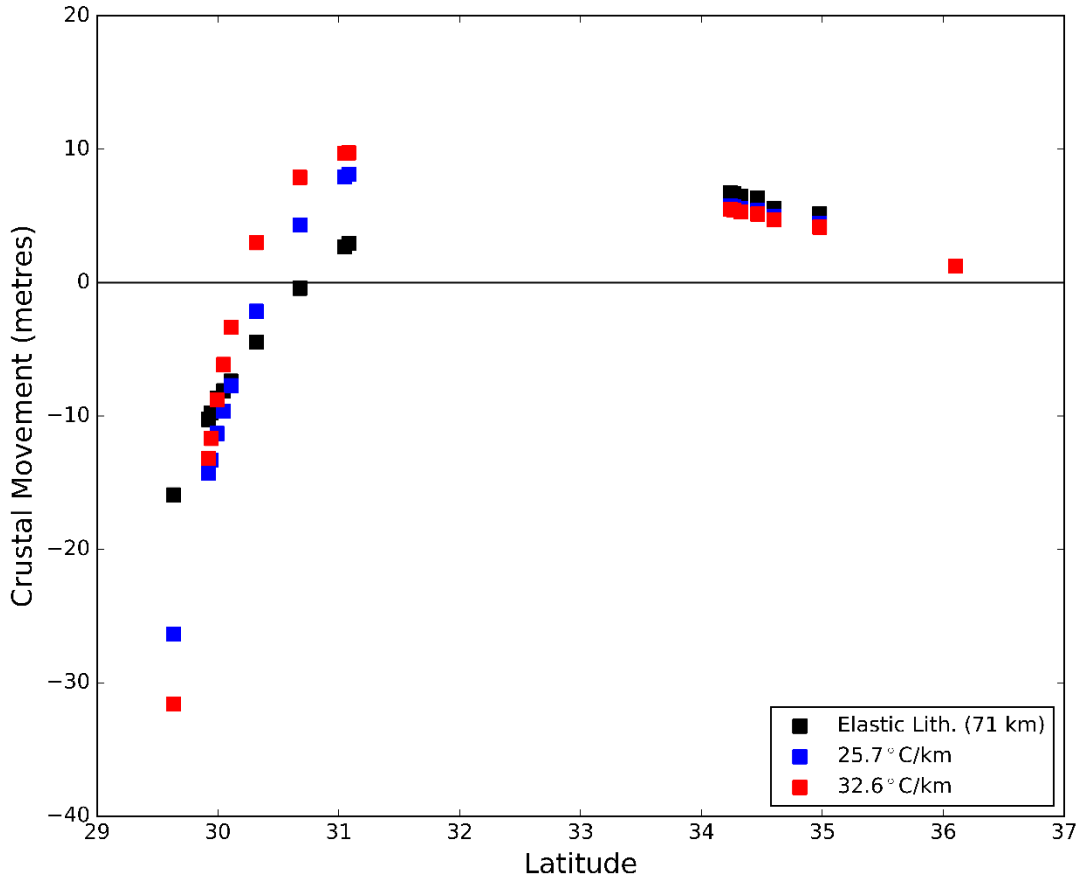

Figure 3.5. Modelled LP displacement at data locations for elastic (black) and viscoelastic (blue and red) models of lithospheric structure. The near-surface geotherms used to compute lithosphere viscosity variations are indicated in the key. All results shown were determined using upper and lower mantle viscosity values of 3×10^{20} and 10^{21} Pas, respectively.

3.3.3 Earth Structure Constraints from Elastic Lithosphere Models

Four different elastic lithosphere thicknesses are considered in conjunction with 50 possible configurations of UMV and LMV (see Section 3.2.2 for details). The modelled output is compared with observational data to evaluate parameter sensitivity and determine parameters that produce an optimal data-model fit. As discussed in Section 3.2.1, the observational data are corrected to account for two different fault-displacement scenarios in the southern end of the LP. The first considered fault adjustment (13% faulting) is less significant and therefore requires that more of the total observed LP displacement be explained by viscoelastic deformation in the model Earth. Conversely, the second considered fault adjustment (40% faulting) requires less viscoelastic deformation to explain the observations. Figure 3.6 illustrates the significance of each faulting scenario on the observational constraints used to determine optimal model parameters. The 13% faulting scenario depicts a pattern of more pronounced lithospheric flexure in the southern end of the LP displacement curve, whereas the 40% faulting scenario displays a pattern of less extreme flexure. Although the elastic lithosphere Earth models appear to adequately satisfy the observations in the northern portion of the LP, they fail to accurately replicate those in the southern portion which exhibit greater vertical displacement. For both faulting scenarios, the optimal models depict lithospheric flexure with a longer wavelength than is indicated by observational constraints.

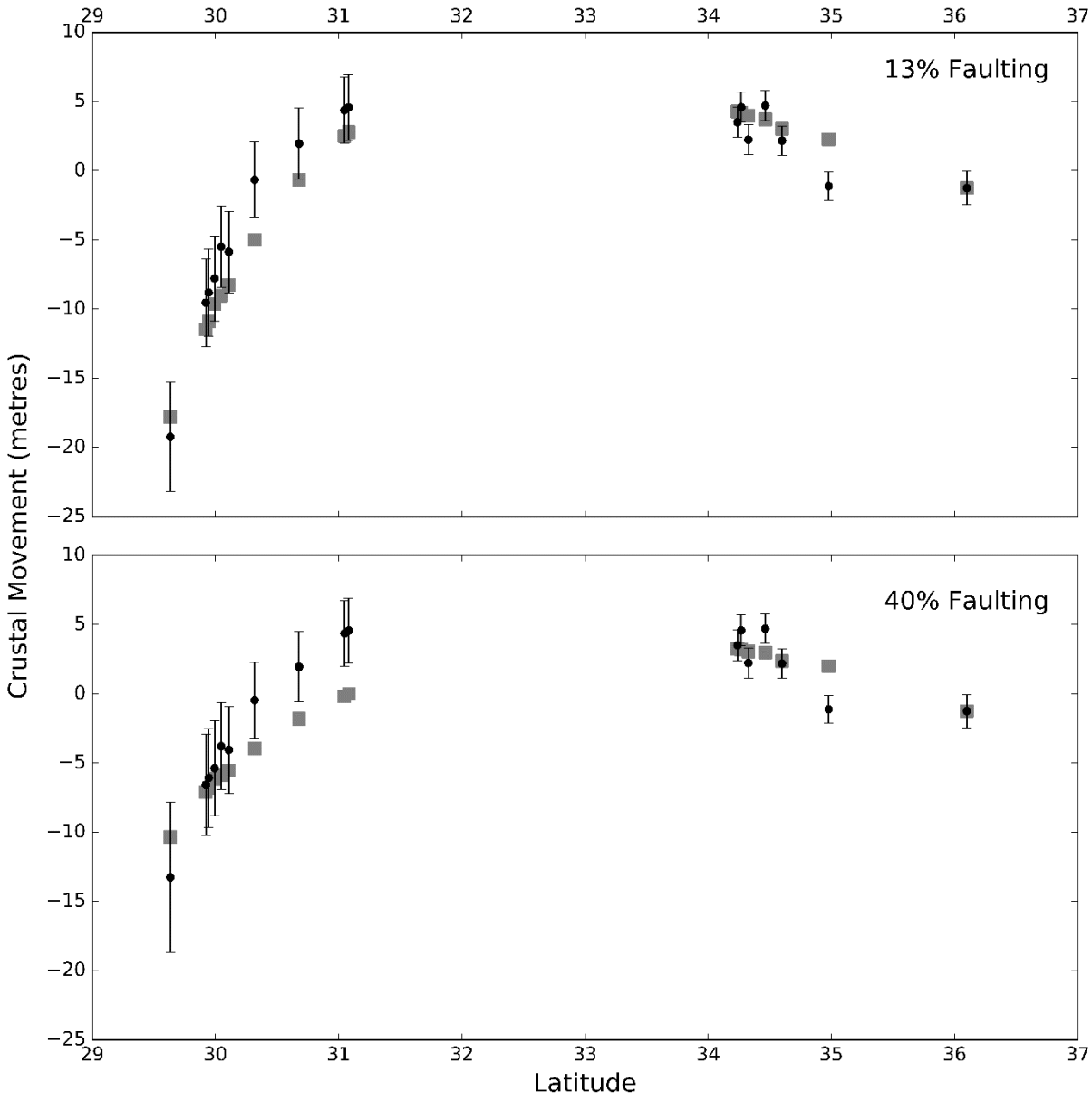

Figure 3.6. Optimal model fit among considered elastic lithosphere Earth models for each fault-displacement scenario. Observational LP displacement (including uncertainty) is plotted in black and modelled values are indicated by grey squares.

A model-fit δ value is computed for every considered elastic lithosphere Earth model and for both faulting scenarios. Both faulting scenarios have the same optimal upper/lower mantle configuration: 10^{20} Pas UMV and 5×10^{21} Pas LMV (see optimal models identified in Figure 3.7).

The independence of the optimal mantle model parameters to the chosen fault correction demonstrates the varying viscosity-depth sensitivity across the length of the LP. Due to the relatively shallow viscosity structure sensitivity in the southern LP portion (see Section 3.3.1) where the fault correction is applied, mantle parameter constraints are unaffected by the chosen faulting scenario. We hypothesise, therefore, that the mantle model requirements are imposed by the northern LP portion, which is sensible given the dominance of the ice-loading signal in that area (Figure 3.4). In contrast, the specified faulting scenario exerts significant control over the optimal lithosphere thickness. A relatively thick lithosphere (120 km) is favoured for the more extreme (40%) faulting scenario compared to a 71 km lithosphere for the 13% faulting scenario. For both faulting scenarios, none of the model fits yield a model-fit δ value of less than 1, indicating an inability of the elastic lithosphere Earth models to satisfy observational constraints.

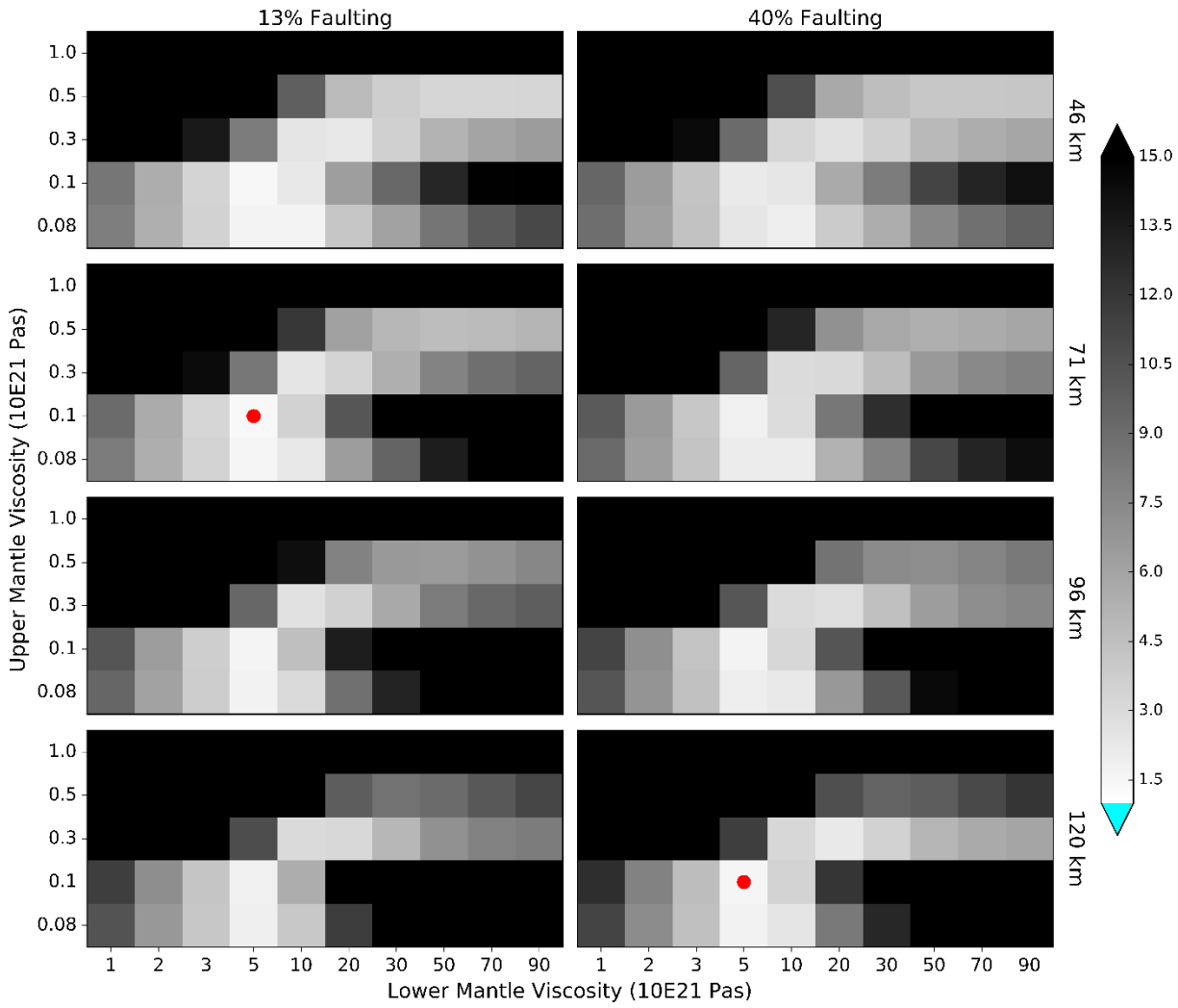

Figure 3.7. Model-fit δ values for all considered elastic lithosphere Earth models. Each column indicates model fits for the two faulting scenarios considered. Each row corresponds to a given elastic lithosphere thickness, as indicated on the right side of each row. Model-fit δ values less than 1 are represented by a light blue colour (see scalebar). Optimal viscosity structure models for each faulting scenario are associated with the lowest model-fit δ values, as marked by a red dot.

For most model parameter sets considered, there is a general preference of the data for thinner lithospheres, as indicated by the greater amount of grey area for lower lithosphere thicknesses on the model-fit figures. However, for a small subset of mantle viscosity configurations this is not the case. The optimal mantle viscosities are the most obvious example of this. The identified

optimal mantle (UMV/LMV) configuration does not always obey this relationship with lithosphere thickness, and in fact for the 40% faulting scenario it is entirely reversed – hence the convergence on a 120 km optimal lithosphere in that case.

In terms of parameter trade-off, one might expect there to be a balance between lithosphere thickness and UMV, or UMV and LMV, as is often evident when modelling other data sets such as relative sea level change or land motion (Nakada & Lambeck, 1988; Lambeck et al., 1996; Milne et al., 2004). However, no such trade-off is evident in the model-fit results. In fact, there is a broad trend of stiffer structure in one portion of the mantle increasing the preference for stiffer structure in the other portion. In Figure 3.7 it can be seen that, for both faulting scenarios and each lithosphere thickness, increasing the UMV shifts the preferred LMV towards higher values. The conspicuous absence of significant parameter trade-off in the model-fit results is further evidence for the different depth sensitivities of the deformation components that comprise the LP displacement signal. Interestingly, there is a subtle trade-off between lithosphere thickness and LMV, whereby higher LMV values become comparatively more favourable as lithosphere thickness is decreased. This trade-off occurs strictly within a single deformation component, as it likely relates to ice-loading effects that contribute a long-wavelength signal to the LP displacement (see Figure 3.4) associated with peripheral bulge dynamics (Clark et al., 1978; Kuchar et al., 2019).

One limitation of this study is the use of a spherically symmetric Earth model. Although its computational efficiency benefits this study by allowing a denser exploration of the parameter space, it fails to account for lateral heterogeneities in Earth structure. Different components of the LP displacement curve sample viscosity structure at different regional scales. The ice-related signal samples continent-scale Earth structure, whereas other deformation components sample more localized structure proximal to the Mississippi River and northern Gulf of Mexico. In reality, there are structural heterogeneities that exist across these spatial scales which cannot be accounted for in the spherically symmetric model. This may also result in the model-fit pattern here deviating from that commonly seen with other data sets. The lack of balanced parameter trade-off between UMV and LMV may be due to the observational data sampling different mantle viscosity structures which are combined to form the total observed signal. The plausibility of this explanation is supported by the results recently published by Kuchar et al.

(2019) which found that, for relative sea level data constraints from the Gulf Coast and Hudson Bay, a significantly better data-model fit could be achieved by allowing lateral mantle viscosity variations instead of using a spherically symmetric mantle.

3.3.4 Earth Structure Constraints from Viscous Lithosphere Models

Earth models that include viscous structure within the lithosphere were constructed using the two considered geotherm scenarios and all 50 possible UMV and LMV configurations (see Section 3.2.2). As expected, the warmer geotherm (32.6°C/km) results in a thinner and weaker lithosphere relative to the colder geotherm (25.7°C/km) (see Figure 3.8). The deviation in lithosphere viscosity between the two geotherms becomes larger at greater depths. As noted in Section 3.2.2.1, the chosen geotherm affects the calculated lithosphere termination depth, with the warmer geotherm resulting in a shallower lithosphere base. However, this rheological boundary in the models is also affected by the specified UMV, albeit less so than by the chosen geotherm. The relationship among these Earth model parameters is shown in Figure 3.9. Selecting a relatively weak upper mantle has the effect of deepening the lithosphere base. A reduction in UMV progressively increases lithosphere thickness in a nonlinear manner such that incremental reductions in UMV are most significant for the lowest considered UMV values. The selected UMV also mediates the geotherm effect; a warmer geotherm reduces lithosphere thickness more if the UMV is softer. Although the chosen geotherm is the most significant determinant of lithosphere thickness, the effect of UMV is considerable. This can be appreciated by comparing the lithosphere termination depths in Figure 3.9 for the weakest (0.08×10^{21} Pas) and strongest (1×10^{21} Pas) UMV values. The lithosphere thickness for the weakest UMV with the warmer geotherm is equivalent to the lithosphere thickness for the strongest UMV with the colder geotherm. As a result of the trade-off between geotherm and UMV, a relatively broad range of lithosphere thicknesses is sampled.

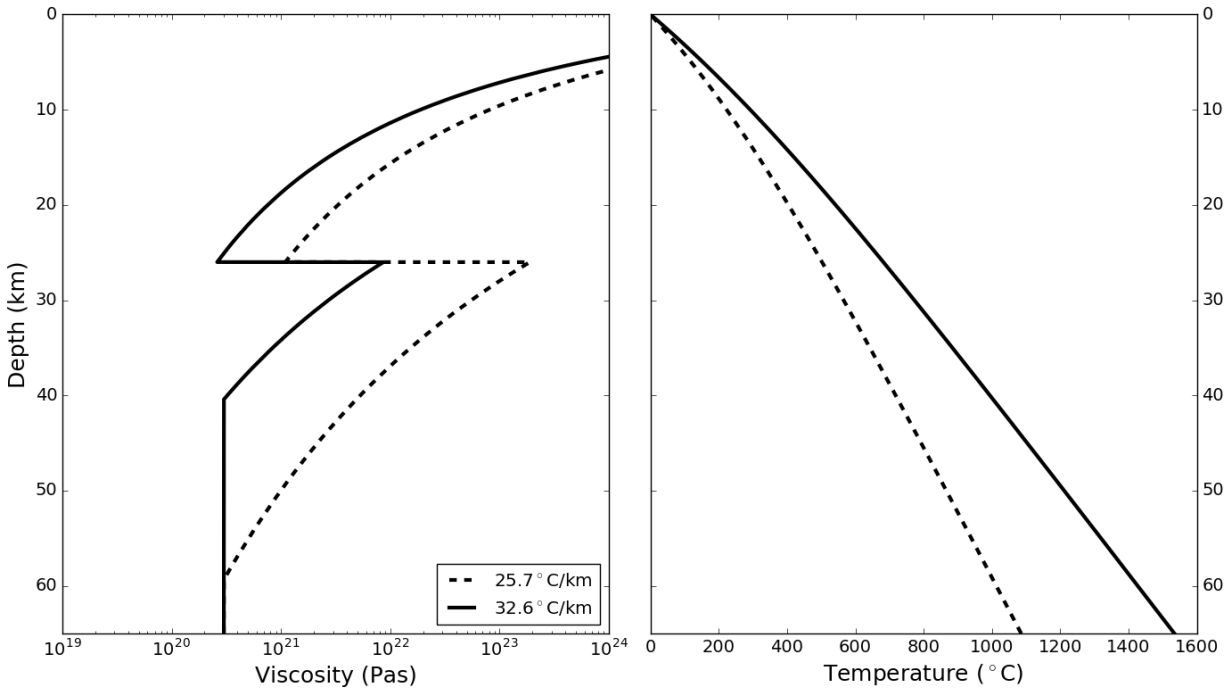

Figure 3.8. Viscosity (on the left) and temperature (on the right) profiles for lithosphere models with viscous structure. Viscosity is depicted on a logarithmic scale (horizontal axis of the left graph). The upper mantle is fixed at 3×10^{20} Pas in this case. The colder and warmer near-surface geotherm scenarios are represented by dashed and solid lines, respectively (see key).

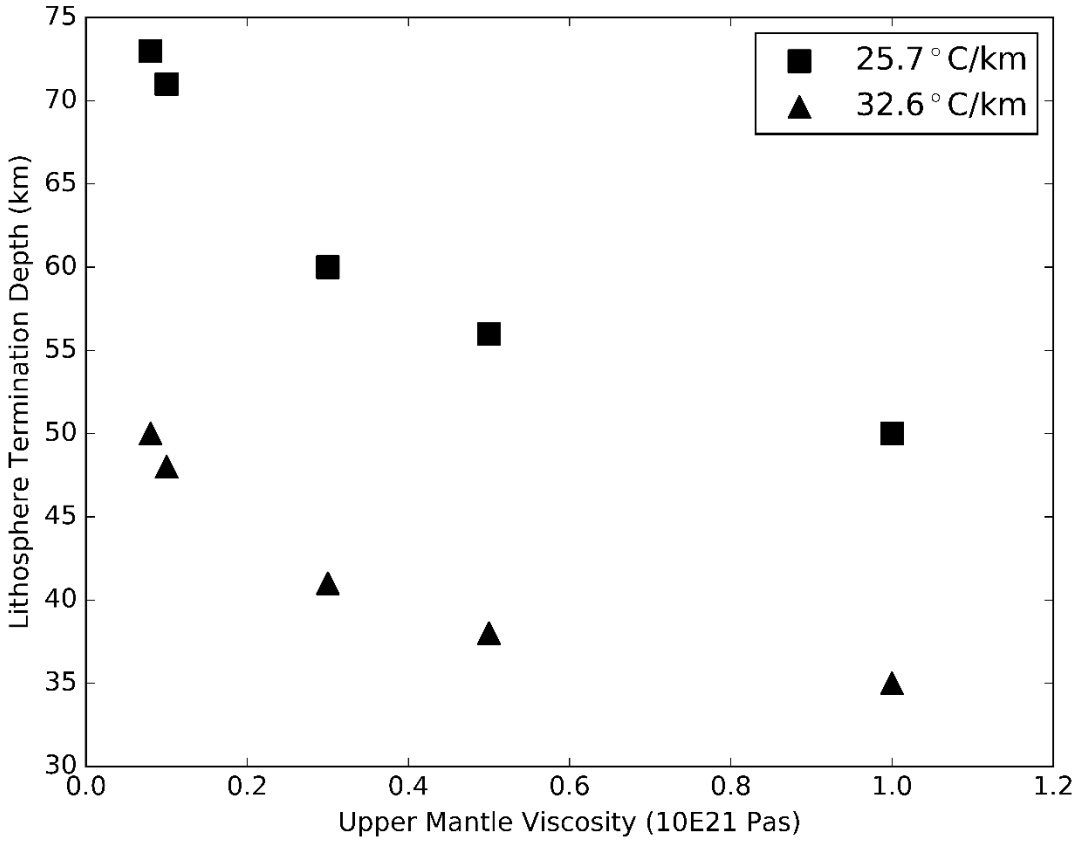

Figure 3.9. Variation in lithosphere termination depths among viscous lithosphere viscosity models for different upper mantle viscosities. The colder and warmer near-surface geotherm scenarios are represented by square and triangle symbols, respectively (see key).

Incorporating viscous structure into the lithosphere acts to reduce its EET compared to the elastic case, particularly for stresses applied over timescales of 10 kyr and longer (Kuchar & Milne, 2015). It is evident from Figure 3.6 that the optimal elastic lithosphere models are not able to replicate the amplitude of flexure in the southern portion of the profile. Therefore, one would expect the viscous lithosphere models to produce an improved fit, at least for the southern portion of the profile, due to their ability to accommodate higher amplitude lithosphere flexure. This is in fact the case, as shown by comparing Figures 3.6 and 3.10. For the 13% faulting scenario the model fit is highly accurate, particularly in the southern portion of the LP where localized high-amplitude flexure is required. In the 40% faulting case, the model fit displays

lithosphere flexure which is somewhat more extreme than is depicted by the observational data. However, even in this case, the model fit appears superior compared to that which was found for the 40% faulting scenario using the elastic lithosphere models.

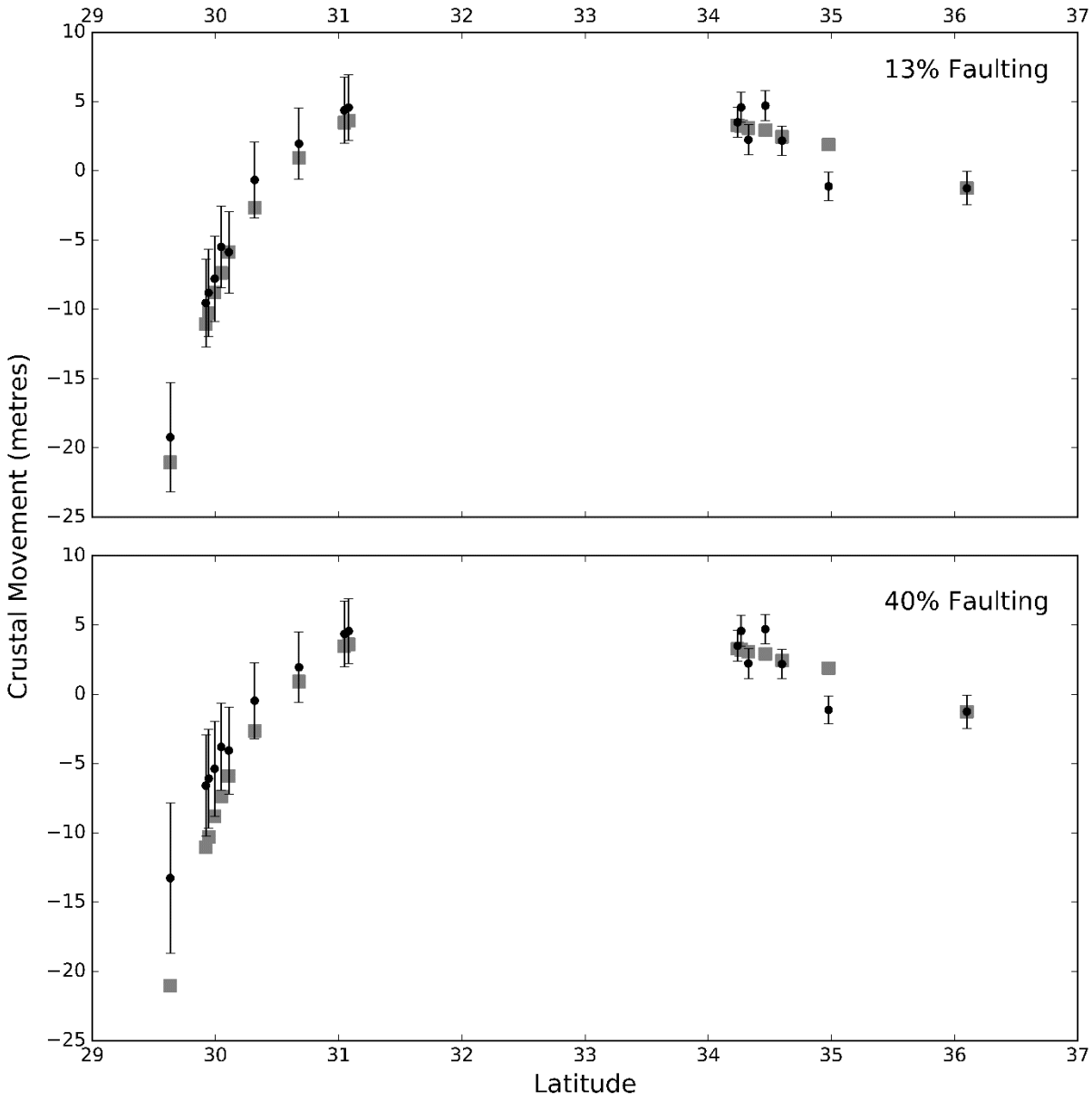

Figure 3.10. Same as Figure 3.6 but for optimal model fit among considered lithosphere models with viscous structure.

Model-fit results for the viscous lithosphere models are plotted in Figure 3.11. As described above, the depth to the bottom of the lithosphere depends on the adopted geotherm and UMV, and so the reader should refer to Figure 3.9 to associate a lithosphere thickness with a given parameter set in Figure 3.11. For both faulting scenarios the identified optimal viscous lithosphere Earth model is the same: 10^{21} Pas UMV and 9×10^{22} Pas LMV with the 32.6°C/km geotherm. This optimal model favours the warmer geotherm in conjunction with the stiffest UMV, meaning that the shallowest lithosphere termination depth among all Earth models is preferred (35 km depth – see Figure 3.9). In addition to its thin and mechanically weak lithosphere, this optimal model is extreme in that it favours the stiffest considered UMV and LMV values. These optimal values of mantle viscosity are considerably stiffer than those found for the elastic lithosphere models, indicating that a reduction in lithosphere EET renders a stiffer mantle more favourable. In fact this relationship between lithosphere EET and mantle viscosity preference is present broadly; in general, the relatively stiffer mantle viscosity configurations in the considered parameter space become more favourable when viscous lithosphere models are used, as compared to the elastic case. Conversely, weaker mantle viscosities often provide better data-model fit when paired with elastic lithospheres. The significance of the trade-off between lithosphere mechanical structure and mantle viscosity can also be appreciated by comparing the northern portions of the optimal LP displacement curves in Figures 3.6 and 3.10; the patterns are nearly identical despite the significantly different Earth model parameters in each case. Similarly, the optimal lithosphere thickness found using a viscous lithosphere rheology is much thinner than what is preferred for the elastic lithosphere rheology, demonstrating that large variations in lithosphere EET can be balanced by viscosity changes in the sub-lithospheric mantle.

The model-fit results (Figure 3.11) depict significant dependence between UMV and LMV with respect to model suitability. Similarly to the elastic lithosphere model results, the viscous lithosphere Earth model results display a pattern of stiffer UMV rendering stiffer LMV more favourable, and vice versa (see Section 3.3.3 for further discussion of this phenomenon). However, one should be mindful that the elastic lithosphere model-fit results displayed in Figure 3.7 are for fixed lithosphere thicknesses, whereas the viscous lithosphere model-fit results in Figure 3.11 include varying lithosphere thicknesses (recall Figure 3.9). Another commonality between the elastic and viscous lithosphere models is that the optimal UMV and LMV values are

the same for either fault-adjustment scenario. However, for the viscous lithosphere models, the fault adjustment does not constrain lithosphere structure because the preferred geotherm scenario is the same in both cases. Comparing the model-fit δ values between faulting scenarios reveals that the results for the 13% faulting scenario are preferred relative to the 40% faulting scenario, but without any perceivable change in overall parameter-fit trends. For the 40% faulting scenario, the optimal model fit yields a model-fit δ value of 1.31, compared to 0.93 in the 13% faulting case. Between the elastic and viscous lithosphere models, a superior model fit is found using a viscous lithosphere for both faulting scenarios. For 13% faulting, the viscous lithosphere model fit outperforms the elastic lithosphere with a model-fit δ value of 0.93 versus 1.40. In the 40% faulting case the difference is somewhat smaller, with the more suitable viscous lithosphere model yielding a model-fit δ value of 1.31 as compared to the elastic lithosphere model with a model-fit δ value of 1.56. Both the elastic and viscous lithosphere models are better able to replicate the observed LP displacement in the 13% faulting scenario relative to 40% faulting, but a model-fit δ value of less than 1 was only achieved using a viscous lithosphere for the 13% faulting case (indicated in light blue in Figure 3.11). The comparative difficulty in replicating the 40% faulting scenario could suggest that, based on the physical framework of the models employed in this study, the 13% fault adjustment is a more realistic appraisal of site conditions and real-world solid-Earth deformation.

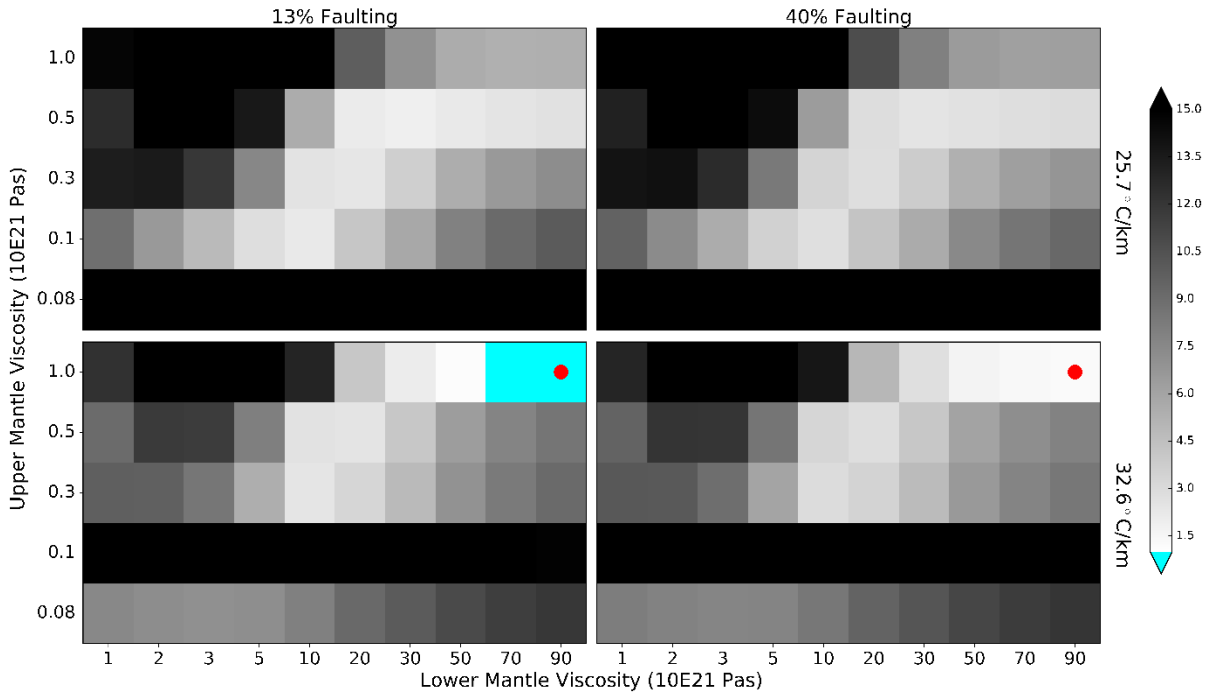

Figure 3.11. Same as Figure 3.7 but for two lithosphere models with viscosity structure. Near-surface geotherms used to define the viscous structure are listed on the right side of each row.

3.4 Conclusions

Using 50 different configurations of sub-lithosphere mantle viscosity structure in conjunction with various lithosphere mechanical structures, the Mississippi River LP displacement over the past ~80 kyr has been interpreted with the assumption that the displacement is dominated by isostatic deformation and fault slippage (in the south portion of the LP). Modelling results for individual isostatic loading components demonstrate that the northern portion of the LP displacement curve is dominated by glacial isostatic adjustment associated with Quaternary continent-scale glaciation, and the southern portion is governed by sediment loading as a result of Mississippi River sedimentation. The analyzed observational data is adjusted using two fault-displacement scenarios in order to obtain a more realistic appraisal of real-world conditions. The employed Earth models consist of a lithosphere which is either entirely elastic or has internal viscosity structure. For the elastic lithosphere models, the optimal lithosphere thickness is strongly controlled by the chosen faulting scenario, with the 13% fault adjustment favouring a 71

km lithosphere thickness, and a comparatively thicker 120 km thick lithosphere being preferred in the 40% faulting case. The viscous lithosphere models are derived using two near-surface geotherms; the warmer (32.6°C/km) geotherm is preferred for both faulting scenarios. For both the elastic and viscous lithosphere Earth models, the chosen faulting scenario exerts no control over the optimal sub-lithosphere mantle configuration. However, the optimal mantle viscosities vary considerably between the two kinds of lithospheres: for the elastic lithosphere, the optimal UMV is 10^{20} Pas and the optimal LMV is 5×10^{21} Pas, whereas the viscous lithosphere models result in optimal mantle viscosities of 10^{21} Pas and 9×10^{22} Pas for UMV and LMV, respectively. The optimal viscous lithosphere Earth model has a lithosphere thickness of 35 km – the shallowest among all evaluated Earth models.

Considerable parameter trade-off between lithosphere mechanical structure and mantle viscosity is evident: a thick elastic lithosphere permits softer mantle viscosity, while a thin and mechanically weak lithosphere requires stiffer mantle viscosities to replicate the same signal. Between the two faulting scenarios, the signal with the 13% fault adjustment is more accurately replicated for both the elastic and viscous lithosphere models. Between the elastic and viscous lithosphere models, the best data-model fit is found using a viscous lithosphere for both faulting scenarios, demonstrating that incorporating viscous lithosphere structure can more accurately replicate the LP displacement. The viscous lithosphere results also illustrate significant parameter trade-off between mantle and lithosphere mechanical properties. For parameter trade-off within the mantle itself (UMV and LMV), a more enigmatic trend is present. Stiffer structure in one portion of the mantle favours stiffer structure in the other portion (and vice versa for weaker mantle viscosities). This trend could be a consequence of different deformation components (i.e. continent-scale glaciation and regional sedimentation) sampling mantle viscosity structure at different spatial scales, consequently producing an observed LP signal which incorporates multiple distinct mantle viscosity signatures. The plausibility of such an explanation is indicative of a limitation of this modelling study – the use of spherically symmetric Earth models. Future work may offer deeper insight into the isostatic signal contained in the Mississippi River LP by using Earth models which permit lateral viscosity variations. Future research may also benefit from utilizing additional observable proxies of solid-Earth deformation, such as records of relative sea level change along the Gulf Coast or geodetic data of 3D land motion.

3.5 References

Artemieva, I.M., 2011. *The Lithosphere: An Interdisciplinary Approach*. Cambridge University Press.

Barnes, S.R., Bond, C., Burger, N., Anania, K., Strong, A., Weilant, S. & Virgets, S., 2017. Economic evaluation of coastal land loss in Louisiana, *J. Ocean Coast. Econ.,* **4**(1), doi:10.15351/2373-8456.1062.

Blum, M.D. & Roberts, H.H., 2012. The Mississippi Delta region: past, present, and future, *Ann. Rev. Earth Planet. Sci.,* **40**, 655-683.

Childs, C., Nicol, A., Walsh, J.J. & Watterson, J., 2003. The growth and propagation of synsedimentary faults, *J. Struct. Geol.,* **25**, 633-648.

Clark, J.A., Farrell, W.E. & Peltier, W.R., 1978. Global changes in postglacial sea level: A numerical calculation, *Quat. Res.,* **9**, 265-287.

Cox, R.T. & Van Arsdale, R.B., 2002. The Mississippi Embayment, North America: a first order continental structure generated by the Cretaceous superplume mantle event, *J. Geodyn.,* **34**, 163-176.

Craddock, W.H. & Kylander-Clark, A.R.C., 2013. U-Pb ages of detrital zircons from the Tertiary Mississippi River Delta in central Louisiana: Insights into sediment provenance, *Geosphere,* **9**(6), doi:10.1130/GES00917.

Cushing, E.M., Boswell, E.H. & Hosman, R.L., 1964. General geology of the Mississippi Embayment: U.S. Geological Survey Professional Paper 448-B.

Dalca, A.V., Ferrier, K.L., Mitrovica, J.X., Perron, J.T., Milne, G.A. & Creveling, J.R., 2013. On post-glacial sea level - III. Incorporating sediment redistribution, *Geophys. J. Int.,* **194**, 45-60.

Day, J.W. & Templet, P.H., 1989. Consequences of sea level rise: implications from the Mississippi Delta, *Coastal Management,* **17**(3), 241-257.

Dixon, T.H., Amelung, F., Ferretti, A., Novali, F., Rocca, F., Dokka, R., Sella, G., Kim, S., Wdowinski, S. & Whitman, D., 2006. Subsidence and flooding in New Orleans, *Nature,* **441**, 587-588.

Dokka, R.K., 2011. The role of deep processes in late 20th century subsidence of New Orleans and coastal areas of southern Louisiana and Mississippi, *J. Geophys. Res.,* **116**, B06403, doi:10.1029/2010JB008008.

Donoghue, J.F., 2011. Sea level history of the northern Gulf of Mexico coast and sea level rise scenarios for the near future, *Clim. Change,* **107**, 17-33.

Dziewonski, A.M. & Anderson, D.L., 1981. Preliminary reference Earth model, *Phys. Earth Planet. Inter.,* **25**(4), 297-356.

Eddy, D.R., Van Avendonk, H.J.A., Christeson, G.L. & Norton, I.O., 2018. Structure and origin of the rifted margin of the northern Gulf of Mexico, *Geosphere,* **14**(4), 1804-1817, doi:10.1130/GES01662.1.

Forrest, J., Marcucci, E. & Scott, P., 2007. Geothermal gradients and subsurface temperatures in the northern Gulf of Mexico, *Search and Discovery,* Article #30048, 1-15.

Frederick, B.C., Blum, M., Fillon, R. & Roberts, H., 2018. Resolving the contributing factors to Mississippi Delta subsidence: Past and present, *Basin Res.,* **31**(1), 171-190, doi:10.1111/bre.12314.

Gagliano, S.M., Kemp, E.B., Wicker, K.M. & Wiltenmuth, K.S., 2003. *Active Geological Faults and Land Change in Southeastern Louisiana*. Prepared for U.S. Army Corps of Engineers, New Orleans District, Contract No. DACW 29-00-C-0034.

Galloway, W.E., Ganey-Curry, P.E., Li, X. & Buffler, R.T., 2000. Cenozoic depositional history of the Gulf of Mexico basin, *AAPG Bulletin,* **84**(11), 1743-1774.

Galloway, W.E., Whiteaker, T.L. & Ganey-Curry, P., 2011. History of Cenozoic North American drainage basin evolution, sediment yield, and accumulation in the Gulf of Mexico basin, *Geosphere,* **7**(4), 938-973.

Glavovic, B.C., 2014. Waves of adversity, layers of resilience: floods, hurricanes, oil spills and climate change in the Mississippi Delta, in *Adapting to Climate Change – Lessons from Natural Hazards Planning,* pp. 369-403, eds Glavovic, B.C. & Smith, G.P., Springer.

Kuchar, J. & Milne, G.A., 2015. The influence of viscosity structure in the lithosphere on predictions from models of glacial isostatic adjustment, *J. Geodyn.,* **86**, 1-9, doi:10.1016/j.jog.2015.01.002.

Kuchar, J., Milne, G.A. & Latychev, K., 2019. The importance of lateral Earth structure for North American glacial isostatic adjustment, *Earth Planet. Sci. Lett.,* **512**, 236-245.

Kuchar, J., Milne, G.A., Wolstencroft, M., Love, R., Tarasov, L. & Hijma, M., 2018. The influence of sediment isostatic adjustment on sea level change and land motion along the U.S. Gulf Coast, *J. Geophys. Res. Solid Earth,* **123**, 780-796, doi:10.1002/2017JB014695.

Lambeck, K., Johnston, P., Smither, C. & Nakada, M., 1996. Glacial rebound of the British Isles – III. Constraints on mantle viscosity, *Geophys. J. Int.,* **125**, 340-354.

Love, R., Milne, G.A., Tarasov, L., Engelhart, S.E., Hijma, M.P., Latychev, K., Horton, B.P. & Törnqvist, T.E., 2016. The contribution of glacial isostatic adjustment to projections of sea-level change along the Atlantic and Gulf coasts of North America, *Earth's Future,* **4**, 440-464, doi:10.1002/2016EF000363.

Mauduit, T. & Brun, J.P., 1998. Growth fault/rollover systems: Birth, growth, and decay, *J. Geophys. Res.,* **103**(B8), 18119-18136.

McCulloh, R.P. & Heinrich, P.V., 2012. Surface faults in the south Louisiana growth-fault province, in *Recent Advances in North American Paleoseismology and Neotectonics East of the Rockies,* pp. 37-49, eds Cox, R.T., Tuttle, M.P., Boyd, O.S. & Locat, J., Geological Society of America.

Milne, G.A., Mitrovica, J.X., Scherneck, H., Davis, J.L., Johansson, J.M., Koivula, H. & Vermeer, M., 2004. Continuous GPS measurements of postglacial adjustment in Fennoscandia: 2. Modeling results, *J. Geophys. Res. Solid Earth,* **109**, B02412, doi:10.1029/2003JB002619.

Mitrovica, J.X., 1996. Haskell [1935] revisited, *J. Geophys. Res.,* **101**(B1), 555-569.

Mitrovica, J.X. & Peltier, W.R., 1991. A complete formalism for the inversion of post-glacial rebound data: resolving power analysis, *Geophys. J. Int.,* **104**(2), 267-288.

Morton, R.A., Bernier, J.C., Barras, J.A. & Ferina, N.F., 2005. Historical subsidence and wetland loss in the Mississippi Delta Plain, *Gulf Coast Association of Geological Societies Transactions,* **55**, 555-571.

Nakada, M. & Lambeck, K., 1988. Non-uniqueness of lithospheric thickness estimates based on glacial rebound data along the east coast of North America, in *Mathematical Geophysics,* pp. 347-361, eds Vlaar, N.J., Nolet, G., Wortel, M.J.R. & Cloetingh, S.A.P.L., D. Reidel Publishing Company.

Needham, H., Brown, D. & Carter, L., 2012. *Impacts and Adaptation Options in the Gulf Coast*. Center for Climate and Energy Solutions.

Nunn, J.A., 1985. State of stress in the northern Gulf Coast, *Geology,* **13**, 429-432.

Peltier, W.R., 1974. The impulse response of a Maxwell Earth, *Rev. Geophys.,* **12**(4), 649-669.

Peltier, W.R., 2004. Global glacial isostasy and the surface of the ice-age Earth: the ICE-5G (VM2) model and GRACE, *Ann. Rev. Earth Planet. Sci.,* **32**, 111-149.

Penland, S. & Ramsey, K.E., 1990. Relative sea-level rise in Louisiana and the Gulf of Mexico: 1908-1988, *J. Coast. Res.,* **6**(2), 323-342.

Petterson, J.S., Stanley, L.D., Glazier, E. & Philipp, J., 2006. A preliminary assessment of social and economic impacts associated with Hurricane Katrina, *Am. Anthropol.,* **108**(4), 643-670.

Salinas, L.M., DeLaune, R.D. & Patrick, W.H., 1986. Changes occurring along a rapidly submerging coastal area: Louisiana, USA, *J. Coast. Res.,* **2**(3), 269-284.

Shen, Z., Dawers, N.H., Törnqvist, T.E., Gasparini, N.M., Hijma, M.P. & Mauz, B., 2017. Mechanisms of late Quaternary fault throw-rate variability along the north central Gulf of Mexico coast: implications for coastal subsidence, *Basin Res.,* **29**(5), 557-570, doi:10.1111/bre.12184.

Shen, Z. & Lang, A., 2016. Quartz fast component optically stimulated luminescence: Towards routine extraction for dating applications, *Radiat. Meas.,* **89**, 27-34.

Tarasov, L., Dyke, A.S., Neal, R.M. & Peltier, W., 2012. A data-calibrated distribution of deglacial chronologies for the North American ice complex from glaciological modeling, *Earth Planet. Sci. Lett.,* **315-316**, 30-40.

Thatcher, C.A., Brock, J.C. & Pendleton, E.A., 2013. Economic vulnerability to sea-level rise along the northern U.S. Gulf Coast, *J. Coast. Res.,* **63**(sp1), 234-243.

Turcotte, D.L. & Schubert, G., 2014. *Geodynamics*. Cambridge University Press.

Wolstencroft, M., Shen, Z., Törnqvist, T.E., Milne, G.A. & Kulp, M., 2014. Understanding subsidence in the Mississippi Delta region due to sediment, ice, and ocean loading: Insights from geophysical modeling, *J. Geophys. Res. Solid Earth,* **119**, 3838-3856, doi:10.1002/2013JB010928.

Yuill, B., Lavoie, D. & Reed, D.J., 2009. Understanding subsidence processes in coastal Louisiana, *J. Coast. Res.,* **54**, 23-36.

Chapter 4

Conclusion

4.1 Research Results Synthesis

In the research presented in this thesis, numerous (1900) computational simulations have been performed in which a diverse array of Earth viscosity structures were subjected to various loading scenarios. The response of the solid Earth in each case has been related to measurable surficial effects which were then compared with observational data. In this way, the validity of each considered Earth model has been assessed and insight into the real-world viscosity structure of the Earth has been gained. Additionally, the sensitivity of the solid-Earth signal to each considered model parameter has been thoroughly examined, and trade-offs as well as dependencies among model parameters have been identified. Understanding the nature of these relationships among the model parameters is important for analyzing the physical processes studied in this research and estimating the degree of non-uniqueness in the obtained parameter estimates.

The geophysical problem described in Chapter 2 (the "Transition Zone Water Filter" theory; Bercovici & Karato, 2003; Karato et al., 2006; Leahy & Bercovici, 2007, 2010) was addressed by defining a model Earth with a low-viscosity melt-rich layer at 410 km depth that was subjected to glacial loading and its related processes (ocean loading and changes in Earth rotation). The modelled response to these forcings was compared to observables which capture that of the real Earth – specifically, relative sea level and geoid ($\dot{J}_2$) data. Both of these observables have complementary depth sensitivities, and using them to impose model constraints was an effective strategy which allowed conclusions to be made about the physical properties of the mantle and the melt-rich layer it contained.

The $\dot{J}_2$ observable was highly sensitive to variations in lower mantle viscosity and restricted this parameter to relatively stiff values ($\geq 10^{22}$ Pas). At two past-glaciated locations, relative sea level predictions were generated and used to determine decay time values. Due to their shallower

depth sensitivity, these determined decay time values imposed the strongest constraints on the upper mantle and the 410 km melt-rich layer itself. Permissible viscosities for the upper mantle were most frequently 3-5×10^{21} Pas, but stiffer values could be accommodated if they were offset by a softer lower mantle. The two considered model parameters for the melt-rich layer itself, thickness and viscosity, exhibited strong trade-off between one another. Thicker melt-rich layers required stiffer viscosities; the thickest (20 km) considered layer was restricted to viscosities of 10^{17} Pas or greater, whereas the thinnest (1 km) layer could have any viscosity within the considered range. The viscosity of the upper mantle also strongly mediated the effect of the melt-rich layer, with a stiffer mantle viscosity enhancing the sensitivity to the layer properties, likely due to a deformation-focusing effect.

As a result of the omnipresent influence of trade-off among model parameters, a unique constraint on the properties of the theorized melt-rich layer could not be determined. However, useful constraints on viscosity were identified for each considered thickness of the melt-rich layer, and the sensitivity of the observational data to the presence and properties of such a layer was thoroughly evaluated. Moreover, multiple glaciation histories were used such that the considerable effect of the chosen ice-loading model could be examined in detail.

Unlike Chapter 2 where lithosphere properties were insignificant, the results of the study in Chapter 3 are strongly dependent on the mechanical behaviour of the lithosphere. This is because, in addition to continental glaciation, the isostatic effects of sedimentation in the Mississippi Delta region are an important driver of the deformation signal captured in a new and unique data set – vertical displacement of the Mississippi River long profile. For this reason, two different approaches were used to represent the lithosphere in the Earth models: conventional elastic lithospheres and lithospheres which had internal viscous structure. The latter was determined from two end-member geotherm scenarios. Although the ice-related isostatic signal has an important influence on the northern portion of the long profile, the southern portion is largely controlled by the more-localized sediment load. However, the observed displacement in the southern portion is also thought to be significantly affected by fault slippage (Gagliano et al., 2003; McCulloh & Heinrich, 2012; Shen et al., 2017; Frederick et al., 2018), and to account for this, two fault-displacement scenarios were considered for which the observational data were corrected such that the isostatic signal was better isolated.

For the elastic lithosphere models, the less significant (13%) faulting scenario preferred a 71 km lithosphere, whereas a thicker (120 km) lithosphere was favoured in the more extreme (40%) faulting case. When viscous lithosphere models were used, the same model configuration was optimal for both faulting scenarios: the thinnest (35 km) viscous lithosphere with the warmer (32.6°C/km) geotherm. For both faulting scenarios, the optimal viscous lithosphere models produced more suitable data-model fits as compared to the elastic lithosphere models, suggesting that the more realistic viscous lithosphere models are required to capture the observations. Similarly, the 13% faulting scenario could be better replicated than its more extreme counterpart using either an elastic or viscous lithosphere, indicating that the less significant fault correction is the more accurate of the two considered. The selected fault correction did not exert any influence over the optimal sub-lithospheric mantle viscosities, however there was highly significant trade-off between mantle viscosity and lithosphere mechanical properties – a much stiffer mantle was required to satisfy the observations when viscous lithospheres were used.

The results of this study demonstrate that, for situations of localized loading such as deltaic sediment deposition, the rheology of the lithosphere is highly significant in determining the solid-Earth response. The model-fit results illustrate that altering lithosphere properties can significantly influence the estimation of other Earth model parameters – even lower mantle viscosity. Another noteworthy aspect of the results is the inferred optimal thickness of lithosphere when viscous structure is included. Choosing a viscous lithosphere rheology paradoxically decreased the optimal thickness relative to the elastic case – this is even more remarkable if one contemplates the even thinner effective elastic thickness of that weak and warm viscous lithosphere. It is clear from the model results that such a significant shift in lithosphere effective elastic thickness can be compensated for by varying the viscosity of the underlying mantle.

4.2 Future Research Work

There are multiple avenues to explore that could improve upon the results presented in this thesis. Beginning with the surface loads imposed on the modelled Earth, it seems obvious that more accurate (both spatially and temporally) models of these loads would ultimately produce modelling results which more precisely replicate the real-world behaviour of the planet. This fact

is demonstrated by the non-negligible ice model sensitivity depicted by the results in Chapter 2. This is even more true for Chapter 3 where, unlike Chapter 2, sensitivity to variations in surface load geometry cannot be attenuated by the use of observational data parameterizations, such as the decay time formalism (Mitrovica et al., 2000).

Moving along to the properties of the Earth model, the assumption of spherical symmetry limits the potential viscosity structures that can be considered, despite its beneficial effect on computational efficiency. This is particularly restrictive when dealing with multiple observational data sources that are geographically distant from each other, or when the observational data is recorded at a position distant from the surface loading area. The studies in Chapters 2 and 3 both show promise for improved model fit if lateral viscosity variations are permitted. Furthermore, the properties of the theorized melt-rich layer in Chapter 2 would be governed by geodynamic factors such as mantle upwelling rates, water content, and the topography of the ~410 km discontinuity, therefore one would expect that such a feature would not be spherically symmetric in reality. Similarly for the analysis in Chapter 3, where lithosphere properties are a strong determinant on model output, the argument for permitting lateral viscosity variations is stronger because the real-world lithosphere is typically more heterogeneous than the sub-lithospheric mantle. There is also the issue of the assumed rheology of the Earth model. The linear Maxwell viscoelastic rheology requires that all modelled deformation occur as a result of the diffusion creep mechanism. However, in reality it is known that dislocation creep is an important process under certain conditions (e.g. low temperature, high stress; Ranalli, 1995), and so incorporating a nonlinear power-law rheology into the Earth model would be useful to determine whether such a model could more accurately replicate the processes, and therefore, observables considered in this thesis.

Finally, there are the observational constraints themselves and how they are interpreted. Clearly, the precision of the model parameter determination will increase as the uncertainties of the observational data are reduced. This is particularly true for the Chapter 3 study where the resolving power of the data in the southern portion of the long profile are unfortunately limited by their observational uncertainty. Aside from simply more accurate measurements, the utmost care should be employed when extracting the desired isostatic signal from the observational data. Improving knowledge of all the processes contained in the observational measurement will

ultimately lead to more accurate model constraints if the signal due to these other processes can be accurately estimated and removed. For example, mass transfer related to modern polar ice sheet melting must be removed from the $\dot{J}_2$ measurement, and the effect of fault mobilization is clearly significant in the Mississippi River long profile displacement record.

In terms of study design, the way that observational constraints are utilized is a crucial aspect. A recurring theme in the research presented here is the depth sensitivity of the observational data. The resolving power of a dataset mirrors its depth sensitivity, and it is crucial to be mindful of this resolving power when interpreting the study results. Future work should seek to formally incorporate resolving power into the parameter estimation process by the application of a formal data inversion (e.g. Mitrovica, 1996; Mitrovica & Forte, 2004; Lau et al., 2016). Another noteworthy and related point is that, because the depth sensitivity of the long profile varies considerably with latitude, future work might benefit from separating the long profile into spatial portions and determining model constraints independently. Additionally, including other observational constraints in an analysis can improve the precision of the results, particularly when the observations have different depth sensitivities. Beyond observational data and how to use it, another way to arrive at more precise parameter determinations would be to perform a joint inversion in which a separate geophysical process that is also sensitive to viscosity structure is evaluated, such as mantle convection dynamics (e.g. Forte & Mitrovica, 1996; Mitrovica & Forte, 1998, 2004).

4.3 References

Bercovici, D. & Karato, S.-I., 2003. Whole-mantle convection and the transition zone water filter, *Nature,* **425**, 39-44.

Forte, A.M. & Mitrovica, J.X., 1996. New inferences of mantle viscosity from joint inversion of long-wavelength mantle convection and post-glacial rebound data, *Geophys. Res. Lett.,* **23**, 1147-1150.

Frederick, B.C., Blum, M., Fillon, R. & Roberts, H., 2018. Resolving the contributing factors to Mississippi Delta subsidence: Past and present, *Basin Res.,* **31**(1), 171-190, doi:10.1111/bre.12314.

Gagliano, S.M., Kemp, E.B., Wicker, K.M. & Wiltenmuth, K.S., 2003. *Active Geological Faults and Land Change in Southeastern Louisiana*. Prepared for U.S. Army Corps of Engineers, New Orleans District, Contract No. DACW 29-00-C-0034.

Karato, S.-I., Bercovici, D., Leahy, G., Richard, G. & Jing, Z., 2006. The transition-zone water filter model for global material circulation: Where do we stand?, in *Earth's Deep Water Cycle,* pp. 289-313, eds Jacobsen, S.D., Van Der Lee, S., American Geophysical Union.

Lau, H.C.P., Mitrovica, J.X., Austermann, J., Crawford, O., Al-Attar, D. & Latychev, K., 2016. Inferences of mantle viscosity based on ice age data sets: Radial structure, *J. Geophys. Res. Solid Earth,* **121**, 6991-7012, doi:10.1002/2016JB013043.

Leahy, G. & Bercovici, D., 2007. On the dynamics of a hydrous melt layer above the transition zone, *J. Geophys. Res.,* **112**, B07401, doi:10.1029/2006JB004631.

Leahy, G. & Bercovici, D., 2010. Reactive infiltration of hydrous melt above the mantle transition zone, *J. Geophys. Res.,* **115**, B08406, doi:10.1029/2009JB006757.

McCulloh, R.P. & Heinrich, P.V., 2012. Surface faults in the south Louisiana growth-fault province, in *Recent Advances in North American Paleoseismology and Neotectonics East of the Rockies,* pp. 37-49, eds Cox, R.T., Tuttle, M.P., Boyd, O.S. & Locat, J., Geological Society of America.

Mitrovica, J.X., 1996. Haskell [1935] revisited, *J. Geophys. Res.,* **101**(B1), 555-569.

Mitrovica, J.X. & Forte, A.M., 1998. New insights obtained from joint inversions for the radial profile of mantle viscosity, *Phys. Chem. Earth,* **23**, 857-863.

Mitrovica, J.X. & Forte, A.M., 2004. A new inference of mantle viscosity based upon joint inversion of convection and glacial isostatic adjustment data, *Earth Planet. Sci. Lett.,* **225**, 177-189.

Mitrovica, J.X., Forte, A.M. & Simons, M., 2000. A reappraisal of postglacial decay times from Richmond Gulf and James Bay, Canada, *Geophys. J. Int.,* **142**, 783-800.

Ranalli, G., 1995. *Rheology of the Earth*. Chapman & Hall.

Shen, Z., Dawers, N.H., Törnqvist, T.E., Gasparini, N.M., Hijma, M.P. & Mauz, B., 2017. Mechanisms of late Quaternary fault throw-rate variability along the north central Gulf of Mexico coast: implications for coastal subsidence, *Basin Res.,* **29**(5), 557-570, doi:10.1111/bre.12184.